Near Real-Time Impact Point Prediction for the Flight Termination System of the DART XL Sounding Rocket

Commissioned by T-Minus Engineering B.V.

Laura Koelemij

Delft University of Technology

Near Real-Time Impact Point Prediction for the Flight Termination System of the DART XL Sounding Rocket

by

Laura Koelemij

to obtain the degree of Master of Science
at the Delft University of Technology,
to be defended publicly on Friday July 15th 2022 at 14:00h.

Thesis Report - Version 1.0

Student number:	4725689	
Project duration:	July 1st 2020 – July 15th 2022	
Thesis committee:	ir. M. C. Naeije,	Delft University of Technology, supervisor
	ir. R. H. P. Eerkens,	T-Minus Engineering B.V., supervisor
	Dr.ir. W. van der Wal	Delft University of Technology
	Dr. A. Cervone	Delft University of Technology

This thesis is confidential and cannot be made public until July 15th 2024.

Preface

This report is the result of a thesis project at the TU Delft department of Aerospace Engineering, in cooperation with T-Minus Engineering B.V.. It is a study on how to develop an algorithm to predict a sounding rocket's instantaneous impact point in near real-time during a launch, with the purpose of informing a range safety officer's flight termination decision. According to Murphy's Law, 'anything that can go wrong will go wrong'. It is therefore crucial to carefully consider every aspect of model development in terms of impact point accuracy, model computation time and being able to unambiguously interpret the results. The main goal of this report is to detail the development of a first iteration of this prediction model and describing the considerations and assumptions made along the way.

The completion of this thesis also marks the completion of my time as a student. It has been a long journey, and I will definitely never forget the lessons learned in the multiple cities and multiple countries that this journey has taken me to. Specifically during the thesis work, I have learned more about myself than I ever thought I would. Who knew starting a thesis while working from home during a pandemic would suddenly become part of the curriculum...

Therefore, I would first like to thank my supervisors Marc Naeije of the TU Delft and Roel Eerkens of T-Minus Engineering. Through all the ups and downs, you were always there to guide me and offer words of encouragement. To T-Minus Engineering as a whole, thank you for truly making feel like part of the team and offering the best distractions from my thesis work in the form of launch campaigns. To Kevin Cowan, thank you for the wise words and insightful comments during my midterm presentation, as well as the encouraging Space Bar conversations.

Furthermore, I would like to thank my friends who were always up for talking about the victories and hurdles, and forcing each other to leave the house when there really was nothing to do outside. The many hours of Dungeons & Dragons and League of Legends definitely provided some much needed relief.

Finally, I would like to thank the people closest to me. To my family, for all the support throughout my student years and offering a place to recharge myself. You can now stop asking my when I will be graduating, it is finally happening. Actually. Last but not least, I want to offer the biggest thanks to Willem. The words of encouragement, the late night conversations about my work and of course proof-reading my entire report, I truly could not have done this without you.

Laura Koelemij
Delft, July 4th 2022

Abstract

A flight termination system (FTS) is one of the most important safety features on a launch vehicle, as it allows for the vehicle's flight to be terminated in a controlled way when predetermined safety criteria or boundaries are exceeded. Every vehicle, launch range or company may require different safety criteria to form the foundation of the FTS. This includes T-Minus Engineering B.V., who aim to develop a custom flight termination system for the Dart payload stage of their DART XL sounding rocket. A sounding rocket is by definition sub-orbital, so an important safety constraint is its impact location. Based on this impact location, an advice can be formed for a range safety officer (RSO) to base flight termination decisions on. Therefore, the objective of this thesis is creating an algorithm to predict the instantaneous impact point (IIP) of the DART XL's ballistic payload stage in near real-time during a launch, considering impact probability area boundaries and requirements for the accuracy and update rate.

To meet this objective, two separate models were created. The first was a pre-flight nominal trajectory model aimed at evaluating the nominal vehicle trajectory and thereby producing inputs and verification tools to assist the development of the second model. The second model, the in-flight IIP prediction model, is intended to run during a DART XL launch to predict the ballistic trajectory and IIP of the Dart stage in the post-separation phase. This IIP prediction will then continuously be updated and displayed to an RSO to advise their flight termination decisions. An important element of developing both models is determining the model definitions. The final environment model selection consists of a US76 atmospheric model, a central gravity model including the J_2 effect, a local wind model and a rotating, ellipsoidal Earth model. Furthermore, using 3-degrees of freedom (3-DoF) for the IIP prediction model resulted in IIP predictions close to those predicted using a nominal trajectory model of more degrees of freedom. The only exception was the local wind model, which required a correction factor because using 3-DoF excludes the influence of rotational inertia which causes a delay in the effects of wind.

Furthermore, an Euler integrator with a step-size of 0.01 s was initially used for the IIP prediction model. However, this did not meet the computation time requirement of an update rate of 1 s or less. Model modifications could not sufficiently decrease the overall computation time for this step-size. Therefore, it was decided to change the integration step-size to 0.1 s. With this updated step-size, the IIP prediction model did successfully meet the computation time requirement. For the accuracy requirement, the IIP prediction model shall only include parameters that influence the prediction in the order of 1 km. To evaluate this, the nominal impact point results of the pre-flight nominal trajectory model were used to verify the results of the IIP prediction model. By comparison, it was concluded that the accuracy requirement was successfully met using the updated step-size of 0.1 s, with a distance to the verification IIP of less than 600 m.

Additionally, the nominal impact point distribution was determined by performing Monte Carlo simulations of the pre-flight nominal trajectory model. The resulting IIP distribution was used to determine the 3-σ impact probability area, which serves as a measure of the uncertainty of the nominal impact point. The uncertainty in the downrange direction was found to be larger than the uncertainty in the crossrange direction, which was to be expected due to the larger influence of errors in the direction of flight. The effect of varying individual parameters using a One-at-a-Time approach was investigated in a sensitivity analysis. Out of the ten investigated parameters, only the influence of the drag coefficient of the ballistic Dart payload stage was found to exceed the 1 km accuracy radius.

It should be noted that uncertainties remain in this nominal prediction larger than the desired 1 km accuracy radius, represented by for example the ballistic impact probability area and Dart drag coefficient. However, it is unlikely that the uncertainty of the nominal IIP prediction can be decreased below a radius of 1 km due to the inherent unpredictability of launch conditions. Nonetheless, recommendations for future work include investigating individual parameter influences on the IIP dispersion, reducing the drag coefficient uncertainty and implementing additional aerodynamic data, as well as investigating the implementation of a variable step-size integrator. With these recommendations in mind, the overall conclusion is that the thesis work has successfully developed a model for the near real-time instantaneous impact point prediction of the DART XL sounding rocket's Dart payload stage.

List of Figures

2.1 The T-Minus CanSat launcher, designed for educational competitions. 6
2.2 The T-Minus DART and DART XL vehicles. 6
2.3 Information flows for the decision making process in different flight termination systems. 9
2.4 Visualization of flight termination based on instantaneous impact point (IIP) prediction. . 10

3.1 The DART XL Dart, an unpropelled payload stage. 16
3.2 The DART XL booster stage, containing the solid rocket motor. 17
3.3 Allowable impact area for Andøya Space during the 2021 PMWE campaign, where a DART was launched. 18
3.4 Functional diagram of the capabilities of the Trajectory Reconstruction Unit (TRU). . . . 21

4.1 Local wind area with respect to the allowable impact area boundary. 26
4.2 Wind profile data, as analysed from the ERA5 database for the Andøya launch site. . . 27

5.1 Environment model comparisons upon which to base the selection of the individual aspects, with respect to the required 1 km accuracy radius. 37
5.2 Latitude and longitude coordinate comparison for the expanded model versions and the baseline model with selected environment. 38
5.3 Horizontal distance and altitude comparison for the expanded model versions and the baseline model with selected environment. 39
5.4 Impact point distribution relative to the Andøya allowable impact area, for a Monte Carlo simulation of 25000 runs during the ballistic flight phase. 40
5.5 Histogram and normal distribution fit of the impact point latitudes and longitudes. 40
5.6 Convergence and confidence analysis of the impact point latitudes and longitudes. . . . 41
5.7 IIP distribution and subsequent impact probability ellipse relative to the Andøya allowable impact area, for a Monte Carlo of 25000 runs during the ballistic flight phase. 41
5.8 IIP distribution and subsequent impact probability ellipse relative to the Andøya allowable impact area, for a Monte Carlo of 25000 runs for the full flight from launch to impact. . . 42

6.1 The Earth-Centered Inertial reference frame. 44
6.2 The Earth-Centered Earth-Fixed reference frame. 44
6.3 The body-fixed frame for the REXUS vehicle. 45
6.4 The East-North-Up reference frame. 45
6.5 Visual representation of the translational and rotational degrees of freedom. 46
6.6 Temperature versus altitude profile according to the United States Standard Atmosphere 1976, with lapse rate L_i. 47
6.7 Visualization of an ellipsoidal Earth model and the different latitude definitions. 49
6.8 Regimes of a planar ballistic launch trajectory, assuming a spherical Earth. 51
6.9 Representation of the positive directions of downrange distance, crossrange distance and altitude for the TRU frame and the ENU frame. 53

7.1 Implementation of environment model aspects in the IIP prediction model, compared to its baseline IIP and the nominal trajectory model results. Results with respect to the required 1 km accuracy radius. 56
7.2 Implementation of the updated wind scaling factor of 0.06 times the relative atmospheric density. 57
7.3 Implementation of the updated wind scaling factor for a fictitious constant wind magnitude of 2 m/s up to 45 km. 58
7.4 Combined implementation of all selected environment model aspects, compared to the nominal trajectory model results with respect to the required 1 km accuracy radius. . . . 59

7.5 Latitude and longitude coordinate comparison for the pre-flight nominal trajectory model versions and the IIP prediction model. 59
7.6 Horizontal distance and altitude comparison for the pre-flight nominal trajectory model versions and the IIP prediction model. 60
7.7 IIP prediction model results for an initial state vector of the baseline + environment and the expanded pre-flight nominal trajectory models, for a step-size of dt = 0.01 s. 60
7.8 Computation time per run for each initial state vector between burnout and impact, for a step-size of dt = 0.01 s. 61
7.9 Computation time per run for each initial state vector between burnout and impact, for a step-size of dt = 0.1 s. Compilation of ten prediction simulations, with highlighted simulations for visualisation purposes only. 62
7.10 IIP prediction model results for an initial state vector of the baseline + environment and the expanded pre-flight nominal trajectory models, for a larger step-size of dt = 0.1 s. . 62
7.11 Visual output representation, as displayed to an RSO. To be updated with the most recent IIP prediction in real-time, with the previous 100 predictions visible for reference. 63
7.12 Numerical output presentation, as displayed to an RSO. Corresponding to the final three impact predictions of a simulation, with a message stating that IIP prediction has been (temporarily) paused due to a lack of new input data entries. 64
7.13 Impact point comparison for a launch from Whalers Way, South Australia, at an azimuth of 180 deg and an elevation of 60 deg. 65

8.1 The effect of parameter uncertainties on the downrange distance, with respect to the nominal IIP. 71
8.2 The effect of parameter uncertainties on the crossrange distance, with respect to the nominal IIP. 71

A.1 Sea level thrust, measured from a DART XL SRM static test. 77
A.2 Nozzle geometry for a nozzle of arbitrary dimensions. 78
A.3 Area and velocity ratios as a function of pressure ratio for the diverging section of a supersonic nozzle, with added indicators for the DART XL nozzle in red. 79
A.4 Calculated thrust coefficients at sea level and in vacuum as a function of burn time. . . 80
A.5 Thrust coefficient C_F versus nozzle area ratio for k = 1.20, with added indicators for the DART XL nozzle in red. 80
A.6 Thrust coefficient C_F as a function of pressure ratio, nozzle area ratio, and specific heat ratio for optimum expansion conditions ($P_e = P_a$), with added indicators for the DART XL nozzle in red. 81
A.7 Thrust conversion from sea level to vacuum as a function of burn time, where the dashed line represents the corrected vacuum thrust used in the trajectory simulations. 81
A.8 Linear fit of the difference between the vacuum and sea level thrust as a function of burn time, to determine the correction factor. 82
A.9 Center of pressure versus Mach number of the DART XL. 82
A.10 Drag coefficient versus Mach number of the powered DART XL. 83
A.11 Drag coefficient versus Mach number of the unpowered DART XL. 83
A.12 Drag coefficient versus Mach number of the DART XL Dart payload stage. 83

B.1 Impact point distribution relative to the Andøya allowable impact area, for a Monte Carlo simulation of 25000 runs during the ballistic flight phase. 86
B.2 Histogram and normal distribution fit of the impact point latitudes and longitudes for a Monte Carlo of the full flight. 86
B.3 Convergence and confidence analysis of the impact point latitudes and longitudes. . . . 87
B.4 Evaluating the validity of the assumption of a zero roll rate during the ballistic flight phase. 88
B.5 Convergence and confidence analysis of the impact point latitudes and longitudes, for a simulation with a sustained roll rate throughout the ballistic phase. 88

E.1 Table of mechanical characteristics of the high-range accelerometers used in the TRU. 93
E.2 Table of mechanical characteristics of the high-accuracy accelerometers used in the TRU. 95

List of Tables

2.1 Comparison of dimensions and characteristics of the DART and the DART XL sounding rockets. 7

3.1 Overview of the input parameters presented in this section. 19

4.1 Baseline environment model selection and alternative options. 27
4.2 Dispersion parameters for Monte Carlo analysis of the full trajectory from lift-off to impact. 33
4.3 Dispersion parameters for Monte Carlo analysis of the ballistic trajectory from motor burnout to impact. 34

5.1 Overview of the selected environment model aspects. 36
5.2 Impact point coordinates of the different nominal trajectory model versions and the ground distance between them. 39

8.1 Individual components and total 1-σ uncertainties of the initial ballistic state vector of the DART XL Dart payload stage in the TRU frame. 69
8.2 Selected parameters for the one-at-a-time sensitivity analysis of the in-flight IIP prediction model. 70

A.1 Descriptions and values of variables used for the thrust conversion. 78

C.1 Verification and validation reference table. 89

D.1 Descriptions of variables and frame superscripts used in the frame transformations. . . 91

List of Symbols

Symbol	Unit	Description
γ	deg	Flight path angle
γ_0	deg	Launch elevation angle
δ	deg	Declination
δ_w	-	Wind correction factor
Λ	deg	Longitude
Λ_0	deg	Launch longitude
λ	deg	Latitude
λ_0	deg	Launch latitude
μ	-	Mean value
μ_{MC}	-	Cumulative average across a Monte Carlo simulation
μ_E	m^3/s^2	Geocentric gravitational constant
ρ	kg/m^3	Atmospheric density
ρ_0	kg/m^3	Sea level atmospheric density
σ	-	Standard deviation
χ	deg	Heading angle
χ_0	deg	Launch azimuth angle
ω	rad/s	Earth rotation rate
$C_{D,d}$	-	Dart drag coefficient
$COM_{b,i}$	m	Booster center of mass in direction 'i'
$COM_{d,i}$	m	Dart center of mass in direction 'i'
$COM_{p,i}$	m	Propellant center of mass in direction 'i'
D	N	Drag
e	-	Eccentricity
f	-	Flattening factor
g	m/s^2	Gravitational acceleration
g_0	m/s^2	Sea level gravitational acceleration
g_r	m/s^2	Radial gravitational acceleration
g_λ	m/s^2	Latitudinal gravitational acceleration
h	m	Geometric altitude
I	kg m^2	Moment of inertia
Isp	s	Specific impulse
L	K/m	Lapse-rate
m_d	kg	Dart structural mass
n	-	Number of runs in a Monte Carlo simulation
p	Pa	Atmospheric pressure
R	-	Specific gas constant for air
R_e	km	Mean radius of the Earth

Symbol	**Unit**	**Description**
$R_{e,eq}$	km	Equatorial radius of the Earth
$R_{e,pl}$	km	Polar radius of the Earth
$R_{e,s}$	km	Local radius of the Earth
r	m	Distance between center of Earth and vehicle
S	m	Position
SE	-	Standard error
T	K	Temperature
T_0	K	Sea level temperature
t	s	Flight time
V	m/s	Velocity
$V_{w,N}$	m/s	Northerly wind velocity (blowing from South to North)
$V_{w,E}$	m/s	Easterly wind velocity (blowing from West to East)
X_{CP}	m	Center of pressure
z	m	Geopotential altitude

List of Abbreviations

Abbreviation	**Description**
AFTS	Autonomous Flight Termination System
ASTOS	Analysis, Simulation and Trajectory Optimization Software
B	Baseline environment model settings
COCOM	Coordinating Committee for Multilateral Export Controls
CoM	Center of Mass
DOPRI	Dormand-Prince
DoF	Degrees of Freedom
ECEF	Earth-Centered Earth-Fixed
ECI	Earth-Centered Inertial
ECMWF	European Centre for Medium-Range Weather Forecasts
ENU	East-North-Up
EoM	Equations of Motion
FTS	Flight Termination System
GNSS	Global Navigation Satellite System
IIP	Instantaneous Impact Point
IMU	Inertial Measurement Unit
INS	Inertial Navigation System
MC	Monte Carlo
NAFTU	NASA Autonomous Flight Termination Unit
OAT	One-at-a-time
RK4	Runge-Kutta 4
RO	Research Objective
RQ	Research Question
RSO	Range Safety Officer
SO	Sub-Objective
SQ	Sub-Question
SR	System Requirement
SRM	Solid Rocket Motor
TR	Thesis Requirement
TRU	Trajectory Reconstruction Unit
US62	United States Standard Atmosphere 1962
US76	United States Standard Atmosphere 1976

Contents

Preface iii

Abstract v

List of Figures vii

List of Tables ix

List of Symbols xii

List of Abbreviations xiii

1 Introduction 1
- 1.1 Thesis Objectives 1
  - 1.1.1 Research Objective 2
  - 1.1.2 Research Question 2
- 1.2 Report Structure 3

2 Background 5
- 2.1 Company Profile: *T-Minus Engineering* 5
- 2.2 Vehicle Profile: *DART XL* 5
- 2.3 Flight Termination Systems 7
  - 2.3.1 Order of Events 7
  - 2.3.2 Traditional versus Autonomous Flight Termination 8
  - 2.3.3 Flight Termination Conditions 9
- 2.4 Current State-of-the-art 10
  - 2.4.1 Traditional Systems 10
  - 2.4.2 The Transition to Autonomous Systems 11
- 2.5 Requirements by T-Minus Engineering 12
  - 2.5.1 General System Requirements 12
  - 2.5.2 Thesis Requirements 13

3 Model Definitions and Assumptions 15
- 3.1 In-flight Instantaneous Impact Point Prediction Model 15
- 3.2 Pre-flight Nominal Trajectory Model 15
- 3.3 Initial Model Inputs 16
  - 3.3.1 Vehicle Data - Dart Payload Stage 16
  - 3.3.2 Vehicle Data - Booster Stage 17
  - 3.3.3 Launch Parameters 18
  - 3.3.4 Overview of the Initial Inputs 19
- 3.4 Near Real-Time State Vector 19
- 3.5 Integrator Settings 20

4 Methodology of the Pre-flight Nominal Trajectory Model 23
- 4.1 Baseline Model for Environment Selection 23
- 4.2 Environment Model Options 23
  - 4.2.1 Atmospheric Models 24
  - 4.2.2 Gravitational Models 24
  - 4.2.3 Rotational Models 25
  - 4.2.4 Shape Models 25
  - 4.2.5 Wind Model 26
  - 4.2.6 The Environment Model Selection Process 27

4.3 Expanded Model for Impact Point Distribution Analysis 28
4.4 Impact Point Distribution Analysis 28
4.4.1 Monte Carlo Simulation 29
4.4.2 Dispersion Parameters 30
4.4.3 Overview of the Dispersion Parameters 32
4.5 Impact Probability Area 33

5 Results of the Pre-flight Nominal Trajectory Model 35
5.1 Environment Model Selection 35
5.2 The Nominal Trajectory 38
5.3 Monte Carlo Impact Point Distribution 39
5.4 Three-Sigma Impact Probability Area 41

6 Methodology of the In-flight Instantaneous Impact Point Prediction Model 43
6.1 Reference Frames 43
6.1.1 Frame Definitions 43
6.1.2 Frame Transformations 45
6.2 Degrees of Freedom 45
6.3 Environment Model Implementation 46
6.3.1 Atmosphere Model - United States Standard Atmosphere 1976 46
6.3.2 Gravitational Model - J_2 effect 48
6.3.3 Rotational Model - Rotating Earth 48
6.3.4 Shape Model - Ellipsoidal Earth 48
6.3.5 Wind Model - Instantaneous Local Winds 49
6.4 Flight Dynamics. 50
6.4.1 Equations of Motion 50
6.4.2 Input State Vector 52
6.5 Output Compilation 53
6.5.1 Map Representation 53
6.5.2 Numerical Value Output and Visual Indicator 53
6.5.3 Loss of Signal Considerations 54

7 Results of the In-flight Instantaneous Impact Point Prediction Model 55
7.1 Environment Model Implementation and Comparison 55
7.1.1 General Environment Model Implementation and Comparison 55
7.1.2 Local Wind Model Implementation and Scaling Factor 57
7.1.3 Combined Effects of the Environment Model Aspects 58
7.2 Accuracy of the IIP Prediction for a Nominal Input State Vector 58
7.3 Computation Time of the IIP Prediction for a Nominal Input State Vector 61
7.4 Output Presentation 62
7.4.1 Visual Output - Map Projection 62
7.4.2 Numerical Output - Distance to Allowable Impact Area Boundaries 63
7.5 Model Testing for a Different Launch Location 64

8 Sensitivity Analysis 67
8.1 One-at-a-Time Approach. 67
8.2 Parameters of Interest and their Standard Deviations 67
8.2.1 Initial State Vector 68
8.2.2 Selection from the Monte Carlo Dispersion Parameters 69
8.2.3 Sensitivity Analysis Parameter Overview 70
8.3 Results 70

9 Conclusions & Recommendations 73
9.1 Conclusions and Evaluation of the Research Questions 73
9.2 Recommendations for Future Work 74

A Additional Model Inputs **77**
A.1 Sea Level Thrust Measurements . . . 77
A.2 Vacuum Thrust Conversion . . . 78
A.3 Center of Pressure . . . 82
A.4 Drag Coefficient . . . 82

B Analysis of the Full Flight Model **85**
B.1 Monte Carlo Impact Point Distribution for the Full Flight . . . 85
B.2 Evaluation of the Zero Roll Rate Assumption . . . 87

C Verification & Validation **89**

D Transformation Matrices between Reference Frames **91**

E Accelerometer Mechanical Characteristics **93**

References **96**

1

Introduction

At the dawn of the Space Age, both the United States and the Soviet Union were highly invested in winning the Space Race. This competition led to rapid technological advancements and frequent rocket launches. On the 5th of February 1958, the second attempt at launching a Vanguard satellite into orbit took place at Cape Canaveral Air Force Station, following an unsuccessful first attempt two months prior. All seemed well for the first 57 seconds of the flight, as the Vanguard TV-3BU had launched nominally from the launch pad and was on its way to orbit. However, the vehicle then suddenly veered off course due to a severe pitch-down event of 45 degrees. The high aerodynamic and structural loads on the vehicle caused it to break up. This left the responsible range safety officer (RSO) no choice but to send a termination command to the vehicle, destroying it and thereby dispersing the remaining fuel before impact (Bille and Lishock, 2004).

The presence of such a flight termination system on a launch vehicle is still common practice today, as it is one of the most important safety features. A flight termination system (FTS) allows for the vehicle's flight to be terminated in a controlled way, when certain predetermined safety conditions or boundaries are exceeded. It is the one system in a launch vehicle that engineers hope to never use, but are thankful for its presence. Before every launch, a set of criteria is determined which the vehicle and its trajectory must follow. If at any moment these criteria are not met, an FTS provides a solution to prematurely end the flight to prevent harm to people, property or other significant surroundings.

Every vehicle, launch range and company may require a different set of safety criteria to form the foundation of the FTS. This is the case for orbital and sub-orbital launch vehicles alike, which includes sounding rockets like the DART XL by T-Minus Engineering. Sounding rockets are sub-orbital vehicles, typically carrying instruments and payloads used for research and scientific experiments. Considering that they are by definition sub-orbital, an important factor to take into account for their safety constraints is its impact location. Based on this impact location, an advice can be formed for the RSO to base their flight termination decision on.

Creating a reliable, custom FTS based on impact point prediction is no trivial task. Determining a vehicle's expected impact point can be done before a launch, based on the nominal trajectory and expected uncertainties. However, this only provides a distribution of impact point predictions rather than a prediction that corresponds to the vehicle's real-time behaviour during a launch. To reflect this real-time behaviour, instantaneous impact point (IIP) prediction can be applied. This does present the additional challenge of implementing real-time input data and high update rates of the trajectory prediction and flight termination advice, while still retaining a high enough accuracy of the prediction. The purpose of this thesis is therefore designing an algorithm that can accurately predict the instantaneous impact point (IIP) of the DART XL in near real-time during a launch.

1.1. Thesis Objectives

Before starting any research, it is important to clearly and unambiguously define its objective. This research objective can then be used to determine research questions. The goal is to have these questions form a complete overview of the work to be done during the thesis project. This way, answering all research questions will simultaneously lead to completion of the thesis work and achieving the determined research objective.

It is important to recognize that this thesis project is a cooperation with industry, specifically with T-Minus Engineering B.V., a launch provider based in Delft, the Netherlands. A key objective is therefore to meet their requirements and provide a workable end product. However, this is not considered a research objective. In this section, an overview is provided of the research objectives and questions that will serve as the foundation of the academic thesis work. The requirements set by T-Minus are discussed later, in Section 2.5.

1.1.1. Research Objective

In order to gain insight into the relevance and purpose of the thesis project, a research objective is determined. The main research objective (RO) of the thesis is:

RO: *To predict the instantaneous impact point of a sounding rocket's ballistic payload stage in (near) real-time, by creating a flight termination algorithm that predicts this impact point considering impact probability area boundaries and accuracy requirements, in order to increase launch safety.*

The accompanying sub-objectives can be divided into two main areas of interest. The first area of interest is the creation of a nominal model during the pre-launch phase. The purpose of this model is to obtain knowledge on the nominal impact point dispersion to be expected and to create a realistic impact probability area based on this dispersion. This impact probability area can then serve as a guideline for the in-flight phase to compare against predicted impact point coordinates. The second area of interest is the in-flight phase, for which an algorithm is to be developed to run after booster burnout. The purpose of this algorithm is the prediction of instantaneous impact points in (near) real-time and their subsequent comparison to the set impact probability area boundaries. To concisely describe these goals, the following sub-objectives (SO) are presented:

SO-1: *To determine a nominal impact point distribution in the pre-launch phase, by applying an IIP distribution analysis considering the inherently uncertain model inputs.*

SO-2: *To set impact probability area boundaries representative of a realistic launch scenario, by determining the encompassing ellipse of the impact point distribution with three-sigma certainty.*

SO-3: *To create a dedicated algorithm to run during the non-propelled flight phase that predicts the instantaneous impact point of the payload stage, by extrapolating its ballistic trajectory to the surface.*

1.1.2. Research Question

To realize the established research objective and sub-objectives, research questions are formulated. The main research question (RQ) is formulated as:

RQ: *How can the instantaneous impact point of a sounding rocket's ballistic payload stage be predicted, using a flight termination algorithm, to run in near real-time considering the allowable impact area and accuracy requirements?*

By again dividing this into two areas of interest, being the pre-launch phase and the in-flight phase, sub-questions can be determined. The following sub-questions (SQ) are established:

SQ-1: *Which model definitions provide an optimal trajectory solution, considering the requirements for impact point accuracy and computation time?*

  SQ-1.1: *To what extent does the choice of environmental model aspects for the Earth influence the trajectory solution?*

  SQ-1.2: *To what extent does the model's number of degrees of freedom influence the trajectory solution?*

  SQ-1.3: *Can the same model definitions be used for both the instantaneous impact point prediction and nominal trajectory models, in order to meet the individual requirements of each of these phases?*

SQ-2: *Which inputs of the nominal trajectory model are most important to vary in an initial IIP distribution analysis due to their inherent uncertainty, in order to determine the nominal impact point distribution?*

SQ-3: *Which outputs of the instantaneous impact point prediction model should be displayed at the ground station during launch, to allow a range safety officer to monitor the conditions for flight termination?*

1.2. Report Structure

In order to answer the research questions stated previously, the remainder of this report takes on the following structure. First, Chapter 2 presents background information on the company and vehicle, as well as on flight termination systems in general. This chapter also discusses the flight termination state-of-the-art, as well as company requirements. Next, Chapter 3 goes into the models that are developed, their purpose and their input parameters. After defining the two models that are developed and their inputs, Chapters 4 and 5 present the methodology and results of developing of the first model. The methodology and results of developing the second model are presented in Chapters 6 and 7. Chapter 8 then discusses the sensitivity analysis to determine model robustness. Lastly, conclusions and recommendations for future work are presented in Chapter 9. Additionally, Appendices A to E provide supplementary information and will be referenced at the appropriate locations throughout the main body of this report.

2

Background

Before going into the model development and purpose, first the relevant background information is provided. This chapter begins by presenting some background information about the company and vehicle for which a flight termination system is designed, specifically being the DART XL by T-Minus Engineering B.V.. After establishing who it is for, this chapter goes into background information on flight termination systems themselves. This includes commonly used termination methods, both historically and the current state-of-the-art. Lastly, this chapter states the requirements set by T-Minus Engineering for the flight termination system, that informed the design detailed throughout this thesis report.

2.1. Company Profile: *T-Minus Engineering*

The Dutch company of T-Minus Engineering B.V., or T-Minus for short, was founded in 2011 as an answer to the growing interest and demand for suborbital launch vehicles. Their goal is to build high-quality, affordable suborbital rockets that can be used for many different purposes, including commercialising the space industry, aiding the defence sector and flying scientific experiments in microgravity conditions. To realize this goal, T-Minus is working with both national and international partners and customers, all while using in-house development wherever possible.

Past and ongoing projects show that they have already covered a range of applications using various rockets. An example of this is ESA's CanSat competition, the organization of which T-Minus has been a part of ever since the company was founded. This competition allows high school students to design and build their own can-sized satellites. To help the student teams, T-Minus has designed a CanSat kit which provides them with the basic components needed to build their satellite, capable of measuring and transmitting pressure and temperature data. The winning teams get to fly their satellites to approximately 1 km altitude on the T-Minus CanSat launcher, shown in Figure 2.1. This CanSat launcher is a passively guided, single stage vehicle of 3.17 m long and 200 mm in diameter, capable of launching and deploying six CanSats at a time. At the desired altitude, the CanSats are ejected radially to prevent collision with the vehicle. The vehicle itself is equipped with parachutes, giving the possibility for safe recovery and subsequent full re-usability.

Another big project that T-Minus have contributed to is NASA's InSight mission to Mars. Here, they provided a payload as a subcontractor of the German Aerospace Center DLR. The purpose of this payload, the HP3, was to penetrate the Martian surface to a depth of 5 meters. T-Minus aided in integrating and testing the prototypes, proto-flight and flight models, as well as providing support for the development and qualification testing activities.

2.2. Vehicle Profile: *DART XL*

To further realize their vision and expand on the current range of vehicles and capabilities, T-Minus is developing the DART and the DART XL. Following several successful low-altitude flights from the Netherlands, the first T-Minus DART was launched out of Australia in September of 2020. The DART is a space-capable sounding rocket, designed for frequent and affordable missions to the upper atmospheric regions. The vehicle consists of two parts: a solid rocket motor (SRM) encased by a booster

Figure 2.1: The T-Minus CanSat launcher, designed for educational competitions.
[Source: Claude Piscitelli at CanSat Luxembourg 2022]

stage of 2.1 m by 118 mm in diameter, and a payload compartment (Dart) of 1.35 m by 35 mm in diameter, see Figure 2.2. The vehicle is launched from a helical rail, imparting a spin on the vehicle from lift-off to stabilize it in-flight. Additionally, both the booster and the Dart are stabilized by four fins at their tail ends. After booster burn-out, the vehicle separates due to the acting aerodynamic forces. After separation, both the Dart and the spent booster follow a perturbed ballistic trajectory until impact.

Figure 2.2: The T-Minus DART and DART XL vehicles, with the booster in black and the payload compartment in orange.
[Source: T-Minus Engineering archive]

The DART XL, also shown in Figure 2.2 above, is an upscaled version of the DART and therefore has a very similar configuration, also consisting of a solid rocket booster and a dart-shaped payload compartment. The vehicle is currently still in the development and testing stage, during which the solid rocket motor has performed multiple successful static tests. When completed, the vehicle is expected to be capable of reaching in-flight speeds up to Mach 7. In order to reach these speeds, it has a larger size and higher propellant mass than its predecessor. This provides a whole new range of mission possibilities, including reaching exo-atmospheric altitudes. Furthermore, its relatively large payload compartment allows T-Minus to launch multiple, larger payloads than they were previously capable of, along with providing more space for on-board sensors. Table 2.1 provides a comparison of the dimensions and characteristics of the DART XL with respect to its smaller predecessor.

Table 2.1: Comparison of dimensions and characteristics of the DART and the DART XL sounding rockets.

	Dart length (m)	Dart Ø (mm)	Booster length (m)	Booster Ø (mm)	Payload capacity (kg)	Propellant (kg)	Burntime (s)
DART	1.35	35	2.10	118	1.5	19.5	7
DART XL	1.50	70	2.60	215	5.0	100	15

Although very similar in configuration, there is one significant difference between both vehicles. In contrast to the smaller DART, the DART XL does not launch from a helical rail that imparts it with a spin. To stabilize the vehicle during flight, it is actively spun after exiting the launch rail by four spin-motors located on the booster. Furthermore, both the booster and the Dart are equipped with four evenly spaced fins at their tail ends. The vehicle is passively controlled, meaning that there is no way to actively influence its motion after lift-off. During flight, the stage separation occurs aerodynamically after motor burnout. The Dart is held in the booster only by the forces of gravity and drag, with the thrust propelling them both. Therefore, after motor burnout, the drag and gravity of the booster become higher than that of the Dart, causing it to fall away from the Dart for stage separation.

The increased size and capabilities of the DART XL also come with some increased risk factors. Due to its size and calculated capabilities, the potential for high-risk consequences of an in-flight anomaly or trajectory deviation can readily be understood. To protect the people and property directly below and around the vehicle's trajectory, including the launch site, it is therefore of high importance to implement a safety system, such as a flight termination system. Therefore, this thesis will lay the foundation for creating a flight termination system for the DART XL, by developing an algorithm for near real-time impact point prediction relative to a predetermined allowable impact area.

To avoid confusion, it is reiterated that the remainder of this report concerns the DART XL vehicle only. For this vehicle, the entire vehicle is referred to as the DART XL, capitalised in full. The ballistic payload stage is referred to as the Dart, with only the first letter capitalised.

2.3. Flight Termination Systems

This section first describes the order of events during a launch in which an FTS would be triggered. Next, it details the two main types of flight termination systems and the difference between them, before going into various conditions that can lead to flight termination, along with different termination methods. Finally, the current FTS state-of-the-art is described.

2.3.1. Order of Events

For every launch, there is a certain order of events that is generally followed in terms of flight termination. Before a launch, it is important to determine any and all parameters of interest. This can include parameters such as a vehicle's position, velocity, attitude, internal pressure etc. For each parameter, a set of limits or boundaries is then determined within which the values during launch should remain. Therefore, it is also important that all selected parameters are measurable during the launch, for instance by radar or optical tracking, or onboard measurements sent to a ground station via telemetry.

During the launch, these measurements are then continuously compared to the predetermined boundaries. Depending on the type of flight termination system, this is handled either onboard the vehicle or at a ground station where they are displayed and monitored by one or more range safety officers (RSO). If any of the parameters of interest falls outside of its limits, an RSO can manually decide to terminate, or the vehicle can do so autonomously. If none of the parameters fall outside of their limits, the process of measuring and monitoring is repeated for the next time step, until the window within which flight termination may occur has ended.

Within the scope of this thesis, the focus lies on taking incoming vehicle state vector data and processing this to predict its impact point, relative to predetermined impact area boundaries. This prediction is then presented to an RSO, to serve as advice on whether or not the flight needs to be terminated.

2.3.2. Traditional versus Autonomous Flight Termination

There are two approaches to flight termination: range-centric (traditional, human-in-the-loop) and vehicle-centric (autonomous). Traditional FTS involves RSO's, also called mission flight control officers (MFCO's), having to manually give the command to terminate the flight. For an autonomous flight termination system, the rocket performs calculations at every step of the way and can autonomously decide to terminate whenever a boundary condition is exceeded.

Historically, flight termination systems were designed to always include a human in the loop to give the final command. This traditional system includes tracking the vehicle using ground station equipment, such as C-band radar beacons, unaided radar tracking, optics, and incoming vehicle telemetry (National Research Council, 2000). Communication between the ground station and the vehicle is dependent on line-of-sight transmissions, possibly requiring multiple transmitters to be set up at remote locations along the downrange flight path (Bull and Lanzi, 2007). The live incoming data, among which real-time position and attitude data, is then processed and displayed for the RSO to monitor and evaluate. For sounding rockets like the DART XL, this data may also include real-time trajectory and impact point predictions.

Whenever the launch vehicle is observed to stray from its nominal, predetermined conditions, there are two possibilities. If the vehicle has an active guidance system, it may be possible to counter the deviations by performing course corrections (Larson and Wertz, 2005). If the vehicle only has passive guidance, or if the deviation is too large to correct, the RSO is responsible for making the final call on whether or not to trigger flight termination by sending an uplink command (Ferrell et al., 2004). To prevent influence from outside parties, this signal is generally encrypted (Range Safety Group, 2019). The DART XL is not a guided system and it is therefore not possible to use steering to correct its trajectory to avoid flight termination. Figure 2.3a provides a schematic overview of the information flows involved in the decision making process.

Autonomous flight termination systems (AFTS), also called autonomous flight safety systems (AFSS), are a relatively new development in the shift to more automated and autonomous launch vehicles. How it works, is that positioning data, provided by for instance a Global Navigation Satellite System (GNSS) and by inertial measurement unit (IMU) navigation sensors on-board the launch vehicle, is sent directly into the self-contained AFTS for processing. If a violation of flight rules is detected, the AFTS subsystem sends a command to the vehicle to trigger flight termination. Figure 2.3b provides a schematic overview of the information flows involved in the decision making process of an autonomous flight termination system. From the receiving end, this trigger is no different than that of a traditional FTS command coming from a ground station (Valencia, 2019).

A major advantage of an AFTS is that its use can provide substantial reductions in terms of both launch cost and time. For example, the ground segment can be simplified greatly by eliminating the need for equipment such as radars. This leads to a decrease in the time it takes to configure a range prior to a launch, while simultaneously decreasing the probability of malfunctioning ground equipment causing a launch delay. Additionally, placing flight termination functionality on-board the launch vehicle is very useful during periods of signal attenuation. For a traditional system, a loss of telemetry between all ground stations and the vehicle will most often automatically lead to flight termination, as communications must be possible at all times to allow for the FTS to be manually triggered. When using an autonomous system, the vehicle can always determine its own position and execute flight termination independent of telemetry inputs. An AFTS therefore makes it irrelevant whether or not the vehicle can be tracked from the ground at all times (Clark, 2017).

Despite these advantages, however, it is common practice to first fly and test an AFTS repeatedly in 'shadow mode' alongside a traditional FTS. In this shadow mode, it can collect and process data during launch and arm itself accordingly, but it cannot initiate or trigger the actual flight termination process (Fudge et al., 2003). A traditional-autonomous hybrid system, although not common, would also be an option. A potential implementation of this would be a traditional system that operates within the vehicle's line of sight, with an autonomous system to take over outside of this. Taking this into account, the current design for the DART XL FTS is a traditional system. This is the more conventional and less complicated option to start off with, making it the logical choice for implementation on the first iteration of DART XL vehicles, while still leaving the door open for a future transition to autonomous.

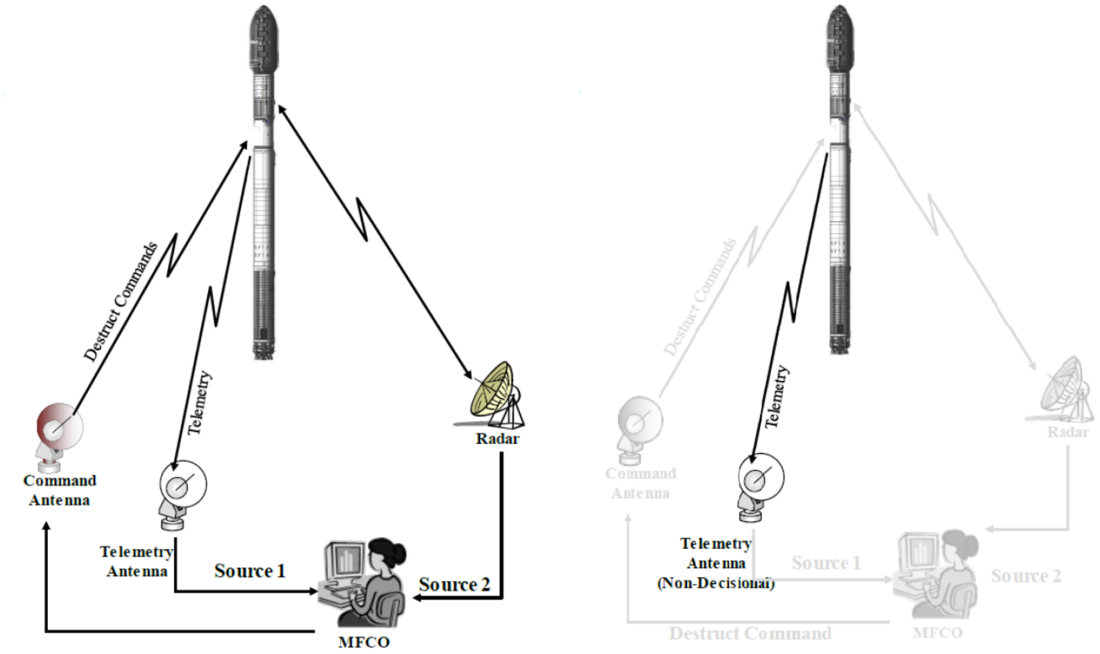

(a) Information flows for the decision making process in a traditional Flight Termination System.

(b) Information flows for the decision making process in an Autonomous Flight Termination System.

Figure 2.3: Information flows for the decision making process in different flight termination systems. [Source: Valencia, 2019]

2.3.3. Flight Termination Conditions

The decision to terminate a flight can be based on many different factors. Mostly they consider whether or not safety, mission and/or legal requirements can still be met. The condition that is focussed on for the thesis work, also being the most common condition for flight termination, is based on deviation from a nominal trajectory. The deviation from a nominal trajectory corridor provides a first indication of the vehicle's behaviour. This corridor is based on the nominal case with acceptable variations and errors in flight conditions such as wind and elevation angle.

For non-orbital vehicles like the DART XL, all stages are expected to impact ballistically within minutes after lift-off. A prediction of the nominal impact point dispersion is therefore often used instead of a full trajectory corridor. For most safety and legal requirements, the impact points of vehicle parts are the most important factors to consider. Focussing on this may therefore allow the RSO to work more effectively. Trajectory deviation and impact point prediction are of course not the only possible termination conditions. Additional termination conditions that may be included in the design of the DART XL at a later stage are a loss of telemetry, loss of critical vehicle systems or stage separation errors. These, however, fall outside of the scope of this project.

To determine whether the vehicle is deviating from a nominal trajectory and subsequent nominal impact area, the nominal case must first be established. The full process of this is described in Chapter 4. Based on a nominal flight, taking local wind variability and input parameter uncertainties into account, an expected impact area can be determined prior to launch. Often, this area is based on the nominal impact areas of vehicle stages and an explosion debris zone. The explosion debris zone represents the area within which debris pieces are predicted to land in the event of a rapid unscheduled disassembly. For the thesis project, the focus will only be on the expected nominal impact distribution. The explosion debris zone is not considered in further discussions. Figure 2.4 provides a visual representation of the selected flight termination condition. A hypothetical vehicle trajectory is shown in white, with its current instantaneous impact point (IIP) prediction at the end of the line. It can be seen that, at this point in the trajectory, the instantaneous impact point prediction intersects with the lower boundary of the allowable impact area shown in red. It would therefore be necessary to trigger the flight termination system to avoid the actual impact point from falling outside of the allowable area.

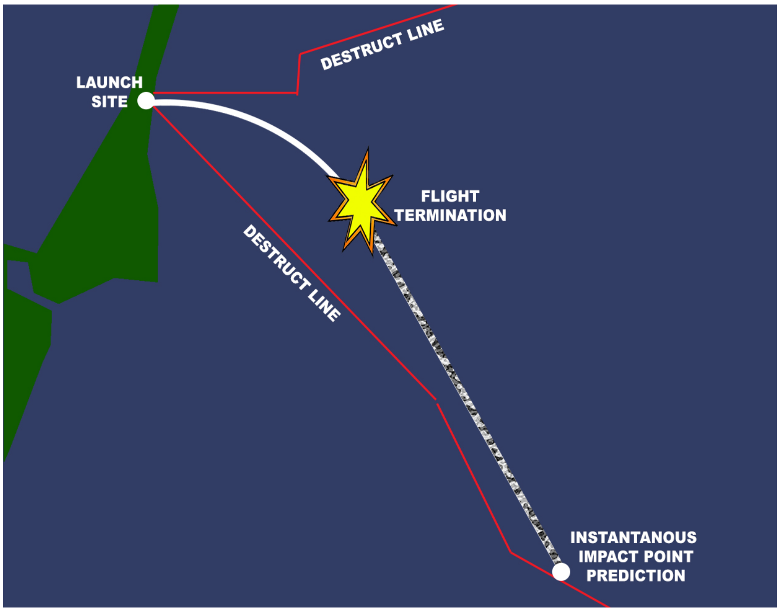

Figure 2.4: Visualization of flight termination based on instantaneous impact point (IIP) prediction.
[Source: Rice, 2015]

2.4. Current State-of-the-art

The previous sections have explained what a flight termination system is and various possibilities for executing flight termination. In this section, the current state-of-the-art is discussed by describing how flight termination technology is incorporated into operational and proposed launch vehicles.

2.4.1. Traditional Systems

The method most commonly found to be used for traditional systems is destruction of the vehicle. Some examples of operational launch vehicles that use this method are ULA's Atlas V and Delta IV Heavy, Northrop Grumman's Antares and Pegasus XL, Arianespace's Vega and Ariane 5, the Japan Aerospace Exploration Agency (JAXA) H-IIA vehicle and Firefly's Alpha.

The user's guides for the Atlas V and the Delta IV configurations specifically mention three reasons for initiating the FTS's destruct sequence: a manual command in case of non-nominal behaviour, an autonomous command if inadvertent break-up is detected, or an autonomous command indicating untimely stage separation (ULA, 2010; ULA, 2013). The FTS has never been used for either of these vehicles, as ULA's mission success rate is currently 100% (ULA, 2022).

The Pegasus XL user's guide describes a similar system, as it can be initiated by a command from the ground or autonomously when sensing inadvertent separation (Northrop Grumman, 2020). Ever since its first mission in 1990, it has only been necessary to terminate two flights; once in 1994 due to a loss of telemetry and once in 1995 due to trajectory deviations (Frick, 2002). For the Antares, the flight termination system has been used once since becoming operational, on the Orb-3 ISS cargo resupply mission. This mission was cut short after only 15 seconds, when the vehicle lost all thrust due to an engine explosion. As a result, the RSO's gave the destruct command to try and minimize damage to the pad and its surroundings as much as possible (NASA Independent Review Team, 2015).

The Vega and the Ariane 5 use a similar destruct system, where range safety officials track the vehicle using radar data and manually sending a destruct command if necessary (Clark, 2020a).

JAXA's H-IIA vehicle again uses a destructive flight termination system (JAXA, 2019). Since its maiden flight, it has been engaged only once in 2003, when one of the two solid rocket boosters failed to jettison. As a result, the vehicle could not reach the desired speed or altitude, causing ground control to terminate the flight 10 minutes after lift-off (JAXA, 2003).

Finally, the Firefly Alpha was confirmed to use a destructive flight termination system during its maiden flight in September of 2021. Here, one of its first stage engines shut down shortly after lift-off, causing the vehicle to start tumbling and finally being terminated by US Space Force (Foust, 2021).

For some vehicles, it is specifically mentioned that the flight termination system uses a combination of thrust termination and destruct capabilities. The user's manual for the Vega launcher, Arianespace (2014), mentions the use of a safety/destruct subsystem, which allows for thrust termination of the SRM's for each stage, instead of vehicle destruction. This removes the potential risk of individual debris pieces, but it would only be possible if the vehicle's remaining ballistic trajectory lies within the predetermined safety corridor (Arianespace and ESA, 2019). The type of termination system for Vega's successor, the Vega C, has not been publicly specified yet. It is however expected to fly using a similar system to that of Vega. It's maiden flight is currently planned for July 2022 (Park, 2022).

Another vehicle that plans to implement these combined capabilities is NASA's upcoming Space Launch System (SLS), with its maiden flight planned for no sooner than August 2022 (Clark, 2022). In the event of termination, the core stage's thrust will reportedly be terminated and the propellant of the SRB's will be dispersed upon destruction (NASA, 2015).

Lastly, examples of this are the Indian Space Research Organisation's (ISRO) Polar Satellite Launch Vehicle (PSLV) and Geosynchronous Satellite Launch Vehicle (GSLV). With this method, the number of fragments from solid stages is kept to a minimum, while the liquid stages are drained of their remaining propellant by engine shutdown and subsequently puncturing the tanks (Gupta et al., 2007). The PSLV has never engaged its flight termination system in the event of a failed launch, and neither have the currently operational GSLV Mark II and Mark III vehicles. Only the GSLV Mark I was terminated by a range safety officer during its final flight in 2010 (ISRO, 2010).

As a final example of vehicle's using a traditional FTS, Astra appears to be the slight outlier by using thrust termination as their only termination method. In September of 2020, their Rocket 3.1 was terminated during its first-stage burn, after which the rocket reportedly impacted and exploded near the launch pad (Foust, 2020). Even more recently in August of 2021, their updated Rocket 3.3 suffered an engine loss at lift-off causing the vehicle to drift horizontally across the launch pad. After allowing the vehicle to continue its vertical flight path up to 50 km and thus moving a significant distance away from the launch pad, the vehicle's thrust was finally terminated due to a deviation from its intended trajectory (Sheetz and Kolodny, 2021).

2.4.2. The Transition to Autonomous Systems

The first rocket launch using live AFTS was performed by SpaceX in February of 2017 (Phipps, 2017). Currently, SpaceX is one of the few launch providers that is able to use an AFTS as their primary safety system and is actively doing so for their Falcon vehicles (SpaceX, 2020).

The capability of using live AFTS is shared by Rocket Lab's Electron and Virgin Orbit's LauncherOne (Burghardt, 2020). Electron debuted an autonomous system on the 'Running Out Of Fingers' mission. This AFTS can terminate a flight by shutting down the vehicle's liquid propellant Rutherford engines (Rocket Lab USA, 2019). It was flown in shadow mode on four flights before making its operational debut on December 6th, 2019.

On May 25th, 2020, LauncherOne's first orbital launch attempt was unsuccessful in reaching space, but it was successful in testing the AFTS. Shortly after first stage ignition, an anomaly occurred that resulted in engine shutdown. After engine shutdown, the AFTS successfully monitored the vehicle's behaviour and position. It was not necessary to destroy the vehicle, as it remained within the predetermined launch safety corridor. Nevertheless, this proves the readiness of the AFTS to terminate the flight at any moment, should the vehicle stray from this corridor (Virgin Orbit, 2020).

Even though there are only a few launch vehicles currently using live AFTS, many launch providers are working on including an autonomous flight termination system into vehicles that are currently still under development. Some examples of this are Arianespace's Ariane 6 and Vega C-light, ULA's Vulcan Centaur and Blue Origin's New Glenn.

The Ariane 6 is expected to make its maiden flight towards the end of 2022 (Park, 2022). In contrast to the Ariane 5, the Ariane 6 has been confirmed to implement an autonomous system. This AFTS will still have similar capabilities to that of the Ariane 5, destroying the vehicle upon termination (Arianespace, 2021). The Vega C-light is a scaled down version of the aforementioned Vega C, designed by removing the first stage and instead modifying the second stage to act as a first stage (Henry, 2017). The Vega C-light is expected to fly its first few missions relying on the traditional system, with this new autonomous system in shadow mode (Mancini et al., 2019).

ULA's Vulcan Centaur's maiden flight was initially planned for 2020, but it is currently on schedule to make its debut in December of 2022 at the earliest (Foust, 2022). Similar to the traditional systems used on the Delta IV and Atlas V, the Vulcan Centaur's AFTS will use vehicle destruction as its termination method (US Air Force, 2019). Reportedly, this allows for multiple launches in one day from the same range with smaller teams needed for each launch (Clark, 2020b).

Lastly, the user's guide for Blue Origin's New Glenn states that the vehicle will incorporate an autonomous FTS, also using vehicle destruct as their termination method of choice (Blue Origin, 2018). Its maiden flight has been pushed to 2023 at the earliest(Foust, 2022).

Additionally, an interesting observation can be made that an increasing number of upcoming launch providers have been deciding to develop flight termination systems in-house, instead of opting for commercially available systems. Some clear examples from the past are SpaceX and Rocket Lab, with both companies developing and eventually successfully flying their own AFTS's. An interesting development in this area is the fact that NASA has released an early software version of their NAFTU (NASA Autonomous Flight Termination Unit) to the launch industry. This allows all US-based launch providers launching from US launch ranges to integrate this AFTS software with their own hardware and have a certified AFTS ready to fly. Rocket Lab is reportedly already using this software on their vehicle's flying from their Wallops launch site (Eggers, 2022).

2.5. Requirements by T-Minus Engineering

T-Minus Engineering falls into the category of companies that aim to develop their own flight termination system. However, they do not have access to resources such as the NAFTU. Therefore, they aim to develop a custom flight termination system for their vehicles. Initially, they aim to develop and flight-prove a traditional, human-in-the-loop FTS for the payload stage of the DART XL. Therefore, this will be the focus of this report.

The first step in developing the FTS is to determine a set of requirements that the system should meet. These are determined in consultation with T-Minus Engineering. Not all of the general system requirements will prove to be directly relevant to the thesis work, but they are nevertheless important to provide a better understanding of the system and its capabilities and limitations. The requirements that will directly guide the thesis work are presented after.

2.5.1. General System Requirements

The system requirements presented here will provide an overview of the full FTS, including the impact prediction software, trigger mechanism and telemetry capabilities. These requirements represent a general overview of the requirements for each aspect of the system, rather than going into specific details. It is important to note here that these requirements shall not contradict those set by T-Minus for their Trajectory Reconstruction Unit (TRU). The TRU is currently being developed in-house, designed to determine a vehicle's state vector in near real-time which serves as an input for the FTS. The following list of system requirements has been formulated in consultation with T-Minus Engineering:

System Requirements (SR):

FTS-SR-01: The system shall be designed to terminate the flight of the 'Dart' payload stage of the DART XL vehicle.

FTS-SR-02: The system shall only be able to initiate flight termination during non-propelled flight.

FTS-SR-03: The system shall operate by altering the aerodynamics of the payload stage, specifically by acting on one or more of the fins.

FTS-SR-04: The system shall be compact, fitting into a 70-mm airframe.

FTS-SR-05: The system shall be fit for use on-board an unguided rocket,
  (a) experiencing loads of up to 60 g's,
  (b) travelling with a speed of up to Mach 7,
  (c) over a trajectory with 150 km altitude and 350 km range.

FTS-SR-06: The system shall be able to predict an instantaneous impact point
  (a) based on the Dart's in-flight state vector,
  (b) with an update rate of 0.1 s or less,
  (c) with an accuracy of 1 km or better.

FTS-SR-07: The system shall be able to integrate with the T-Minus Engineering 'Trajectory Reconstruction Unit' and use its outputs as an initial state vector.

FTS-SR-08: The system shall be able to operate without the input of GNSS data.

FTS-SR-09: The system shall be able to operate both with and without using radar tracking data as an input.

FTS-SR-10: The system shall operate using a secure data link, such that
  (a) no position or trajectory data can be retrieved unsecured,
  (b) no outside signals can trigger and engage the flight termination system.

FTS-SR-11: The system shall have a sub-second response time to incoming termination triggers.

FTS-SR-12: The system shall be able to communicate with multiple ground stations simultaneously and
  (a) monitor its ability to communicate with each involved ground station,
  (b) engage upon receiving a termination trigger from any one station, without interference from another,
  (c) engage if unable to communicate with any ground station.

2.5.2. Thesis Requirements

This section represents only those requirements that have a direct impact on the scope of the thesis work. This includes more in-depth model-specific requirements that are not presented in the previous section of general system requirements. However, to best represent a complete set of thesis requirements, relevant general system requirements are also copied or rephrased into the list below.

Thesis Requirements (TR):

FTS-TR-01: The algorithm shall be active only during non-propelled flight to predict an instantaneous impact point for the 'Dart' payload stage of the DART XL vehicle.

FTS-TR-02: The algorithm shall be able to predict the Dart's instantaneous impact point
  (a) based on the Dart's in-flight state vector,
  (b) with an update rate of 1 s or less,
  (c) by incorporating only input parameters that influence the impact point in the order of 1 km.

FTS-TR-03: The algorithm shall be able to integrate with the T-Minus Engineering 'Trajectory Reconstruction Unit' and use its outputs as an initial state vector.

FTS-TR-04: The algorithm shall be created using software readily available for all involved parties.

FTS-TR-05: The algorithm shall be able to operate without the input of GNSS data.

FTS-TR-06: The algorithm shall run at the ground station during flight.

FTS-TR-07: The algorithm outputs shall, at minimum, be displayed in the form of
  (a) a map representation of current and past impact point predictions, relative to the allowable impact area boundaries,
  (b) a numerical value output, representing the shortest ground distance between the location of a predicted impact point and the allowable impact area boundaries,
  (c) a visual indicator for the numerical value output, to differentiate between impact points inside and outside of the allowable impact area boundaries.

FTS-TR-08: The pre-launch nominal trajectory simulation shall be used to

(a) determine an impact point distribution analysis, based on expected input parameter uncertainties,

(b) determine impact probability area boundaries by taking the three-sigma dispersion range of the determined impact point distribution.

3

Model Definitions and Assumptions

In order to best answer the research questions, two separate models are developed. This chapter briefly describes the purpose of each of these models and the software used to create them. Furthermore, this chapter provides an overview of the different input parameters used in the models. Environment models are presented in Section 4.2 and are therefore not included in this overview. Lastly, to simplify the models, the assumptions of zero lift and zero angle of attack are made.

3.1. In-flight Instantaneous Impact Point Prediction Model

The main focus of the thesis work is the ’in-flight instantaneous impact point prediction model’. The model’s purpose is to extrapolate the trajectory of the DART XL’s Dart payload stage to a predicted impact point, to be evaluated by a range safety officer. The flight termination hardware is placed on the Dart stage only, to be triggered only after stage-separation. Therefore, the in-flight IIP prediction model is only concerned with predicting the ballistic flight of the Dart in the post-separation phase.

The extrapolation will begin from a given input state vector of position and velocity data, provided in near real-time by an external source. To fulfil the model’s intended purpose, the most important aspect to consider is that the model should not only produce an impact point prediction within the desired update rate (requirement FTS-TR-02b), but it should also present this output in a way that can be unambiguously and quickly interpreted by a range safety officer. This is especially relevant when determining which factors to include in the final model, e.g. environment models or integrator settings, in order to provide a good balance between accuracy, computation time and output evaluation.

Since the FTS is designed as a human-in-the-loop system, the impact point prediction model will run at the ground station during launch, instead of for example as an embedded system aboard the launch vehicle. Taking this into account, along with time constraints of the thesis work, it was decided to create the model in MATLAB (version R2020a). MATLAB is a numerical programming environment and interpreted language that is especially suited for running simulations and developing algorithms. Its strength in the areas of data analysis and visualization makes it perfectly suited to present the required outputs.

3.2. Pre-flight Nominal Trajectory Model

The ’pre-flight nominal trajectory model’ serves as a supplementary model for the in-flight IIP prediction model. It is used mainly as a verification tool for various aspects of the in-flight model and for supplying inputs to the in-flight model at different stages of its development.

The pre-flight model was created using an established trajectory simulation software called ASTOS (Analysis, Simulation and Trajectory Optimization Software), version 9.16. ASTOS consists of a graphical user interface (GUI) with defined sections for each part of the model, such as environment, vehicle and launch site definitions. The software also includes many pre-programmed libraries, e.g. common environment models, a launch vehicle database, numerical integration methods and ground station tracking. However, ASTOS is not designed for real-time applications. It is therefore used exclusively in the pre-launch phase to model a nominal launch and accompanying nominal impact point. This nominal trajectory can then be used as a verification tool for the in-flight model, as both models should result in a similar nominal trajectory and impact point if the same input parameters are used.

Because ASTOS is an established software with various pre-programmed libraries, it is an ideal tool for comparing impact point predictions based on different model definitions. The first aspect for which this applies are the environment models, such as gravitational and atmospheric models. This can be quite difficult and time-consuming to implement using MATLAB, whereas ASTOS already has a number of commonly used environment models in its database. Therefore, ASTOS was used for the comparison and selection of environment models, to be subsequently implemented in the in-flight model.

Another important aspect is the capability of performing simulations in batch mode, and thus the capability of easily performing an IIP distribution analysis. This allows a selection of input parameters to be simultaneously varied within the limits of the individual parameter distribution, defined by their mean μ and standard deviation σ. In a batch of many consecutive simulations, each simulation then starts with a different set of starting conditions within the provided parameter distributions. A more in-depth description of the method selected for the IIP distribution analysis and its implementation in this thesis, including a selection of parameters and their uncertainties, is provided in Section 4.4. For the in-flight model, only the end results of the IIP distribution analysis are important as they provide the necessary data to determine the impact probability area. The coordinates of this area are implemented into the in-flight model for comparison to the near real-time impact point predictions and to provide uncertainty boundaries for these predictions.

3.3. Initial Model Inputs

In this section, the numerical inputs for both of the above-mentioned models are introduced. They are grouped into different categories, where it is mentioned wherever necessary if a set of parameters only applies to one of the models. The parameters are based on actual measurements wherever possible, otherwise a best estimation is provided as a model input. The vehicle data for the DART XL is separated into two groups: booster and Dart. A general overview of the vehicle and its purpose was previously presented in Section 2.2.

3.3.1. Vehicle Data - Dart Payload Stage

The unpropelled Dart stage, see Figure 3.1, consists of an orange body tube, a nose- and tailcone and four fins. Its total length from end to end is 1500 mm and its body diameter is 70.0 mm, with a total mass of 14.0 kg. The moment of inertia tensor, as presented below in g/mm^2, was determined in SolidWorks with the number of significant digits as presented. Its point of reference was the point where the axis of symmetry intersects with the bottom of the tailcone. This tensor shows that the vehicle is nearly axisymmetrical, with some small deviations due to for example a hole in body tube where the vehicle's umbilical cable can be connected. For this report, the vehicle is assumed to be perfectly axisymmetric, with its center of mass (CoM) at 796 mm from the tail end, on the axis of symmetry.

$$I_{Dart} = \begin{bmatrix} Ixx & Ixy & Ixz \\ Iyx & Iyy & Iyz \\ Izx & Izy & Izz \end{bmatrix} = \begin{bmatrix} 11353726.29 & 106176.09 & 106183.13 \\ 106176.09 & 10380288986.94 & -3733.44 \\ 106183.13 & -3733.44 & 10380288987.38 \end{bmatrix} \tag{3.1}$$

To define the aerodynamics of the Dart, its drag coefficient (C_D) as a function of Mach number is used as a model input. The full input curve is presented in Appendix A.

Figure 3.1: The DART XL Dart, an unpropelled payload stage.
[Source: T-Minus Engineering archive]

3.3.2. Vehicle Data - Booster Stage

The flight of the propelled booster stage is only simulated in the pre-flight nominal model, and therefore the parameters presented in this section only apply to that model. The booster consists of a body tube, propellant, four fins, nozzle and a transition cone to connect to the Dart, as shown in Figure 3.2. Its total length from end to end is 2920 mm and its body diameter is 215 mm. Its dry mass is estimated at 32.0 kg, with the propellant weighing an additional 100 kg.

The moments of inertia, as presented below in g/mm^2, were again determined in SolidWorks with the number of significant digits as presented. Similar to the Dart payload stage, the booster shows a slight deviation from axisymmetry due to for example the launch lugs attached to the booster casing. For this report, the booster is also assumed to be perfectly axisymmetric. The CoM of the dry booster lies at 931 mm from the nozzle end, along its axis of symmetry. The CoM of all SRM propellant grains combined lies at 1345 mm from the nozzle end. The combined center of mass is therefore 1236 mm from the nozzle end. These centers of mass were also determined using SolidWorks.

$$I_{Booster,dry} = \begin{bmatrix} Ixx & Ixy & Ixz \\ Iyx & Iyy & Iyz \\ Izx & Izy & Izz \end{bmatrix} = \begin{bmatrix} 591647663.54 & -22.42 & -335.97 \\ -22.42 & 62656340953.26 & 0.79 \\ -335.97 & 0.79 & 62656340939.65 \end{bmatrix} \tag{3.2}$$

$$I_{Propellant} = \begin{bmatrix} Ixx & Ixy & Ixz \\ Iyx & Iyy & Iyz \\ Izx & Izy & Izz \end{bmatrix} = \begin{bmatrix} 590702695.77 & 0.00 & 0.00 \\ 0.00 & 226106964025.38 & 0.00 \\ 0.00 & 0.00 & 226106964025.38 \end{bmatrix} \tag{3.3}$$

From static test data, the burn time is estimated at 15.0 s with a specific impulse (Isp) of 241.61 s. A thrust profile is provided in Appendix A. One thing to note here is that ASTOS only accepts vacuum inputs for the thrust and Isp. A conversion from sea level to vacuum pressure therefore has to be done, which results in a new vacuum thrust profile and a vacuum Isp of 264.82 s. The full conversion method and subsequent vacuum thrust curve are detailed in Appendix A.

The booster is only relevant in the pre-flight model before stage separation, as its post-separation trajectory is not modelled. The IIP prediction model only concerns the post-separation trajectory of the Dart payload stage, not of the booster. The aerodynamic coefficients used as inputs are therefore of the DART XL vehicle as a whole, rather than of the booster only. Again, the drag coefficient C_D is presented as a function of Mach number. It is possible for a short delay to occur between the moment of burnout and the moment of aerodynamic stage separation. Therefore, the C_D is provided for a propelled DART XL as well as for an unpropelled DART XL. The center of pressure (X_{CP}) also varies with the Mach number. For this, only the values for the propelled DART XL are known. The rest is left for ASTOS to compute internally. The full input curves are again presented in Appendix A.

Lastly, the booster also contains three spin motors to impart the vehicle with a rotation upon leaving the launch rail. These are located at the bottom of the transition cone at equal distances around its perimeter. Their purpose is to stabilise the vehicle by imparting it with a rotation, which acts as a countermeasure against destabilising factors such as fin and thrust misalignments. The spin motors have their own, separate propellant source, using approximately 48 g of propellant each. This allows them to burn for approximately 2.3 s, based on static test data.

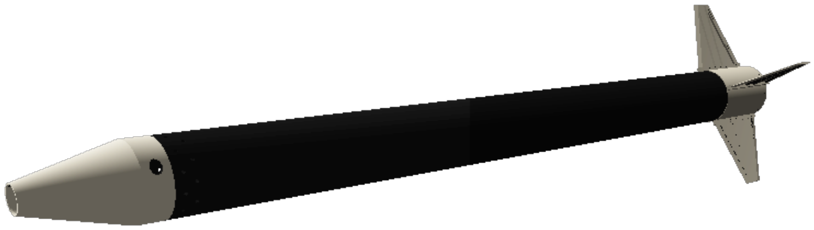

Figure 3.2: The DART XL booster stage, containing the solid rocket motor.
[Source: T-Minus Engineering archive]

3.3.3. Launch Parameters

After defining the vehicle being launched, it is also very important to define the launch parameters themselves. In this section, parameters such as launch coordinates, angles and the allowable impact area are defined.

Launch Site

For the purposes of this thesis, a launch from Andøya Space in Andenes, Norway, is simulated. The launch coordinates are set at $(lat, lon) = (\lambda_0, \Lambda_0) = (69.294167, 16.019444)$ deg. To determine whether the predicted impact points would even allow a launch from this location, they are compared to the boundaries of the allowable impact area. As the name implies, this is the area within which all non-orbital components of a launch vehicle are required to land. In this case, the allowable impact area is based on the impact and recovery area provided for the PMWE (Polar Mesosphere Winter Echoes) launch campaign at Andøya in 2021, during which a T-Minus DART was launched. A visual of this allowable impact area is provided in Figure 3.3a, with a more zoomed out view in Figure 3.3b.

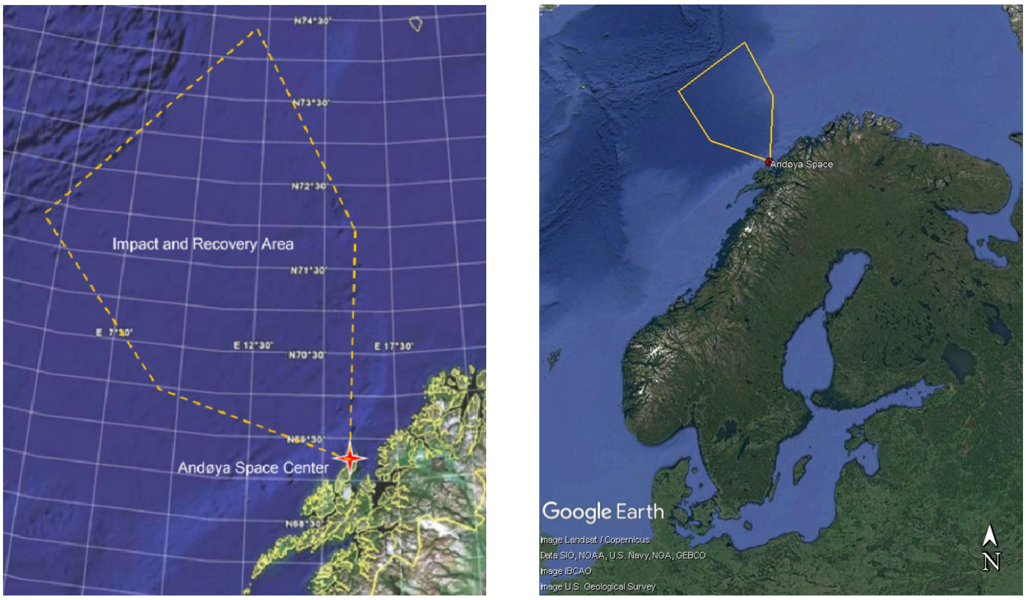

(a) Allowable impact area boundary coordinates. [Source: T-Minus Engineering archive]

(b) Zoomed out view of the Andøya Space allowable impact area. [Source: Google Earth]

Figure 3.3: Allowable impact area for Andøya Space during the 2021 PMWE campaign, where a DART was launched.

Launch Tower

The DART XL will be launched from a launch rail of 9 m long, that can rotate to the desired launch elevation and azimuth. The vehicle will be connected to the rail by means of launch lugs on the side of the booster. Given its launch from Andøya Space, the desired azimuth is set at χ_0 = 324.1 deg based on the azimuth of the aforementioned DART launch at Andøya in 2021. The launch elevation is set at γ_0 = 67.0 deg, which is based on preliminary calculations by T-Minus for a minimum energy trajectory. All elevations stated in this report are relative to the local horizontal. For model simplification, the launch altitude is assumed to be zero.

One important thing to note is that the azimuth can be measured with respect to geographic North or magnetic North. The geographic North, also called true North, is a fixed point on Earth where the rotation axis intersects the Earth's surface. The magnetic North, however, changes slowly over time because it depends on Earth's magnetic field. For Andøya, the difference between geographic and magnetic North, called the magnetic declination, is approximately +8.43 deg[1]. If the azimuth is set using a compass, then this is relative to magnetic North. If the launch tower is a fixed structure, the azimuth is most likely defined with respect to geographic North so that the angle remains constant over time. For the modelled DART XL launch, the azimuth is defined with respect to geographic North.

---

[1] Magnetic-Declination.com (2022). *What is Magnetic Declination?* URL: https://www.magnetic-declination.com/what-is-magnetic-declination.php (visited on 29/04/2022)

3.3.4. Overview of the Initial Inputs

For convenience, the table below provides an overview of all parameters and their values presented in this section. For the moment of inertia tensors, the equation numbers are provided. For parameters consisting of a profile, the relevant figure in Appendix A is given.

Table 3.1: Overview of the input parameters presented in this section.

Parameter	Unit	Value
Dart		
Length	mm	1500
Diameter	mm	70
Mass	kg	14.0
CoM from tail end	mm	796
Moment of inertia tensor Dart	g/mm^2	See Equation 3.1
Drag coefficient	-	See Appendix A
Booster		
Length	mm	2920
Diameter	mm	215
Dry mass	kg	32.0
Propellant mass	kg	100.0
Spin motor propellant mass	g	48
Dry booster CoM from nozzle end	mm	931
Propellant CoM from nozzle end	mm	1345
Nozzle exit area	cm^2	153.9
Dry booster moment of inertia tensor	g/mm^2	See Equation 3.2
Propellant moment of inertia tensor	g/mm^2	See Equation 3.3
Motor burn time	s	15.0
Spin motor burn time	s	2.3
Specific impulse at sea level	s	241.61
Specific impulse in vacuum	s	264.82
Thrust profile at sea level	kN	See Appendix A
Thrust profile in vacuum	kN	See Appendix A
Drag coefficient	-	See Appendix A
Center of pressure	mm	See Appendix A
Launch		
Latitude	deg	69.294167
Longitude	deg	16.019444
Azimuth	deg	324.1
Elevation	deg	67.0
Rail Length	m	9.0

3.4. Near Real-Time State Vector

Last but not least, the vehicle's state vector is required as a model input for the in-flight impact point prediction model in order to update the impact point prediction in near real-time. During a launch, this will be provided by incoming telemetry data and potential other methods of tracking. There are various options to track a launch vehicle's real-time position: space-based, ground-based or vehicle-based methods. The methods considered here are the commonly used methods of GNSS (space-based) and radar systems (ground-based), as well as the vehicle-based Trajectory Reconstruction Unit developed in-house by T-Minus.

Global Navigation Satellite Systems (GNSS)

GNSS, or Global Navigation Satellite Systems, provide global coverage of positioning data by having several satellites simultaneously send positioning and timing data to a receiver. This receiver can be placed anywhere, including inside a launch vehicle. In this receiver, the data is then processed to determine its position and velocity relative to Earth's surface (OxTS, 2020). GNSS is one of the most widely used positioning systems. However, when aiming to track a launch vehicle using GNSS, major restrictions arise posed by the so-called COCOM (Coordinating Committee for Multilateral Export Controls) limits. These limits state that a GNSS receiver must be shut off at speeds above 600 m/s to prevent its use for guidance and navigation of ballistic missiles. Any GNSS receivers able to remain operational after exceeding these limits are export restricted dual-use goods (European Commission, 2022). The DART XL already exceeds this speed after a few seconds, thereby rendering such GNSS receivers inoperative for the vast majority of its flight. Therefore, T-Minus requires that no part of the DART XL shall be dependent on GNSS data, as stated in FTS-SR-08 (Olthof, 2020).

Radar

In contrast to GNSS, radar tracking is a more local, launch specific tracking method, known for its high update rate and high accuracy. Unlike for example optical tracking telescopes, radar signals have the ability to penetrate most atmospheric disturbances, including common weather phenomena such as clouds (Larson and Wertz, 2005). As stated in system requirement FTS-SR-09, the eventual goal for the system is the ability to operate both with and without the presence of radar systems. For the current first iteration of the FTS, however, it was decided to only focus on a vehicle-based tracking system for model simplicity. Furthermore, this allows for a self-contained system, able to operate regardless of the launch facilities at the selected launch range.

Trajectory Reconstruction Unit (TRU) by T-Minus Engineering

A vehicle-based tracking system can be based on different sensors to estimate the vehicle's positioning or attitude, including temperature sensors, pressure sensors, magnetometers, star trackers or Sun sensors. Another option, and arguably one of the most commonly used, is an inertial navigation system (INS). An INS consists of an inertial measurement unit (IMU) and a navigation processor, making it a self-contained system that does not require any external inputs after initialization (Groves, 2013). An IMU typically consists of three orthogonal accelerometers and three orthogonal gyroscopes, coinciding with the vehicle's body reference frame. The accelerometers measure accelerations relative to the surrounding gravitational acceleration and the gyroscopes measure angular velocities (Mooij, 2017).

To determine the near real-time position and attitude of their vehicles throughout the entire flight, T-Minus decided to develop an in-house INS called the Trajectory Reconstruction Unit (TRU). It takes the accelerometer and gyroscope measurements to determine the vehicle's velocity, position and attitude. It is also tasked with storing the in-flight measurements to reconstruct a vehicle's trajectory during post-flight analysis, upon successful recovery. This allows the user to compare the pre-launch model to sensor data and observe possible sensor inaccuracies (Olthof, 2020). A top-level overview of the TRU's capabilities is provided in Figure 3.4.

The FTS is developed to incorporate the outputs of the TRU, allowing for full flight coverage within the line of sight. For the current iteration of the FTS, the TRU's position and velocity outputs serve as the initial state vector from which to extrapolate an impact point prediction. Internally, the TRU uses quaternions to calculate the velocity and position, which are then converted to Cartesian coordinates relative to the launch location. This Cartesian format will be used by the FTS. Each impact point prediction will use the most recent TRU state vector. Currently, the TRU has an update rate of 10 Hz, whereas the desired update rate for the FTS impact point prediction is 1 Hz (FTS-TR-02b).

3.5. Integrator Settings

In order to simulate the trajectory from initial state vector to impact point, an integrator is needed to determine how to update this state vector from one time step to the next. A choice can be made between fixed step-size and variable step-size integrators. Fixed step-size integrators are more suited for objects travelling at a more constant rate. Variable step-size integrators can be used to better accommodate for fast changes in the dynamics. These integrators operate by basing the time step on the dynamics and adjusting it accordingly (Dirkx and Mooij, 2017).

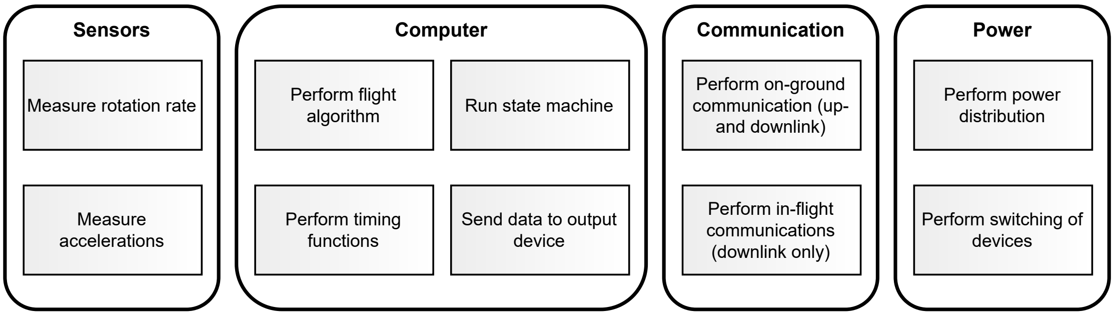

Figure 3.4: Functional diagram of the capabilities of the Trajectory Reconstruction Unit (TRU).
[Source: Figure 3 from Olthof, 2020]

The nominal trajectory model simulates the trajectory all the way from the launch pad to impact, whereas the IIP prediction model only simulates the ballistic trajectory from burnout onward. Therefore, there is a slight difference in the selection of integrators for each model to account for this. Furthermore, it is important to note that the nominal trajectory can be fully modelled prior to launch. There are no significant constraints on the required computation time or processing power that need to be taken into account, other than considering the cumulative effect of running a simulation with a particular integrator in batch mode. Therefore, a decision will be made based on the minimum desired accuracy of the model. The chosen integrator and propagator should be able to meet this requirement, but there is no need to significantly exceed it and use unnecessarily high computing power.

For the pre-flight nominal trajectory model, two different integrators are selected from the options provided by the ASTOS software. During the propelled flight phase, the vehicle moves at such continually high speeds and accelerations that a variable step-size integrator is not advantageous. The only available fixed step-size integrator is Runge-Kutta 4, or RK4. It is therefore selected for the propelled flight phase, with a step-size of 0.01 s. Smaller step-sizes were found to have a higher computation time, without a change in impact point that is significant with respect to the 1 km accuracy requirement. Larger step-sizes were found to have a lower computation time, but the change in impact point was found to be significant with respect to the 1 km accuracy requirement. Therefore, the step-size of 0.01 s was selected considering the balance between accuracy and computation time.

The advantages of a variable step-size integrator become more apparent during the ballistic, unpropelled phase. Here, for instance, the rate of change of the vehicle state at apogee is much smaller than the rate of change near impact. Therefore, a variable step-size can help ensure each of these aspects is integrated accordingly. To select a variable step-size integrator for the ballistic phase, ASTOS provides three options: Dormand-Prince 4/5 (DOPRI 4/5), Dormand-Prince 7/8 (DOPRI 7/8) and MEBDFDAE. The MEBDFDAE (Modified Extended Backward Differentiation Formulae, Differential Algebraic Equations) integrator is only suited for stiff initial value problems, so it can be removed from consideration (Astos Solutions GmbH, 2020b). The difference between DOPRI 4/5 and DOPRI 7/8 is only in their order, with DOPRI 7/8 being of a higher order and therefore of a higher accuracy. To keep a similar order throughout the simulation, and again considering accuracy versus integration time, the DOPRI 4/5 integrator was selected.

For the initial calculations of the in-flight IIP prediction model, an Euler integrator is used with a step-size of 0.01 s. This integrator was selected as it is expected to perform well in terms of low model complexity and low computation time. Whether this step-size meets the requirements is evaluated in the results in Chapter 7. The step-size was selected to be equal to the step-size for the RK4 integrator in ASTOS. In case this combination of integrator and step-size does not result in a model that meets the requirements for accuracy and/or computation time, two things can be done. One option is to change the step-size to decrease the computation time or to increase the accuracy. The second option is to change the integrator from Euler to MATLAB's built-in ode45 integrator. This ode45 integrator implements the variable step-size Runge-Kutta 4(5) method, which only requires the state vector at the time immediately preceding the current one[2].

---

[2] MathWorks (2016). *ode45 - Documentation*. URL: https://nl.mathworks.com/help/matlab/ref/ode45.html (visited on 22/04/2022).

4

Methodology of the Pre-flight Nominal Trajectory Model

This chapter describes the methodology for setting up the pre-flight nominal trajectory model, using the input parameters as described in the previous chapter. First, a baseline version of the model is presented that is used for environment selection. Next, details are provided on the process of using this baseline model to select different aspects of the environment model, along with the options from which the final selection is made. After environment selection, a more complex version of the pre-flight model is presented, that is used to determine the expected nominal trajectory and impact point. Lastly, this nominal trajectory is used as a basis for performing an IIP distribution analysis, from which a 3-σ impact probability area is determined.

4.1. Baseline Model for Environment Selection

In order to compare different environment models to each other, it is necessary to first determine the baseline settings use as a point of reference. Therefore, the baseline model was created using the parameters in Table 3.1 and the simplest option of each of the environment models. All options are presented in the next section, along with an overview of the baseline set of environment models in Section 4.2.6. To fully determine the influence of implementing a certain environment model, the baseline model was set to simulate the entire DART XL flight from launch to impact, instead of only the non-propelled phase.

It is also important to note that the baseline model used for the process of environment selection was chosen to be a less complex version of the pre-flight model version used for the IIP distribution analysis. This allows the baseline model to be used at a later stage for verification of the in-flight IIP prediction model by direct comparison, while still being able to perform the IIP distribution analysis on a more detailed model. The in-flight model is a 3 degrees of freedom model for the Dart payload stage of the DART XL, where the Dart is considered to have a homogeneous mass distribution and zero roll rate. Furthermore, it is assumed that the aerodynamic angles angle of attack, angle of sideslip and bank angle are all constant at zero (see Chapter 6 for more details on these assumptions). By creating a baseline nominal trajectory model in ASTOS using these same assumptions, it can be directly compared to the IIP predictions in MATLAB for the in-flight model to verify the implementation of the selected environment model.

4.2. Environment Model Options

When modelling a vehicle's trajectory, it is important to consider its surroundings. For a suborbital flight, the most important aspects that define an environment model are an atmospheric model, a gravitational model, a rotational model, a planetary shape model, and a local wind model. Given the relatively short duration of the flight, models concerning for example third-bodies or solar radiation are not included. In this section, first the different environment model options are presented, followed by a description of the selection process.

Developing the most accurate and realistic trajectory model means using the most accurate environment model. However, for the in-flight trajectory calculations, maintaining a short computation time is essential in producing (near) real-time results. Therefore, it is also important to not select a model that is overly accurate, as this will only lead to unnecessarily complex models and time consuming computations. To decide which of the described models best suits a DART XL launch model, it is important to consider the software that will be used. In order to avoid having to manually test different environment settings in the IIP prediction model using MATLAB, the considered environment model options are first evaluated using the available presets in ASTOS. Because these models are available as presets and do not require additional user inputs, only a short description of each is provided in this chapter. For the models that are selected for implementation into the IIP prediction model, a more detailed description including the relevant equations is provided in Section 6.3.

4.2.1. Atmospheric Models

A very important model to include in any trajectory calculation is that of Earth's atmosphere, so that the drag caused by its presence can be taken into account. There are two types of atmospheric models: a *standard* atmosphere model and a *reference* atmosphere model. A standard atmosphere represents average, year-round, mid-latitude conditions. It assumes only vertical differences, therefore giving the same results regardless of the input location or time. A reference atmosphere, however, does include variations. It takes into account, for instance, seasonal, temporal, spatial, latitudinal, geomagnetic and solar influences (Mooij, 2017).

For the current iteration of the FTS, the use of a standard atmosphere model is preferred to allow for a change in launch location without altering the model definitions. Multiple standard atmosphere models are available in the ASTOS software database, some of which require user input tables. This section details those options that do not require additional user inputs, for easier transferability to the in-flight prediction model. The options are the exponential atmosphere model, the U.S. Standard Atmosphere 1962 and the U.S. Standard Atmosphere 1976.

The first and simplest atmosphere model is the exponential atmosphere model. The exponential atmosphere model is an isothermal model, meaning that it assumes a constant temperature throughout the atmosphere instead of accounting for variations with altitude. It assumes that the atmosphere is an ideal gas, meaning that the particles are considered to be point masses moving randomly without interactions. Furthermore, to determine the density as a function of altitude, it is assumed that the atmosphere is in hydrostatic equilibrium. Equations 4.1 and 4.2 present the ideal gas law and the hydrostatic equilibrium equation respectively. Here, p is the atmospheric pressure in Pa, ρ is the atmospheric density in kg/m^3, T is the temperature in K, h is the altitude in m, g is the gravitational acceleration in m/s^2 and $R = 287.058$ J/(kg K) is the specific gas constant for air.

$$p = \rho R T = \rho \frac{R^*}{M_a} T \tag{4.1}$$

$$dp = -\rho \; g \; dh \tag{4.2}$$

In contrast, the U.S. Standard Atmosphere 1962 (US62) and 1976 (US76) models are not isothermal models. Rather, they are based on temperature measurements throughout the atmosphere, performed by weather balloons, sounding rockets and satellite remote sensing data. Other variables, such as pressure, density and atmospheric composition are then determined from this using physical equations to best fit the available experimental data (AIAA, 2010). The US76 model is an updated version of the US62 model, with slight revisions mostly at higher altitudes, due to an increased inventory of experimental data (NOAA, 1962; NOAA, 1976). Given the temperature distribution, equations for other atmospheric parameters such as density can be determined based on this distribution, the ideal gas equation and the hydrostatic equation above.

4.2.2. Gravitational Models

When modelling Earth's gravitational field, there are two main options; to assume the body is a point mass or to model it using spherical harmonics. The point mass approximation assumes a central gravity and is therefore the most basic gravitational model that can be used. When assuming that both the Earth and the launch vehicle are a point mass, Newton's law of gravitation can be used to describe the gravitational force between them. This law can be simplified by assuming that the mass of the Earth is much greater than that of the DART XL. The law of gravitation is then used to directly compute the gravitational acceleration, using Equation 4.3. Here, g_r is the gravitational acceleration in m/s^2 in radial direction and r is the distance between the vehicle and Earth centres of gravity in m. Lastly, the geocentric gravitational constant μ_E for Earth is defined as $\mu_E = 3.9860047 \cdot 10^{14}$ m^3/s^2 (Mooij, 2017).

$$g_r = \frac{\mu_E}{r^2} \tag{4.3}$$

The point mass model is most commonly used in situations where a body's presence only results in third-body perturbations (Mooij, 2017) This is not the case for a DART XL launch, where the Earth's gravitational pull is of great influence on the vehicle's motion. For a more complex and detailed gravity model of Earth, a spherical harmonics model allows for a more detailed representation of its non-homogeneous, non-symmetric mass distribution and the resulting variations in the gravitational field. The full spherical harmonics equations contain parameters for the degree n and the order m of the model. Both the degree and order can be quite large, with the maximum degree and order supported by ASTOS being 150 (Astos Solutions GmbH, 2020a).

As this can quickly lead to a very complex and computationally intensive gravitational model, often the assumption is made to only include the second degree zonal coefficient 'J_2' to the central gravity term. This is the largest spherical harmonics coefficient by at least three orders of magnitude, and is therefore considered to be the primary perturbation in low-Earth orbit. It represents the gravitational effect of Earth's oblateness, where a larger percentage of mass is located at equatorial latitudes (Astos Solutions GmbH, 2020a; Wertz, 2009). As a result, the vehicle will experience a small perturbation in the radial direction (pointing away from Earth's center) as well as in the latitudinal direction (North to South). For zonal coefficients the order $m = 0$, meaning that they are independent of longitude.

4.2.3. Rotational Models

For flights of a short duration, often the assumption of a non-rotating Earth is made. The Earth rotates at a constant rate of 360.9856235 deg/day, or $\omega = 7.29212 \cdot 10^{-5}$ rad/s (Seidelmann et al., 2007). It is therefore mostly relevant for longer duration flights or satellite missions, but can still be of influence for a shorter duration flight like the DART XL.

When assuming a non-rotating Earth, this means that the Earth's surface and its atmosphere are stationary, with the launch vehicle being the only moving component. If the Earth's rotation is considered, both the motion of the surface itself as well as the co-rotation of the air in the atmosphere are important. This is represented by taking into account the Coriolis force and relative forces like the centripetal force. As a result, the latitudes and longitudes on which the trajectory's ground track is projected shift at every time-step. This ultimately leads to a change of impact latitude and longitude with respect to a non-rotating Earth.

4.2.4. Shape Models

There are many different available shape models for Earth, with varying levels of accuracy. The considered shape models are a spherical Earth and an ellipsoidal Earth. Any models that include local variations or topography, such as the geoid model or a digital elevation model, are not considered. Due to their increased accuracy, these models are also expected to greatly increase the complexity of a trajectory model, thereby negatively influencing the development time and the computation time of the end product. A flat-Earth model is not considered due to a lack of accuracy when implementing it for larger downrange distances, like the maximum expected nominal flight range of 350 km.

Both the spherical and ellipsoidal Earth models are simplified assumptions of the Earth's non-uniform shape. For a spherical Earth model, the Earth is assumed to be perfectly round with a constant radius equal to Earth's mean radius of R_e = 6371 km (Larson and Wertz, 2005). Ellipsoidal models are considered to be more realistic than a spherical model, as they include a slight flattening effect caused by the Earth's rotation. This results in the shape of an ellipsoid, or oblate spheroid. Based on the IERS89 ellipsoidal model, the equatorial radius is $R_{e,eq}$ = 6378.136 km, the polar radius is $R_{e,pl}$ = 6356.751 km and the flattening factor, or ellipticity, of $f = 1 - R_{e,pl}/R_{e,eq} \approx$ 1/298.257 (Mooij, 2017). This change in shape comes with a change in definitions for altitude and latitude, which can subsequently cause a change in the predicted impact point coordinates.

4.2.5. Wind Model

The final aspect of the environment model that is considered is a wind model. Due to the high variability over time and location, wind is arguably the hardest environmental aspect to describe in model form. Leading up to a launch, it is common practice to continuously monitor the local winds and use the latest data as an input for a trajectory and impact point prediction model. However, to get a general idea of the influence of wind on the DART XL's behaviour at an earlier stage, a wind model is included in the nominal trajectory model. For the final environment model, the consideration is whether including a wind model is necessary to improve the trajectory model's accuracy. Therefore, the impact point prediction of a model without wind is compared to that including a wind model. The local wind model used in this comparison is detailed below.

The source of the wind data used is the ECMWF (European Centre for Medium-Range Weather Forecasts) Copernicus Climate Data Store. The ERA5 database was selected from the data store, which is a fifth generation ECMWF reanalysis of global climate and weather (ECMWF, 2019). This database combines model data with measurements to produce a best estimate of the actual conditions, dating all the way back to 1979 up to the present. One thing to note here is that this database does include measurements for vertical wind velocities. For the thesis work, only horizontal winds are considered for simplicity.

To account for the variability of winds over time, but to not include all data dating back to 1979, it was decided to use a dataset covering the past 10 years. Furthermore, monthly averaged data was selected over using hourly data. This is expected to give a sufficient estimate of the expected wind conditions, while substantially decreasing the size of the dataset. The seasonal variability is considered to be much higher than the annual variability, as confirmed by Basse et al. (2021) for ERA5. Therefore, to further decrease the dataset size, the monthly averages for the selected decade are averaged again to present one overarching average per month. As a final step, the month of October is selected because it was identified by T-Minus as a likely potential month for a future DART XL launch.

To account for the high wind variability depending on location, a local wind model is preferred over a more global model. To encompass the whole allowable impact area, the selected coordinates for the local wind model lie between $69° - 75°$ N and $4° - 17°$ E. The boundaries of this area are shown in Figure 4.1 relative to the allowable impact area. Within this range of latitudes and longitudes, the ERA5 datapoints form a grid spaced at 0.25 deg in both directions. For further simplicity, the gridpoint closest to the launch coordinates is selected. At these coordinates, $(lat, lon) = (69.25, 16.0)$ deg, the model should cover winds at ground level, as well as at various altitudes. The wind influence is the greatest during the first part of any launch, due to a phenomenon called weather cocking which is very common for unguided and statically stable vehicles. Weather cocking occurs in the presence of winds perpendicular to the direction of flight, as the vehicle's static stability will try to reduce its angle of attack. Since no course corrections can be applied, the vehicle's nose will rotate into the wind (Wittenberg et al., 2016). This can have a very large effect on the trajectory and subsequent impact point, so it is therefore crucial to take winds at altitudes above ground level into account. ERA5 takes into account winds up to approximately 35-40 km, which is the commonly used maximum altitude that standard latex weather balloons are capable of reaching (Safonova et al., 2016).

Summarizing, the selected dataset consists of an average for the month of October from the year 2012 to 2021. It covers altitudes up to approximately 40 km at $(lat, lon) = (69.25, 16.0)$ deg. The ERA5 dataset provides this data relative to pressure levels from 1000 hPa to 1 hPa. The geopotential in m^2/s^2, the Northward wind in m/s and the Eastward wind in m/s are provided for each pressure level. Throughout this report, $V_{w,N}$ describes the wind blowing towards the North (true North) and $V_{w,E}$ describes the wind blowing towards the East. Subsequently, a negative sign for either means wind blowing towards the South or West respectively. In case it is needed for future analysis, temperature data in K is also available at the pressure levels. Figure 4.2 shows the final wind profile that is used.

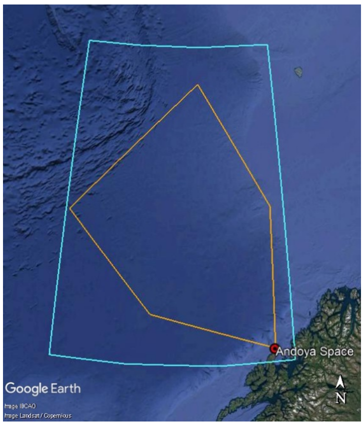

Figure 4.1: Local wind area (blue) with respect to the allowable impact area boundary (orange). [Source: Google Earth]

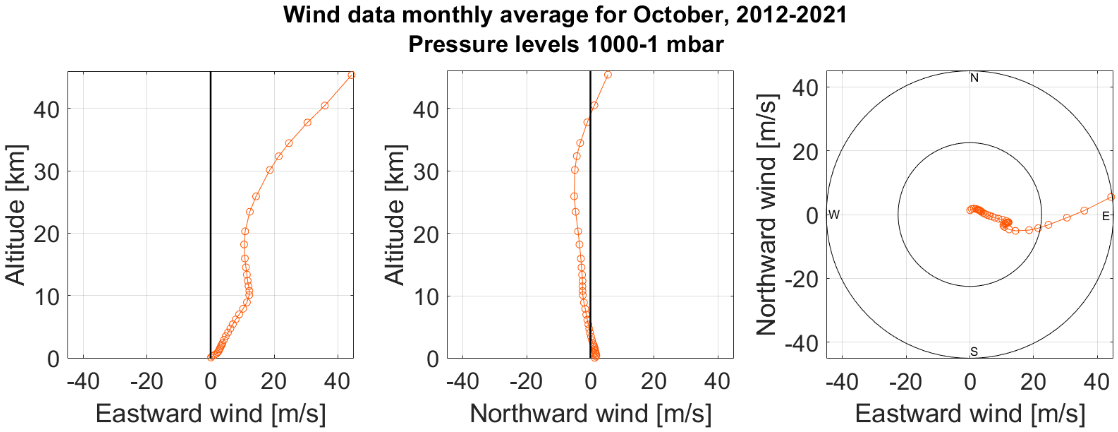

Figure 4.2: Wind profile data, as analysed from the ERA5 database for the Andøya launch site.

4.2.6. The Environment Model Selection Process

The comparison and selection process is the same for each environment model aspect, with the baseline environment model acting as the starting point in each case. This baseline model consists of the aspects that make up the simplest version of the environment model. To observe the effect of changing individual environment model aspects, only one aspect is varied at a time with the rest of the aspects remaining at their baseline condition. The results of each variation are then compared to the baseline for each aspect, to determine the minimum required complexity of that aspect to meet the IIP accuracy requirement of 1 km. To compare these results with respect to the accuracy requirement, the distance between impact point coordinates is used. If the difference between two options for an environment model aspect is large compared to the required IIP accuracy of 1 km, then the more complex option is selected. If the difference is small, then the added complexity is not considered to be worth the increase in accuracy and the less complex option is selected. Table 4.1 provides the set of baseline environment model aspects and an overview of all investigated options as presented above.

Table 4.1: Baseline environment model selection and alternative options.

Environment Model Aspect	**Baseline**	**All Options**		
Atmospheric Model	*TBD*	Exponential	US62	US76
Gravitational Model	Point mass	Point mass	J_2 Coefficient	Spherical Harmonics
Rotational Model	Non-rotating	Non-rotating	Constant Rate	
Shape Model	Spherical	Spherical	Ellipsoidal	
Wind Model	No Wind	No Wind	Monthly Average	

As shown in this table, the choice of baseline atmospheric model is left 'To Be Determined'. As previously mentioned, part of the goal of the environment selection results is to allow verification of the in-flight IIP prediction model. The verification can be done by comparing the change in impact point caused by different environment model definitions. In order to compare this change between the in-flight model and the pre-flight baseline model, the same baseline environment model should be used.

For most considered environment model aspects, changing from the baseline to a different option would only require a possible addition to the existing in-flight model because each option builds on the previous. For example, including the influence of the J_2 coefficient still uses the point mass model as a foundation. However, the atmospheric model is the exception because changing the atmospheric model would require replacing part of the in-flight model. Individual atmospheric models can be quite time-extensive to manually implement in the in-flight model, so this is preferably avoided. Therefore, the atmospheric model is selected first. The rest of the comparisons will then be done relative to a baseline using this selected atmosphere model.

4.3. Expanded Model for Impact Point Distribution Analysis

To best evaluate the effect of varying parameters, an IIP distribution analysis is performed on an expanded, more realistic version of the pre-flight nominal trajectory model. At this point, the simplifications of the baseline model are no longer necessary, because the trajectory model used to perform the IIP distribution analysis will not be compared to the in-flight IIP prediction model. Of this model, two versions are created. One version takes into account the full flight from launch to impact, while the other only considers the ballistic phase of the launch between motor burnout and impact. The model definitions are identical for both, except for the initial state vector. For the full flight model, the initial state is stationary at the launch pad. For the ballistic flight model, the initial state is taken to be the point of motor burnout from the full flight model. This way, the IIP distribution analysis can be performed for both versions. The full flight IIP distribution analysis provides insight into the uncertainty of the whole pre-flight nominal trajectory model, and thus the uncertainty of the nominal impact point. This not only helps determine the robustness of the model, but can also aid T-Minus in determining suitable launch sites and focussing on those parameters that affect the impact point uncertainty the most. The ballistic flight IIP distribution analysis, on the other hand, mostly provides insight into the uncertainty of an impact point based on an in-flight state vector. This is especially relevant to take into account at a later stage, when discussing the results of the in-flight IIP prediction model.

For both versions, the IIP distribution analysis only concerns the uncertainty of the initial state vectors of burnout for the ballistic model and launch for the full flight model. During an actual launch, the uncertainty of course applies to every state vector throughout the entire flight. These subsequent time steps are not considered here because the IIP uncertainty is expected to be largest at these initial state vectors, where the time remaining for propagation of parameter uncertainties is largest.

The first factor differentiating this more realistic version from the baseline model version is the fact that all aspects of the environment model have been selected and implemented. Furthermore, the vehicle has a more realistic, non-homogeneous mass distribution, meaning that the centers of mass and moments of inertia are implemented accordingly based on the data presented in Sections 3.3.1 and 3.3.2. To allow more degrees of freedom for this non-homogeneous vehicle, the aerodynamic angles are no longer constrained at zero. To represent stage separation, an additional flight phase is added between motor burn and ballistic flight. Due to the DART XL's aerodynamic separation method, the moment of separation does not necessarily coincide with the moment of motor burnout. The delay between burnout and separation, called the separation time, is therefore modelled by adding in a flight phase in which the vehicle is no longer propelled, but not yet separated. In this case, the drag data for the unpropelled, full vehicle is implemented. Lastly, ASTOS provides the option to account for the jet damping effect caused by the exhaust plume, that gives the vehicle a slight resistance to attitude changes. Since this effect can have a non-negligible influence on the behaviour of smaller vehicles, it is included in this expanded model version (Astos Solutions GmbH, 2020a).

One factor that is not altered between the baseline model and this expanded model is the fact that Dart payload stage is considered to have a zero roll rate during its ballistic flight. When performing thousands of simulations for the IIP distribution analysis, this assumption can enormously decrease the total computation time while not significantly affecting the resulting impact distribution and impact probability ellipse. This assumption can be made because the main purpose of the spin motors during a launch is to stabilise the vehicle by counteracting destabilising factors such as fin and thrust misalignments. Such destabilising factors are not included into this first iteration of the trajectory model and thus the roll rate of the Dart stage serves no immediate purpose. The roll rate of the full vehicle at lift-off is not negligible, as this still acts as a stabilising factor against low-level winds. For verification of this assumption, see Appendix B which presents a more in depth analysis on the results of the full flight IIP distribution analysis, including a comparison of simulations with and without enforcing a zero roll rate for the Dart.

4.4. Impact Point Distribution Analysis

As previously mentioned, an impact point distribution analysis is performed to understand the effect of expected parameter uncertainties and gain an understanding of the vehicle's most likely behaviour. It is very difficult to determine the uncertainty of the impact point on its own. Therefore, it is determined by taking into account the uncertainties of the input parameters and how these uncertainties propagate throughout the trajectory to finally give an estimate of the impact point uncertainty. For this reason, the Monte Carlo method is selected to analyse the pre-flight nominal trajectory model and subsequent nominal impact point. This section will first provide a general understanding of the Monte Carlo method, before listing the dispersion parameters and their uncertainties. Finally, it describes how to analyse the Monte Carlo results and how to determine an impact probability area from this.

4.4.1. Monte Carlo Simulation

Monte Carlo simulations are used to determine the combined effect of randomly varying a set of parameters within their individual uncertainty boundaries. Using ASTOS, this is done using its 'batch mode' capability. This capability allows for a single simulation to be run repeatedly in sequence, with different input parameter values for each run. This way a selection of input parameters to be simultaneously varied within the limits of the individual parameter distribution inputs.

A parameter distribution is defined by a mean value and a standard deviation (1-σ), based on the estimated parameter uncertainty. Most often, the parameter distributions are Gaussian in nature. The parameter's input value is then randomly selected from this distribution at the start of each individual run. For the actual Monte Carlo simulation, a batch of runs is performed sequentially, using a different set of randomly selected parameter inputs for each run. The result of such a Monte Carlo analysis is a distribution of impact points, that represent the spread caused by input parameter uncertainty (Nassiri et al., 2004). The spread is represented by the individual impact point latitudes and longitudes. From this spread, the impact probability area is determined as the ellipse within which there is a 99.7% (3-σ) chance of impact (see Section 4.5). Finally, the coordinates of the impact probability area are implemented into the in-flight model for comparison to the near real-time impact point predictions and to provide uncertainty boundaries for these predictions.

One key variable that has not been mentioned yet, is the number of runs within a batch sequence. In order to have some confidence in the results of the analysis, a certain minimum number of runs is required. However, it is also not desirable to perform an unnecessarily large number of runs as this can be very time consuming. Monte Carlo simulations do not have an inherent upper or lower limit for the number of runs required for a certain level of confidence. Therefore, a convergence test is performed to determine whether or not the impact point distribution converges to a single point. This convergence test is done for both the impact point latitude and longitude separately, by determining the overall mean value after every new run. According to Engelen (2012), which uses a very similar Monte Carlo simulation process, at minimum a few thousand runs are needed for the mean IIP coordinates to converge at a sufficient level of confidence. Therefore, the initial number of runs is set at 25000 to ensure convergence and to determine the approximate number of runs required to reach convergence.

As an additional step, the cumulative average of this simulation is compared to a 3-σ confidence interval for the simulation. The goal of this confidence interval is to determine the confidence in a single Monte Carlo simulation and its expected variability with respect to potential additional simulations with the same number of runs. To define this confidence interval, it is first necessary to determine the standard error of the mean. This standard error is the variability *across* multiple samples, in contrast to the standard deviation which describes the variability *within* a certain sample. The standard error is calculated using

$$SE = \frac{\sigma}{\sqrt{n}} \tag{4.4}$$

where σ is the standard deviation of a single sample and n is the number of runs within this sample. The 3-σ confidence interval is then defined as the interval

$$\left[\mu_{MC} - 3\frac{\sigma}{\sqrt{n}},\ \mu_{MC} + 3\frac{\sigma}{\sqrt{n}}\right] = \left[\mu_{MC} - 3\ SE,\ \mu_{MC} + 3\ SE\right] \tag{4.5}$$

where μ_{MC} is the cumulative average after each run within the Monte Carlo simulation. After determining whether the Monte Carlo simulation consists of enough runs to converge to a single point with a sufficient level of confidence, the simulation is repeated with a different random seed. This is done to verify that the simulation will again converge to a point close to the original mean value, within the confidence interval (Higham, 2004; Engelen, 2012).

4.4.2. Dispersion Parameters

To perform a Monte Carlo analysis, it is necessary to first select the parameters to vary. These parameters are referred to as the dispersion parameters. To determine which model input parameters to include as dispersion parameters, it is first important to take into account the capabilities and limitations of the ASTOS software. Some parameters are not a direct user input, but rather they are calculated internally based on other user input parameters. Additionally, some parameters cannot be altered because they are part of a fixed preset. By design of the ASTOS software, it is therefore not possible to include such parameters as dispersion parameters. Another assumption is that the dispersion parameters are not aimed at determining the effect of uncertainties on design parameters such as vehicle length or mass, as these can be accurately determined before a launch for the specific vehicle that is flown.

To limit the computation time of the Monte Carlo simulation, the number of dispersion parameters was limited. Parameters that are not included are either presumed to not have a large effect on the impact point dispersion or they are not considered as primary parameters of interest for this iteration of the trajectory model. The final set of parameters and accompanying uncertainties presented below were determined in consultation with T-Minus. Most parameter distributions are Gaussian, with exceptions mentioned. For a brief overview of all the parameters and their mean and standard deviations, see Section 4.4.3. This section also clearly shows the distinction between the parameters used for the full flight Monte Carlo analysis and those used for the ballistic flight Monte Carlo analysis.

For the ballistic flight, no additional uncertainties are placed on the post-burnout state vector. Only those parameters are considered that influence the trajectory from a given initial state vector onward. For the Monte Carlo analysis, the TRU measurements are therefore considered to be an accurate representation of the vehicle's current state vector without uncertainty. The effects of state vector uncertainties on the impact point prediction are evaluated in the sensitivity analysis in Chapter 8.

Environment

For the environment model, there are only a few parameters that can be varied within the software. These are the atmospheric density scaling factor for the selected atmospheric model and scaling factors for the magnitudes of the Eastern and Northern winds. All three parameters are scaling factors. Their mean value is therefore set at a scaling of 1.0. According to Nassiri et al. (2004); Engelen (2012), the uncertainty of parameters in a standard atmosphere model is assumed to be 5%. Here, this only applies to the scaling factor for density as a function of altitude.

Wind is a much more unpredictable input, where an average value is used as an input that does not accurately reflect possible extremes like high wind gusts. Therefore, a uniform distribution is selected with a 1-σ of 16.7% uncertainty. This way, the maximum values of approximately 3-σ lie between 50% and 150% of the original value for the Northerly and Easterly winds. This assumption does limit the directions in which the wind can blow to those presented by the average wind profile, as no sign change will occur within these uncertainties.

Motor and Propellant

For the vehicle's SRM, the considered parameters are the propellant CoM, initial propellant mass, residual propellant mass and a scaling factor for the thrust and specific impulse. Thrust alignment uncertainties are not considered. The CoM is considered only in the x- and y-directions as defined by the body-fixed frame (Section 6.1), where the x-direction goes through the vehicle's symmetry plane and through the nose. Given that $COM_{p,x}$ is defined with respect to the nozzle end and $COM_{p,y}$ is defined with respect to the rotation axis, the mean CoM lies at $(COM_{p,x}, COM_{p,y}) = (1140, 0.0)$ mm. This CoM was determined using an existing SolidWorks vehicle model. The standard deviations are set at 5 and 1 mm respectively. Variations in the z-direction are not considered due to the vehicle's rotational symmetry and high rotation rate, which would yield identical results to varying only the y-direction.

For the initial mass of the propellant, not considering the booster casing, the nominal value was already determined to be 100 kg. This value is therefore used as the mean. The standard deviation is set at 0.1 kg, based on the experience T-Minus has producing this propellant.

For the residual propellant mass at the end of the burn, the ideal nominal mean is 0. However, this is generally not the case and can also be confirmed by the available static test data. The standard deviation is therefore set at 1 kg. For a positive residual propellant mass, this means that not all propellant has been used up. For a negative residual propellant mass, this means that a certain amount of structural mass has been expelled, for example the propellant casing.

The thrust and specific impulse are individual model inputs in ASTOS, meaning that scaling one of these inputs does not automatically affect the other. To avoid highly unlikely simulations, for example a positive thrust scaling factor and a negative specific impulse scaling factor, the only option is to scale them both with the same factor at all times. Due to the limitations of the ASTOS software mentioned in Section 3.3.2, this scaling factor is applied to the vacuum thrust and vacuum specific impulse. However, this is not an issue as multiplying the vacuum data by a certain factor results in the sea level data scaling with the exact same factor. Because the Monte Carlo parameter is a scaling factor, its mean is 1.0. The standard deviation is set at 5%, based on the variation between multiple static tests.

Mass

The masses considered here are the dry, structural masses of the booster and the Dart payload stage. The nominal structural mass is 32.0 kg for the booster and 14.0 kg for the Dart stage. Following the method in Engelen (2012), the standard deviation for both is set at 1%. For the CoM of the booster and Dart, a similar definition is used as for the propellant CoM described above. This means defining it in the body-fixed frame and neglecting the z-direction. Again, they were determined using an existing SolidWorks vehicle model. Given that $COM_{b,x}$ is defined with respect to the nozzle end and $COM_{b,y}$ with respect to the rotation axis, the mean CoM lies at $(COM_{b,x}, COM_{b,y}) = (931, 0.0)$ mm. The standard deviations are set at 20 mm and 1 mm respectively. Lastly, the mean CoM for the Dart lies at $(COM_{d,x}, COM_{d,y}) = (796, 0.0)$ mm, with $COM_{d,x}$ defined with respect to bottom of the Dart stage's tailcone and $COM_{d,y}$ with respect to the rotation axis. The standard deviations are set at 6 mm and 1 mm respectively. In both cases, the standard deviation for the CoM in x-direction was estimated by taking the relevant component's structural mass $\mu \pm 1\sigma$ and adding it all to one end of the component. The resulting shift in CoM was taken to be the standard deviation of this CoM.

Aerodynamics

All available aerodynamics data was introduced in Chapter 3, which consisted of the center of pressure X_{CP} of the DART XL, and the drag coefficient C_D with respect to Mach number for the powered DART XL, unpowered DART XL and the Dart as determined by T-Minus. In ASTOS, these individual coefficients can only be altered by a scaling factor. Therefore, the mean scaling factor for all coefficients is set at 1.0, meaning no scaling with respect to the input values. The coefficients were all determined using modelling software, which makes it difficult to estimate a standard deviation. Looking at the methods in Nassiri et al. (2004); Engelen (2012), the value was estimated to lie between 5-10%. The more conservative value of 10% was selected as the standard deviation of the aerodynamic coefficients, as T-Minus have indicated their drag coefficient data to be on the conservative side as well.

Launch

The launch parameters considered here are the initial angles and the rail length. As established, the launch angles of azimuth and elevation are set at 324.1 deg and 67.0 deg respectively. These values are used as the mean values for the full trajectory model. However, for the ballistic version of the model, the initial angles are equal to the angles at motor burnout, not at launch. Based on the state vector at burnout for the full model, the mean initial angles for the ballistic phase are an azimuth of 324.017 deg and an elevation of 65.435 deg.

Multiple factors can cause an uncertainty in the launch angles, the first being the measurement method. Launch angles are often measured manually, for instance with a compass or theodolite. A compass measures the azimuth relative to magnetic North, with accuracies between 0.25-1 deg, whereas a theodolite measures the angle between two user-defined points with accuracies up to 0.1-1 mgon. Another potential cause of uncertainty are ground level winds making the launch tower slightly sway in the wind, and the weight of the launch vehicle resulting in a slight deflection angle in the estimated elevation angle. All these uncertainties are difficult to quantify, but they can potentially have a large influence on the exact launch angles. Compared to Engelen (2012) and its cited sources, a conservative estimate is made for both the elevation and azimuth by setting the standard deviation of the angles at 1 deg. These uncertainties in the angles at the time of launch are assumed to translate into uncertainties in the angles at burnout. The standard deviation of 1 deg is therefore applied to both the full and ballistic model versions.

For the rail length, its physical length was set by T-Minus at 9000 mm. In ASTOS, the rail length is defined vertically with respect to the ground. The mean value used in the Monte Carlo simulation is therefore $\sin(67\ deg) * 9000 \approx 8285$ mm. For the standard deviation, it is decided to account for the vehicle's engagement length rather than an uncertainty in the rail's physical length. The engagement length is the length over which the vehicle's motion is restricted by the rail. The DART XL is only connected to the rail by two launch lugs, attached to the booster casing. It is therefore highly likely that the effective engagement length of the rail is smaller than its physical length, causing the vehicle to move more freely before exiting the rail. As a first estimate, the maximum difference (3-σ) is set at the distance between the ground and the vehicle's CoM at lift-of. This represents the situation where the vehicle's engagement with the rail becomes negligible when its CoM has left the rail. The vertical distance from the ground to this point leads to a 1-σ standard deviation of 444 mm. The engagement length cannot exceed the physical rail length, so the distribution is chosen to be a half-Gaussian distribution. This way, the vehicle's engagement length must lie somewhere between the physical rail length and the point at which the vehicle CoM exits the tower.

Timing

The last parameters to consider are potential timing differences. For the DART XL, this concerns an advance or delay in the ignition time and separation time. The ignition time is defined here as the time between ignition and actual lift-off, whereas the separation time is defined as the time between motor burnout and stage separation. The mean ignition time is estimated from static test data, by comparing the time of motor ignition with the time at which the measured acceleration exceeds and remains above the sea level gravitational acceleration. From this, the mean ignition time is set at 0.25 s. The uncertainty based on the static test data was quite low. However, static test data represents a motor fired vertically, with its nozzle at the top. As a result, it is difficult to predict the uncertainty of the ignition time during an actual launch. Therefore, a uniform distribution is selected with a 3-σ uncertainty of 100%. The 1-σ uncertainty is thus 33%.

As stated in Section 2.2, the DART XL utilises aerodynamic stage separation. The time between motor burnout and stage separation is defined as the separation time. It is estimated from the nominal trajectory model, because no real-life separation data is available for either a DART or a DART XL launch. From the nominal trajectory model, the mean separation time is estimated to be 0.1 s. Again, it is difficult to predict the uncertainty of the separation time due to a lack of available data. Therefore, a uniform distribution is selected with a 3-σ uncertainty of 100%. The 1-σ uncertainty is thus 33%.

4.4.3. Overview of the Dispersion Parameters

For convenience, the tables below provide an overview of all Monte Carlo parameters and their values as previously presented. Table 4.2 provides the parameters for the full flight version and Table 4.3 provides the parameters for the ballistic flight version of the nominal trajectory model. In these tables, parameter 1-σ standard deviations are either expressed as an absolute value in the same unit as the mean, or as a percentage of the mean. Furthermore, all parameters have a Gaussian distribution except for (1) the rail length which uses a half-Gaussian distribution, as the rail engagement length cannot exceed the maximum physical length, (2) ignition and separation times which use a uniform distribution due to the lack of available data to present an accurate estimate of the uncertainty and (3) the wind scaling factors which use a uniform distribution to represent random variation of the wind vectors from the mean monthly average wind profile, while still being largely centered around this mean.

Full Flight

The full flight model covers the full flight from launch to impact, with the initial state being stationary at the launch pad. A Monte Carlo analysis of this model provides insight into the uncertainty of the whole pre-flight nominal trajectory model, and thus the uncertainty of the nominal impact point. Furthermore, it can help determine whether the launch site selection is realistic by comparing the impact point dispersion and its distribution to the allowable impact area boundaries. Its dispersion parameters are provided in Table 4.2.

Table 4.2: Dispersion parameters for Monte Carlo analysis of the full trajectory from lift-off to impact.

Parameter	Symbol	Unit	Distribution	Mean μ	Std σ
Environment					
Atmospheric Density Scaling	$\Delta\rho$	-	Gaussian	1.0	5%
Wind Scaling (Northerly)	$V_{w,N}$	-	Uniform	1.0	16.7%
Wind Scaling (Easterly)	$V_{w,E}$	-	Uniform	1.0	16.7%
Motor					
Vacuum Thrust and Specific Impulse Scaling	ΔF	-	Gaussian	1.0	5%
Propellant Center of Mass (x)	$COM_{p,x}$	mm	Gaussian	1140	5 mm
Propellant Center of Mass (y)	$COM_{p,y}$	mm	Gaussian	0.0	1 mm
Initial Propellant Mass	$m_{p,i}$	kg	Gaussian	100.0	0.1 kg
Residual Propellant Mass	$m_{p,e}$	kg	Gaussian	0.0	1 kg
Mass and Inertia					
Booster Structural Mass	m_b	kg	Gaussian	32.0	1%
Booster Center of Mass (x)	$COM_{b,x}$	mm	Gaussian	931	20 mm
Booster Center of Mass (y)	$COM_{b,y}$	mm	Gaussian	0.0	1 mm
Dart Structural Mass	m_d	kg	Gaussian	14.0	1%
Dart Center of Mass (x)	$COM_{d,x}$	mm	Gaussian	796	6 mm
Dart Center of Mass (y)	$COM_{d,y}$	mm	Gaussian	0.0	1 mm
Aerodynamics					
Powered DART XL Drag Coefficient Scaling	$\Delta C_{D,pwd}$	-	Gaussian	1.0	10%
Unpowered DART XL Drag Coefficient Scaling	$\Delta C_{D,upwd}$	-	Gaussian	1.0	10%
Ballistic Dart Drag Coefficient Scaling	$\Delta C_{D,d}$	-	Gaussian	1.0	10%
Center of Pressure Scaling	ΔX_{CP}	-	Gaussian	1.0	10%
Launch					
Launch Elevation	γ_0	deg	Gaussian	67.0	1.0 deg
Launch Azimuth	χ_0	deg	Gaussian	324.1	1.0 deg
Rail Length	l	mm	Half-Gaussian	8285	444 mm
Timing Delays					
Ignition	t_{ig}	s	Uniform	0.25	33%
Separation	t_{sep}	s	Uniform	0.1	33%

Ballistic Flight
The ballistic flight model only considers the ballistic phase of the launch between motor burnout and impact. The model definitions are identical to the full flight model, except for the initial state vector which is taken to be the point of motor burnout from the full flight model to represent a real-time TRU state vector. No additional uncertainties are placed on the initial vehicle state to represent the assumption that the TRU state vectors are considered to be fully accurate. A Monte Carlo analysis of this model provides insight into the uncertainty of an impact point based on an in-flight state vector, to take into account when discussing the results of the in-flight IIP prediction model. Its dispersion parameters are provided in Table 4.3.

4.5. Impact Probability Area

By performing the Monte Carlo simulations, an impact point distribution is created based on all impact point latitudes and longitudes. In general, the impact point spread is expected to take on an elliptical shape that is largest in the downrange direction and smallest in the crossrange direction. The impact probability area can then be determined by calculating the boundary ellipse within which 99.7% (3-σ) of these Monte Carlo impact points lie. Given that the input parameters are mostly Gaussian distri-

Table 4.3: Dispersion parameters for Monte Carlo analysis of the ballistic trajectory from motor burnout to impact.

Parameter	Symbol	Unit	Distribution	Mean μ	Std σ
Environment					
Atmospheric Density Scaling	$\Delta\rho$	-	Gaussian	1.0	5%
Wind Scaling (Northerly)	$V_{w,N}$	-	Uniform	1.0	16.7%
Wind Scaling (Easterly)	$V_{w,E}$	-	Uniform	1.0	16.7%
Motor					
Residual Propellant Mass	$m_{p,e}$	kg	Gaussian	0.0	1 kg
Mass and Inertia					
Booster Structural Mass	m_b	kg	Gaussian	32.0	1%
Booster Center of Mass (x)	$COM_{b,x}$	mm	Gaussian	931	20 mm
Booster Center of Mass (y)	$COM_{b,y}$	mm	Gaussian	0.0	1 mm
Dart Structural Mass	m_d	kg	Gaussian	14.0	1%
Dart Center of Mass (x)	$COM_{d,x}$	mm	Gaussian	796	6 mm
Dart Center of Mass (y)	$COM_{d,y}$	mm	Gaussian	0.0	1 mm
Aerodynamics					
Unpowered DART XL Drag Coefficient Scaling	$\Delta C_{D,upwd}$	-	Gaussian	1.0	10%
Ballistic Dart Drag Coefficient Scaling	$\Delta C_{D,d}$	-	Gaussian	1.0	10%
Launch					
Initial Elevation	γ_0	deg	Gaussian	65.435	1.0 deg
Initial Azimuth	χ_0	deg	Gaussian	324.017	1.0 deg
Timing Delays					
Separation	t_{sep}	s	Uniform	0.1	33%

butions, it is expected that the latitude and longitude will also have a Gaussian distribution. The 3-σ ellipse boundaries can therefore be determined following the method presented in Spruyt (2014). Using this method, the mean latitude and longitude coordinates are set as the center of the ellipse. The magnitude of the semi-major and semi-minor axes is determined from the standard equation for an ellipse, Equation 4.6, which is rewritten into Equation 4.7. The axes lengths can then be calculated using Equation 4.8.

$$\left(\frac{x}{a}\right)^2 + \left(\frac{y}{b}\right)^2 = 1 \tag{4.6}$$

$$\left(\frac{x}{\sigma_x}\right)^2 + \left(\frac{y}{\sigma_y}\right)^2 = p \tag{4.7}$$

$$a = \sqrt{p}\sigma_x \,, \quad b = \sqrt{p}\sigma_y \tag{4.8}$$

Here, a is the semi-major axis, b the semi-minor axis and p is the scale of the ellipse for a confidence of 99.7%. This scale is taken from chi-squared distribution data, where the value for two degrees of freedom (latitude and longitude) is $p = 11.618$. The standard deviations σ_x and σ_y are determined as the square root of the largest and smallest eigenvalues of the data respectively. These eigenvalues represent the spread of the data in a given direction, where this direction is represented by the eigenvectors. Finally, the rotation of the ellipse axis with respect to true North and East is determined from the eigenvectors. Both the eigenvalues and eigenvectors are determined from the covariance matrix of the impact point coordinate data.

This method is used to determine the 3-σ ellipse for both the full flight and the ballistic flight models. The full flight ellipse is used to determine whether the vehicle is expected to impact within allowable impact area for a certain launch site. The ballistic flight ellipse, which is expected to be significantly smaller than the full flight ellipse, is used in the remainder of this research as a probability area for the in-flight IIP predictions.

5

Results of the Pre-flight Nominal Trajectory Model

Before going into the in-flight IIP prediction model, the results of the pre-flight nominal trajectory model are presented. These results are presented in two parts. First, the results of the environment model selection are presented. Next, the results of the Monte Carlo analysis are presented, using a model in which the selected environment model has been implemented. Finally, the impact probability area created from the Monte Carlo results is presented. Verification and validation steps are discussed throughout the results, with a reference table to each aspect provided in Appendix C.

5.1. Environment Model Selection

The environment model selection is dependent on the selection of the individual aspects that it is comprised of. As previously mentioned, the aspects considered are an atmospheric model, a gravitational model, a rotational model, a shape model, and a local wind model. For each aspect, the impact points for each option are shown on a map plot. These figures are shown at the end of the section, after each aspect's selection is detailed. A 1 km accuracy radius is depicted around the most complex option as a white circle. A model aspect meets the accuracy requirements if its impact point lies within the circle. This circle is used as a guide to determine whether the accuracy requirement can be met using a less complex model if it lies within the circle, or whether the more complex model is needed to meet the accuracy requirement. At the end of this section, an overview table of the selected model aspects is provided.

Atmospheric Model Selection

The first aspect to be selected is the atmospheric model, as this selection can then be included in the baseline for the selection of the other aspects. The considered options are the exponential atmosphere model, the US62 model and the US76 model. Figure 5.1a shows the resulting individual impact points when implementing each of these atmosphere models for a nominal trajectory. Immediately, it can be seen that the exponential atmosphere model does not meet the 1 km accuracy requirement as its impact point lies far beyond the boundaries of the circle. The impact points of the remaining options, US62 and US76, lie extremely close to each other at a distance of 1.0 m. In terms of implementation in the in-flight IIP prediction model, their complexity is expected to be very similar. Therefore, the US76 model is selected since it is the more recent atmospheric model.

Shape Model Selection

The considered options for the shape model are a spherical Earth and an ellipsoidal Earth. Figure 5.1b shows the resulting individual impact points when implementing each of these shape models for a nominal trajectory. This figure shows that, at the current launch latitude, the difference between the impact points for a spherical Earth and an ellipsoidal Earth model is approximately 1.9 km. For the current launch coordinates, it is therefore decided to select the ellipsoidal model in order to reach the accuracy requirements.

Gravitational Model Selection

For a gravitational model, three options are considered. In order of increasing complexity, they are the point mass model, central gravity with the J_2 effect and spherical harmonics up to degree and order 50. Figure 5.1c shows the resulting individual impact points when implementing each of these gravitational models for a nominal trajectory. It can be observed that the impact points for the zonal harmonics and spherical harmonics models lie very close to each other, at a distance of 14.6 m. Considering the large difference in complexity between the two gravitational models, the spherical harmonics model is removed from consideration as the J_2 model can reach a very similar degree of accuracy. At a distance of approximately 540 m, the point mass model impact point is further removed but still inside the circle. This means that the point mass model would be considered accurate enough to meet the accuracy requirement. However, one thing to consider is the fact that an ellipsoidal shape model is selected. For consistency, selecting the J_2 model is more logical because the J_2 effect describes the gravitational effects of the mass distribution for an ellipsoidal Earth. Selecting the J_2 model instead of the point mass model is not expected to add much complexity to the in-flight IIP prediction model, as one builds on the other. Therefore, the J_2 model is selected.

Rotational Model Selection

The considered options for the rotational model are a non-rotating Earth and a rotating Earth at a constant rate of 7.29212 $\cdot 10^{-5}$ rad/s. Figure 5.1d shows the resulting individual impact points when implementing no rotation or a constant rotation for a nominal trajectory. This figure shows that, at the current launch latitude and azimuth, the difference between the impact points for a non-rotating and rotating Earth is quite large at a distance of approximately 6.2 km. Therefore, it is decided to select the rotating Earth model.

Wind Model Selection

The considered options for the wind model are to assume no wind or to include a local monthly average wind profile. Figure 5.1e shows the resulting individual impact points when implementing no wind or an average wind profile for a nominal trajectory. This figure shows that, for the average local wind conditions at the current launch site, the difference between the impact points with and without wind is less than 1 km. At a distance of approximately 386 m, both options would meet the accuracy requirements. However, in the case of wind, there is still a high variability left depending on the time of year, the location and whether the input profile is averaged or includes extremes. Furthermore, T-Minus has expressed the desire to have the option to implement local wind measurements taken during a launch campaign. For these reasons, it is therefore decided to select the monthly average wind model. In the absence of adequate wind data, the option always remains to implement a zero magnitude wind profile instead of an averaged profile.

Overview

Table 5.1 below provides a summary of the environment selection, with all available options and those that were selected for the final environment model.

Table 5.1: Overview of the selected environment model aspects.

Environment Model Aspect	All Options			Selection
Atmospheric Model	Exponential	US62	US76	US76
Gravitational Model	Point mass	J_2 Coefficient	Spherical Harmonics	J_2 Coefficient
Rotational Model	Non-rotating	Constant Rate		Constant Rate
Shape Model	Spherical	Ellipsoidal		Ellipsoidal
Wind Model	No Wind	Monthly Average		Monthly Average

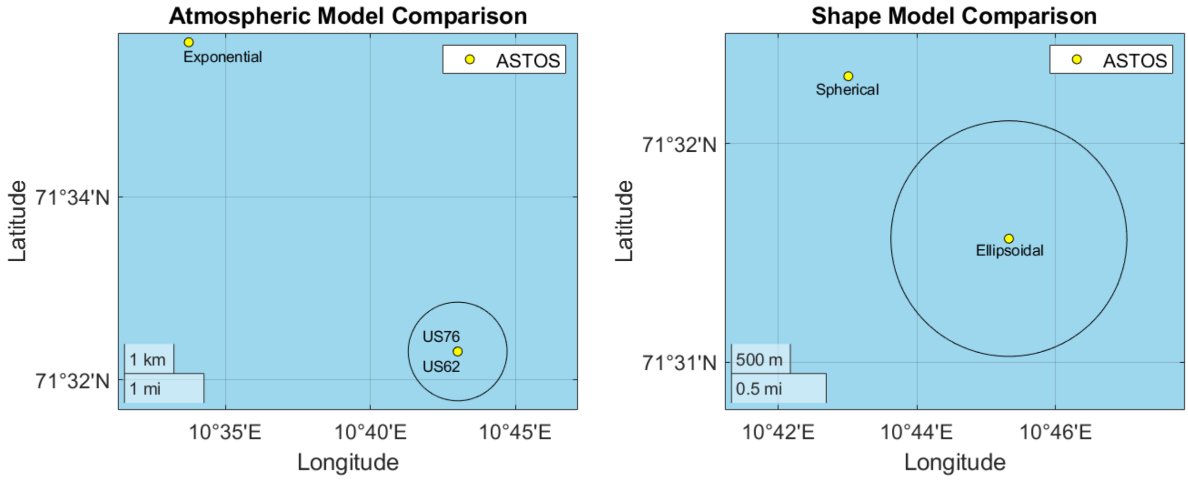

(a) Atmospheric model comparison using a baseline trajectory model, with respect to the required 1 km accuracy radius. The selected model is US76.

(b) Shape model comparison using a baseline trajectory model, with respect to the required 1 km accuracy radius. The selected model is ellipsoidal.

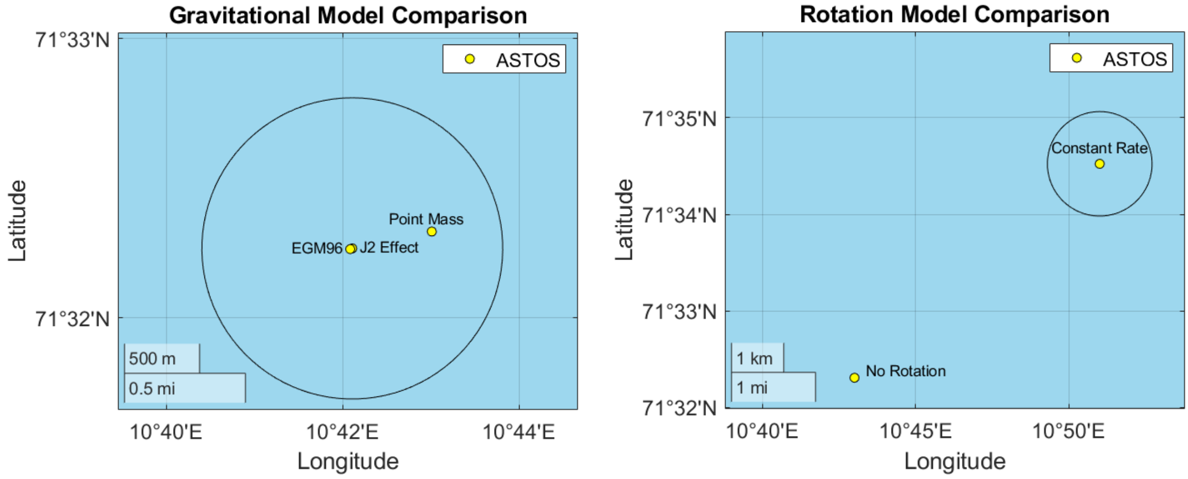

(c) Gravitational model comparison using a baseline trajectory model, with respect to the required 1 km accuracy radius. The selected model is to include the J_2 effect.

(d) Rotational model comparison using a baseline trajectory model, with respect to the required 1 km accuracy radius. The selected model is a constant rotation rate.

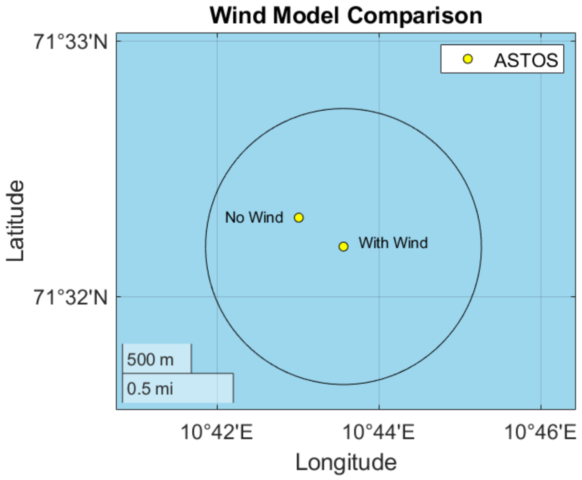

(e) Wind model comparison using a baseline trajectory model, with respect to the required 1 km accuracy radius. The selected model is the monthly average wind model.

Figure 5.1: Environment model comparisons upon which to base the selection of the individual aspects, with respect to the required 1 km accuracy radius.

5.2. The Nominal Trajectory

After selecting the environment model settings, these are implemented into the baseline model as well as into the expanded model versions used in the Monte Carlo analysis from launch to impact (full flight of the DART XL) and the from burnout to impact (ballistic flight of the DART XL's Dart payload stage). This section observes the trajectory similarities and differences between the baseline and expanded models. This is especially relevant since the simpler, baseline model is used as a reference for the in-flight IIP prediction model.

For the three trajectory model versions, Figure 5.2 shows the ground track of each. From this, the ground tracks seem to perfectly overlap each other. This shows confidence in the fact that the differences between the models is small. Furthermore, this appears to verify that the expanded model versions for the full flight and the ballistic flight produce a very similar trajectory. Table 5.2 shows the impact point coordinates for each model version, along with the computed distances between these points. The distance between the impact points of the full flight and ballistic flight expanded model versions was calculated to be 69 m. This similarity was expected because both versions use the same model definitions, and the ballistic flight model's initial state vector is taken from the full flight model.

Again for all three trajectory model versions, Figure 5.3 shows the horizontal distance versus altitude. Here, it can again be observed that the expanded model versions for the full flight and the ballistic flight produce the same trajectory, with only a difference in starting point. Furthermore, the baseline model seems to also largely overlap the expanded model versions. Only near the end of the trajectory, in the highlighted boxes in both figures, does the baseline model start to deviate more from the expanded model versions. The distance between the baseline and expanded model impact points was calculated to be 1.3 km, which would slightly exceed the required accuracy of 1 km or less. Considering that this only starts from about 15 km altitude, this is expected to be caused by a combination of more complex mass and inertia definitions as well as non-zero aerodynamic angles. All these factors would become more influential as the atmospheric density and vehicle velocity increases.

Overall, these figures show that all nominal trajectory model versions are very similar to each other, with the small exception of the baseline model deviation near the end of the trajectory. It is important to note that this should be taken into consideration when evaluating the results of the in-flight IIP prediction model and its expected accuracy.

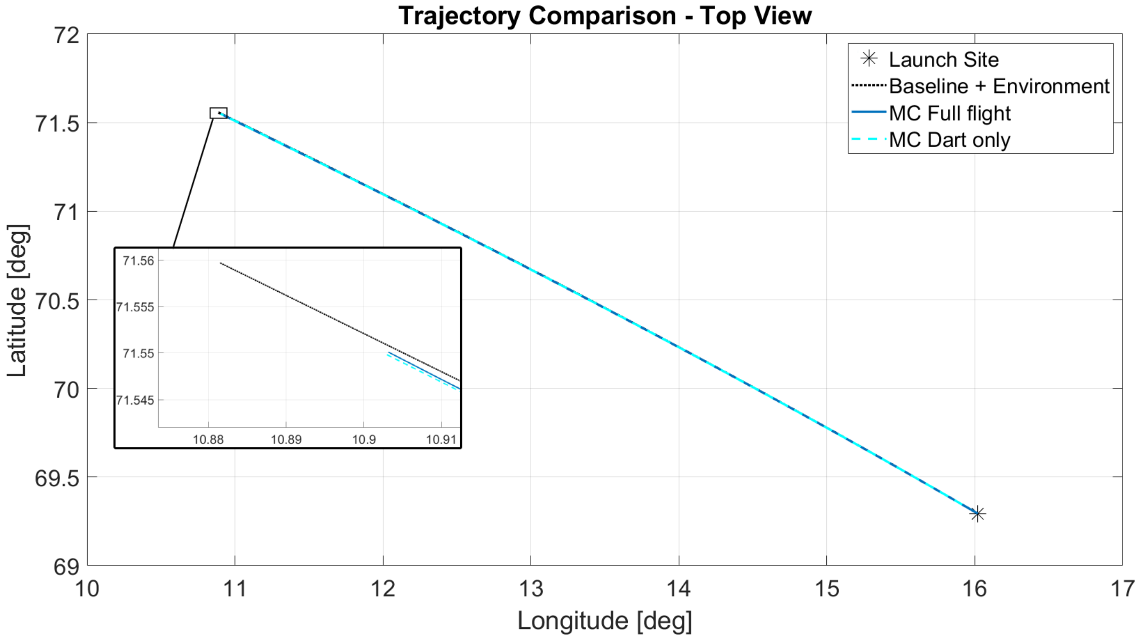

Figure 5.2: Latitude and longitude coordinate comparison for the expanded model versions and the baseline model with selected environment. The window shows a zoomed in view of the impact points of each model.

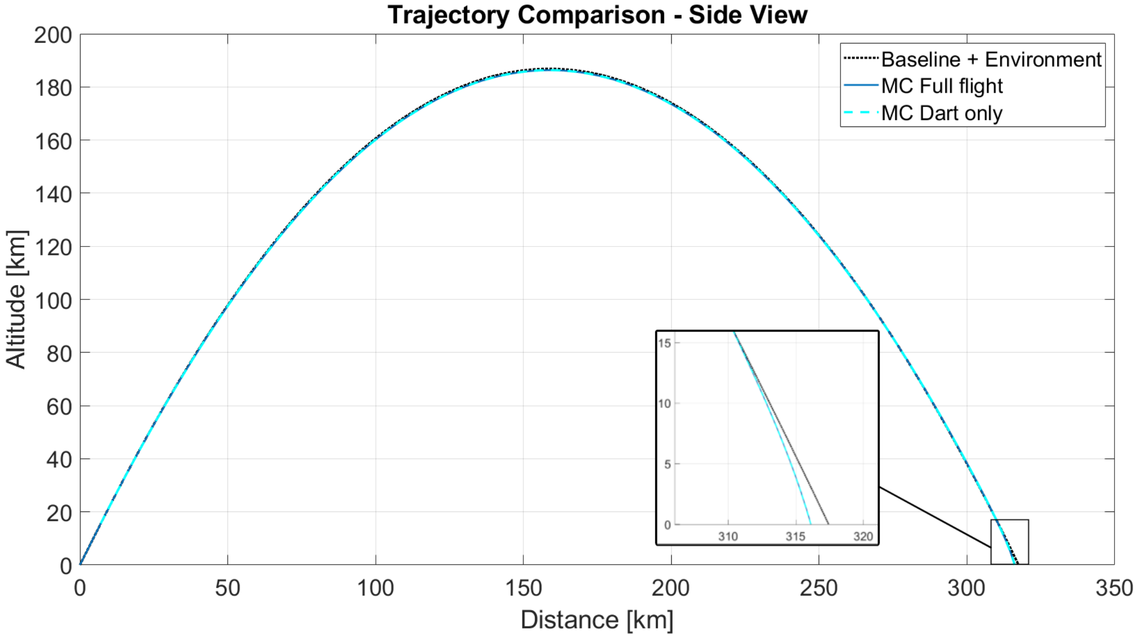

Figure 5.3: Horizontal distance and altitude comparison for the expanded model versions and the baseline model with selected environment. The window shows a zoomed in view of the impact points of each model.

Table 5.2: Impact point coordinates of the different nominal trajectory model versions and the ground distance between them.

Model Version	**IIP Latitude [deg]**	**IIP Longitude [deg]**	**Distance [m]**		
			B+E	**EBF**	**EFF**
Baseline + Environment (B+E)	71.559709	10.881459	-	1314	1318
Expanded Ballistic Flight (EBF)	71.550006	10.902555	1314	-	69
Expanded Full Flight (EFF)	71.550100	10.903171	1318	69	-

5.3. Monte Carlo Impact Point Distribution

This section presents the Monte Carlo analysis results for the expanded ballistic flight model version. All results consider the impact point distribution based on a nominal initial state vector at the start of the ballistic phase. It first presents the spread of the resulting IIP dispersion relative to the nominal impact point. Furthermore, a convergence analysis is done along with an evaluation of the impact point distribution. For similar results of the Monte Carlo analysis for the expanded full flight model version, see Appendix B.

Figure 5.4 shows the results of the Monte Carlo impact point dispersion, for 25000 individual runs representing uncertainties during the ballistic flight phase. Here, it can be observed that the spread is relatively concentrated. This indicates that the effect of varying the dispersion parameters is low. Furthermore, it can be seen that the spread is higher in the downrange direction than in the crossrange direction, and that the spread takes on the expected elliptical shape which is seemingly aligned with these directions. This is to be expected, as the effect of uncertainties is generally larger in the downrange direction than the crossrange direction. It was not investigated which parameters caused the largest spread, as acquiring data for individual parameters would require a lot of additional work that is not directly relevant to the model moving forward and is therefore out of the scope of this project.

The impact point data forms a bivariate normal distribution with latitude and longitude as the variables, which is visualised in Figure 5.5 along with a normal distribution fit of each. This figure shows that both the latitude and the longitude are indeed normally distributed, which is to be expected given that almost all the input dispersion parameters are normally distributed (Gaussian). The latitude fit does appear to show a very slight skew towards higher latitudes, which would indicate that there are slightly more scenarios resulting in an above average impact latitude.

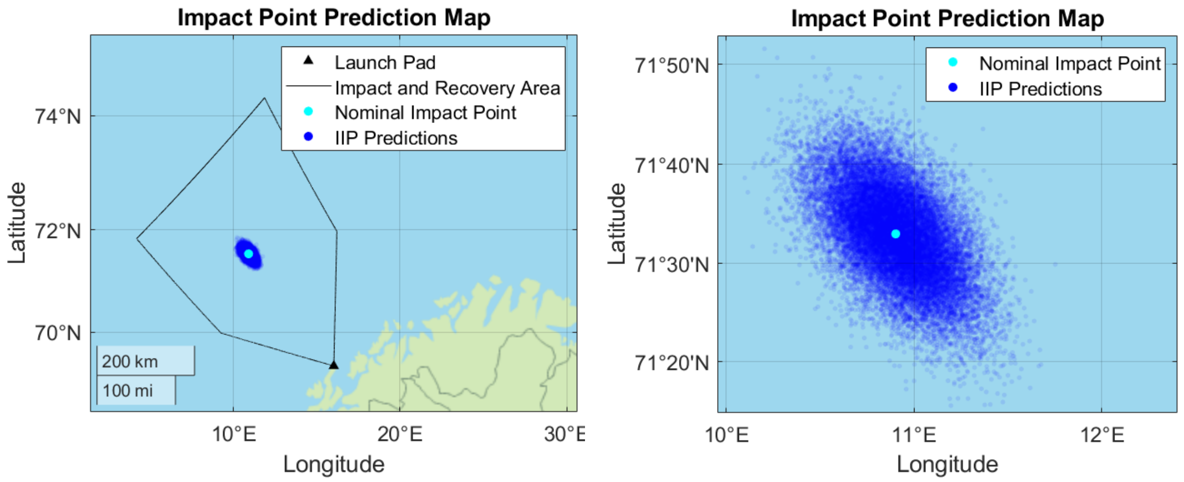

Figure 5.4: Impact point distribution relative to the Andøya allowable impact area, for a Monte Carlo simulation of 25000 runs during the ballistic flight phase. Zoomed in view on the right.

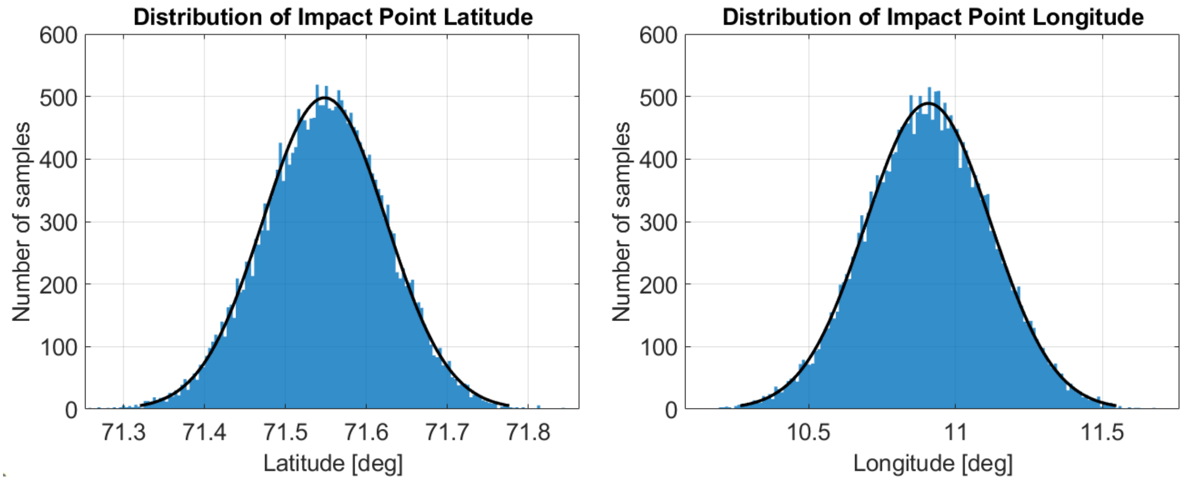

Figure 5.5: Histogram and normal distribution fit of the impact point latitudes and longitudes.

The final step in presenting the Monte Carlo impact point distribution is evaluating the convergence and confidence interval of the data. Figure 5.6 shows the convergence and 3-σ confidence interval for the latitude and longitude individually. The impact points presented above are indicated in this figure as '1st Batch', of which the moving average is visualised by the thick, solid black line. As observed, after a couple hundred runs this moving average converges towards the nominal latitude and longitude values, shown by the dashed black lines. The red lines represent the confidence interval boundaries, calculated from this first batch. This interval shows that, although convergence seems to occur after a few hundred samples, the confidence interval is still narrowing. When considering all 25000 samples, the narrowness of the confidence interval indicates certain convergence.

Taking this into account, the second batch was limited to 10000 runs as this was considered sufficient for convergence. The moving averages of this second batch are depicted by the thin, solid black lines indicated as '2nd Batch', which are not taken into account for the confidence interval. This second batch converges to the same values as the first run, therefore also converging to the nominal values. This also means that the second batch has a sufficient number of runs to fall within the established confidence interval. The results of the Monte Carlo simulations are therefore considered to be verified.

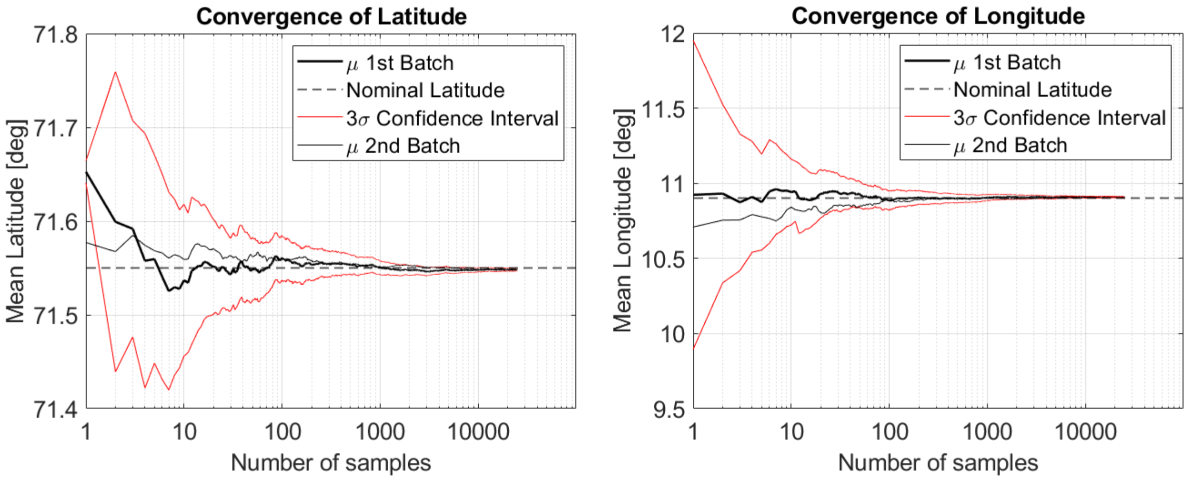

Figure 5.6: Convergence and confidence analysis of the impact point latitudes and longitudes.

5.4. Three-Sigma Impact Probability Area

Based on the IIP distribution presented above, the 3-σ impact probability area can be calculated. Additionally, a comparison is made between the previously determined nominal trajectory impact point and the mean impact point of this distribution. Lastly, this section provides a comparison between the impact probability areas for the ballistic flight model and the full flight model versions.

The 3-σ impact probability area for the ballistic flight model version is presented in Figure 5.7. The distance between the nominal and mean impact point is 0.238 km and the ellipse's semi-major and semi-minor axes lengths are 34.0 and 18.2 km respectively. Compared to the required accuracy limit of 1 km, these axes lengths are significantly larger. Therefore, for any real-time IIP prediction, this 3-σ impact probability area will have to be included in the visualisation for the RSO so they can take the uncertainty of the prediction into account. The first IIP prediction, using the initial state vector at burnout, will serve as the center of the ellipse in the visualisation. The ellipse then represents the expected uncertainty of this first prediction.

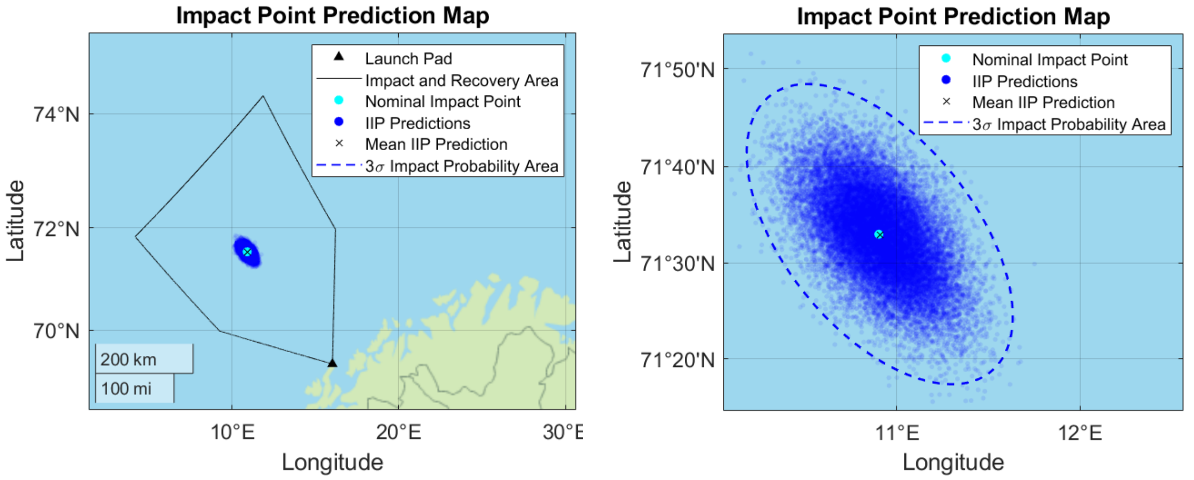

Figure 5.7: IIP distribution and subsequent impact probability ellipse relative to the Andøya allowable impact area, for a Monte Carlo of 25000 runs during the ballistic flight phase. Zoomed in view on the right.

For comparison, the 3-σ impact probability area for the full flight model version[1] is presented in Figure 5.8. Its semi-major and semi-minor axes lengths are 194.4 and 160.6 km respectively and the distance between the nominal and mean impact point is 3.396 km. These results clearly confirm that the IIP distribution and the subsequent impact probability area are much larger when considering the full flight from launch to impact. Furthermore, it can be observed that its eccentricity is lower than that of the ballistic impact probability area, indicating more uncertainty in the crossrange IIP distance. These results are also relevant when considering a launch with an off-nominal state vector at burnout, caused by uncertainties covered by the full flight Monte Carlo analysis. Under such circumstances, the resulting ballistic impact probability area will lie within this larger full flight impact probability area, with the corresponding off-nominal IIP prediction at its center.

Lastly, this figure shows that the impact probability area almost entirely lies within the allowable impact area, with the exception of only a handful of the 25000 impact points. Therefore, the Andøya launch range is considered to be suitable for launching a DART XL in terms when looking at the allowable impact area.

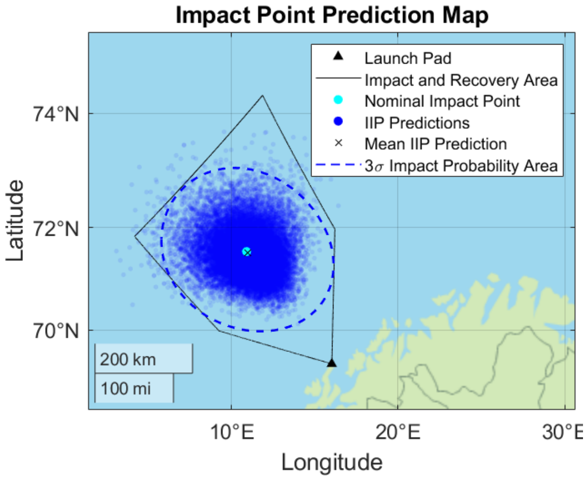

Figure 5.8: IIP distribution and subsequent impact probability ellipse relative to the Andøya allowable impact area, for a Monte Carlo of 25000 runs for the full flight from launch to impact.

---

[1] As previously mentioned, the full analysis of the Monte Carlo simulations for the expanded full flight model version is provided in Appendix B.

6

Methodology of the In-flight Instantaneous Impact Point Prediction Model

To predict a near real-time impact point during a launch, it is necessary to have a model that can not only meet the accuracy requirements but also the computation time requirements. The in-flight instantaneous impact point prediction model aims to build on the foundation of the pre-flight nominal trajectory model and its environment model selection to meet these requirements. It aims to do so by presenting a less complex model while still remaining within the desired accuracy, and by using the MATLAB software that is more suited for real-time applications than the previously used ASTOS software.

This change in software requires some additional flight dynamics and model definitions, which were previously defined on the back-end of the ASTOS software. This is achieved by first describing various relevant reference frame definitions within which to define the flight dynamics, and the degrees of freedom needed to do so. Next, additional information on the selected environment model aspects is provided and their relevant equations. After defining the settings in which the vehicle's motion takes place, the additional flight dynamics and equations of motion are provided that are needed to describe the vehicle's motion itself. To conclude the process, this chapter describes how the resulting model outputs are presented to be easily interpreted and monitored by a range safety officer during launch.

6.1. Reference Frames

A very important factor in defining a model is to decide which reference frame to define it in. This section describes the various reference frames used in the in-flight IIP prediction model, along with the method used for transformation between frames.

6.1.1. Frame Definitions

Generally, there are two different types of reference frames: inertial and non-inertial. An inertial reference frame is defined by the fact that Newton's laws are valid in these frames. For non-inertial reference frames, additional fictitious forces like the Coriolis force are needed alongside Newton's laws. This section describes the relevant reference frames from both categories.

Earth-Centered Inertial Frame (ECI)

In an Earth-Centered Inertial (ECI) frame, the origin is placed at the Earth's center of mass (CoM) and the axes have a fixed orientation, independent of the Earth's rotation[1]. The most commonly used version of the ECI frame, as shown in Figure 6.1, uses the J2000 coordinates. This indicates the mean equator and equinox at 12h, January 1st 2000. In this frame, the z-axis is directed upward along Earth's rotational axis. The x and y-axes lie in the equatorial plane, with the x-axis directed towards the point of vernal equinox where the equatorial and the ecliptic planes intersect and the y-axis completing the right-handed system (Mooij, 2017; Mulder et al., 2013).

---

[1] As noted in Mooij (2017), the ECI frame is actually pseudo-inertial. It does not take into account the fact that the Earth itself, and thereby the frame's origin, orbits the Sun.

Earth-Centered Earth-Fixed Frame (ECEF)

The Earth-Centered Earth-Fixed (ECEF) frame is a non-inertial frame, where the x and y-axes rotate about the z-axis with the same angular velocity as Earth. Again, the origin of the frame is placed at the Earth's CoM. The z-axis is directed upward along the rotational axis, similar to in the ECI frame. The x and y-axes lie in the equatorial plane, with the x-axis directed at the Greenwich meridian and the y-axis completing the right-handed system. Figure 6.2 provides a visualization of this frame. Here, it can be noted that the ECI and ECEF frames coincide once per Earth-rotation (Mulder et al., 2013).

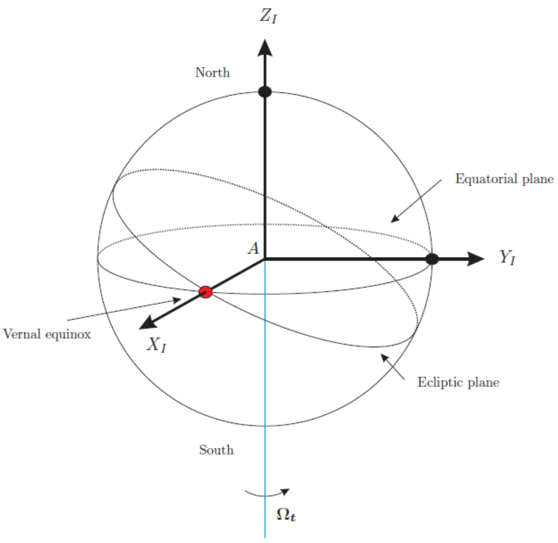

Figure 6.1: The Earth-Centered Inertial reference frame. [Source: Figure 2-2 from Mulder et al., 2013]

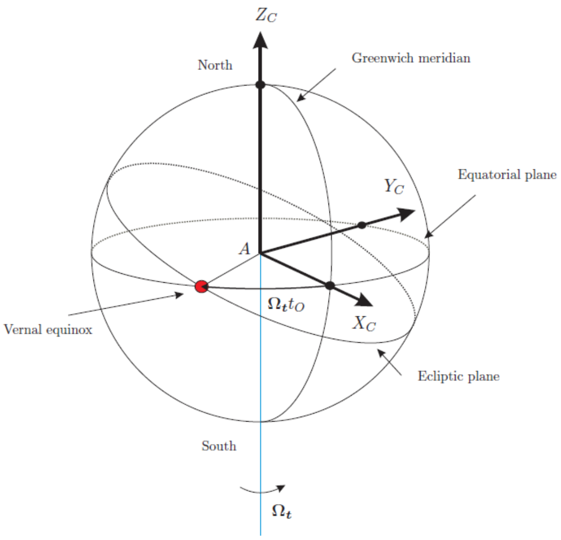

Figure 6.2: The Earth-Centered Earth-Fixed reference frame. [Source: Figure 2-3 from Mulder et al., 2013]

Body-fixed Frame

The body-fixed frame is a non-inertial frame, with its origin at the vehicle's CoM (Mulder et al., 2013). Commonly, the x,y and z-axes are chosen to coincide with the roll, pitch and yaw axes respectively. The x-axis is chosen in line with the vehicle's symmetry plane, through the nose. The remaining axes can be chosen rather arbitrarily for a rotationally symmetric vehicle like the DART XL. The most straightforward option here is to direct the z-axis along one of the fins and to have the y-axis complete the right-handed system. Figure 6.3 provides an example of the body-fixed frame for the REXUS sounding rocket. The body-fixed frame is especially useful because on-board sensors are body-fixed and therefore measure data relative to this frame (Jayaraman et al., 1982). This is also the case for the TRU, as described previously in Section 3.4, which interprets sensor data measured in the DART XL's body frame and converts it to a local reference frame.

Trajectory Reconstruction Unit Frame (TRU)

The Trajectory Reconstruction Unit frame, also referred to as the launcher reference frame, is a non-inertial frame with the origin at the launch location. For security reasons, the axes are aligned with the downrange direction for that specific launch so that third parties can only interpret the data sent by the TRU if they also know the launch location and azimuth. In this frame, the x-axis is aligned with the positive downrange direction and the z-axis points in the local 'up' direction. The y-axis completes the right-handed system, pointing in the crossrange direction (Olthof, 2020). This frame can therefore be considered as a rotated version of a local East-North-Up frame at the same point of origin.

East-North-Up Frame (ENU)

The East-North-Up frame is a non-inertial frame with the origin at an arbitrary point, often the local observer or the vehicle's CoM. For the DART XL trajectory, the ENU frame's origin is selected to be at the launch location. As mentioned previously, this makes it an identical yet rotated version of the TRU frame. In the ENU frame, the x-axis is aligned due East, the y-axis is aligned toward true North and the z-axis points in the local 'up' direction, see Figure 6.4.

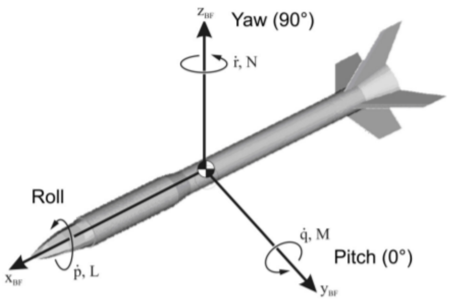

Figure 6.3: The body-fixed frame for the REXUS vehicle.
[Source: Figure 3-3 from Persson et al., 2007]

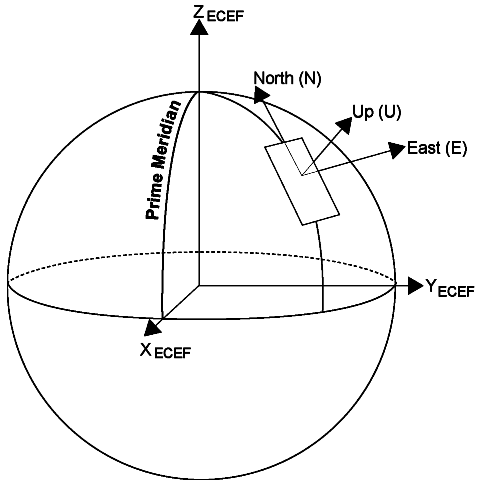

Figure 6.4: The East-North-Up reference frame.
[Source: NovAtel, 2017[2]]

6.1.2. Frame Transformations

If a vector is described in a certain frame, a transformation matrix is needed to be able to describe this vector in a different frame. This can be split into a translational and a rotational change, represented by the general equation of

$$\begin{aligned} v_B &= T + C_{B,A} v_A \\ T &= O_A O_B \end{aligned} \tag{6.1}$$

which represents a frame transformation of vector v from frame 'A' to frame 'B'. T is the translation vector, O_A and O_B are each frame's origin and $C_{B,A}$ is the rotational transformation matrix. As shown, the translation vector is based on the position of the origin of each frame, whereas determining the rotation is a more complex task. Appendix D provides some of the rotation matrices between the above-mentioned frames. More information on a general approach for frame transformations can be found in Section 2-2 of Mulder et al. (2013) and Section 3-2-3 of Mooij (2017).

6.2. Degrees of Freedom

To better describe a vehicle's motion, degrees of freedom (DoF) are introduced. These represent the number of independent motions that a vehicle can perform. A distinction is made between translational motion, describing the motion *of* the center of mass, and rotational motion, describing the rotation *about* the center of mass. Typically, a trajectory model consists of either three or six degrees of freedom, see Figure 6.5. A 3-DoF model can be made using only the three translational motions by approximating the vehicle as a point mass. For trajectory models, however, there is a more commonly used 3-DoF definition. Effectively, this describes a 2D, in-plane trajectory where the parameters to vary are horizontal distance, vertical distance and an in-plane rotation (Mooij, 2017). The rotation can be represented by for instance the pitch angle between the local horizontal and the nose of the vehicle, or by the flight path angle γ between the local horizontal and the velocity vector.

However, when using a 3-DoF trajectory model, a problem arises when crosswinds are introduced. In this case, additional degrees of freedom are required to describe out-of-plane motion. A logical transition would be to shift to a 6-DoF model. This would add degrees of freedom for cross-range translational motion, and yaw and roll rotational motion. However, with these added degrees of freedom also comes a great amount of added model complexity. It was therefore decided to create the initial IIP prediction model using three degrees of freedom. If the accuracy requirements are not met with this

---

[2] NovAtel (2017). *Definition of Reference Frames Within SPAN*. URL: https://docs.novatel.com/OEM7/Content/SPAN_Operation/Definition_Reference_Frames.htm (visited on 27/04/2022)

3-DoF model, then more degrees of freedom will be explored. For more information on how crosswinds are included in this 3-DoF model, see Section 6.3.5.

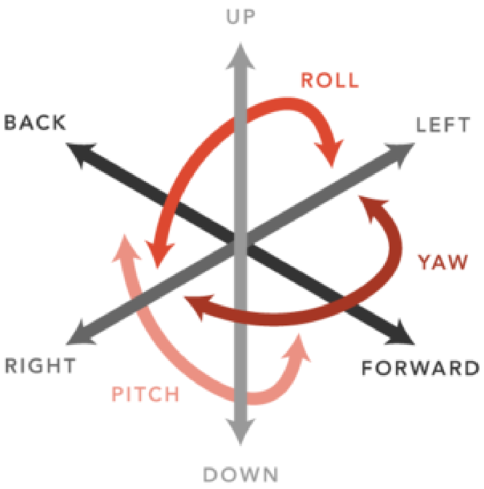

Figure 6.5: Visual representation of the translational and rotational degrees of freedom. [Source: Greene, 2019[3]]

6.3. Environment Model Implementation

In the previous chapter, a selection was made for different aspects of the environment model that are considered best suited for the IIP prediction model. This selection was made based on the accuracy requirement of 1 km or less and the computation time requirement of 1 s or less. This section elaborates further on the selected environment model aspects and how they are implemented in the near real-time IIP prediction model. Again, the environment model aspects that are considered are an atmospheric model, a gravitational model, a rotational model, a shape model, and a local wind model.

6.3.1. Atmosphere Model - United States Standard Atmosphere 1976

To define the Earth's atmosphere, the US Standard Atmosphere 1976 model was selected. This standard atmosphere model does not account for local variations and is therefore independent of the launch latitude and longitude. However, one important factor to note is that the US76 model uses the geopotential altitude z as a variable instead of geometric altitude h. The geopotential altitude is determined by adjusting the geometric altitude to include gravitational variations by latitude and altitude. The relation between the two is given by

$$\begin{gathered} g_0 dz = g\, dh \\ z = \int_0^h \frac{g}{g_0} dh \approx \frac{R_e h}{R_e + h} \end{gathered} \tag{6.2}$$

where R_e is the radius of the Earth (Mooij, 2017). With this definition of the geopotential altitude in mind, the equations for the other parameters can be determined based on the temperature distribution, the ideal gas equation (Equation 4.1) and the hydrostatic equation (Equation 4.2). Figure 6.6 shows the temperature distribution of the US76 model, and the altitudes between which different layers are distinguished. Two types of altitude layers can be observed: isothermal layers (vertical lines of constant temperature) and gradient layers (linear increase or decrease of temperature). Sea level conditions are represented by the gravitational acceleration $g_0 = 9.80665$ m/s^2, temperature $T_0 = 288.15$ K and density $\rho_0 = 1.225$ kg/m^3.

---

[3] J. Greene (2019). *The levels of immersion with VR - Sensory Technologies*. URL: https://sensorytechnologies.com/2019/04/30/3dof-vs-6dof/ (visited on 16/12/2020)

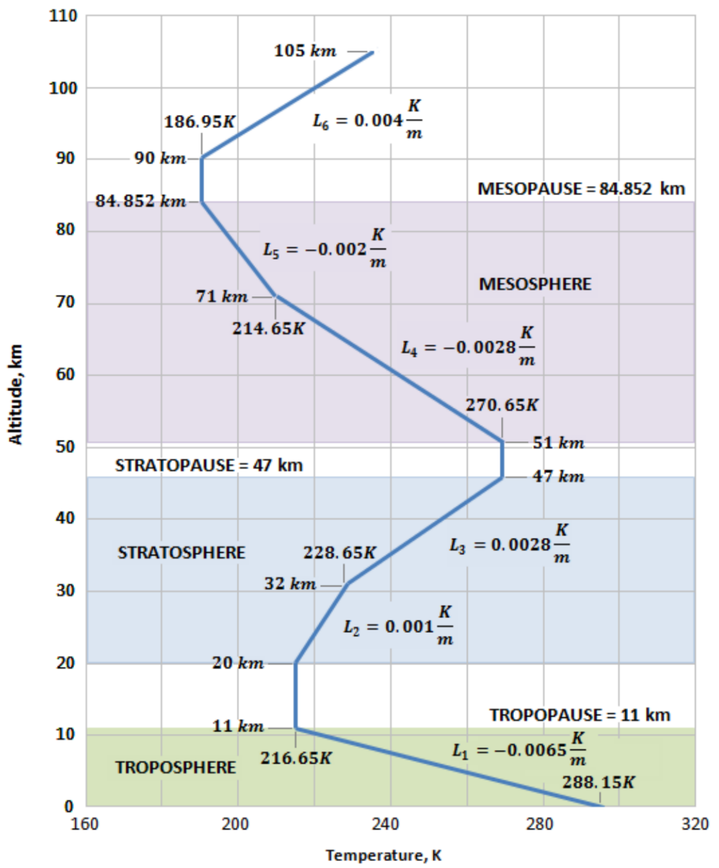

Figure 6.6: Temperature versus altitude profile according to the United States Standard Atmosphere 1976, with lapse rate L_i. [Source: De Marco, 2020[4]]

The isothermal layers are determined following the derivations in Anderson (2012), resulting in the following equations

Isothermal layers (lapse rate = 0):

$$T = T_1 = constant \tag{6.3}$$

$$\frac{p}{p_1} = e^{g_0/(RT)(z-z_1)} \tag{6.4}$$

where T_1, p_1 and z_1 represent the values at the lowest altitude, or base, of the isothermal layer. The density is then determined using the ideal gas equation.

Again following the derivations in Anderson (2012) leads to the following equations defining the gradient layers.

Gradient layers (lapse rate ≠ 0):

$$T = T_1 + L(z - z_1) \tag{6.5}$$

$$\frac{p}{p_1} = \left(\frac{T}{T_1}\right)^{-g_0/(LR)} \tag{6.6}$$

where

$$L = \frac{dT}{dz} \tag{6.7}$$

---

[4] A. De Marco (2020). *International Standard Atmosphere (ISA)*. URL: https://agodemar.github.io/FlightMechanics4Pilots/mypages/international-standard-atmosphere/ (visited on 15/12/2021)

Here, L is called the lapse-rate, or slope, of the gradient layer in K/m. This is a constant, specified value for each gradient layer. The value for each layer is given in Figure 6.6.

The models extend to higher altitudes, up to 700 km for the US62 model and even up to 1000 km for the US76 model, but the assumption of hydrostatic equilibrium starts to already break down above approximately 86 km (NOAA, 1962; NOAA, 1976). Above 86 km, the atmosphere is expected to no longer have a significant influence on the flight of the DART XL. Therefore, for simplicity, the equations that represent the US62 or US76 atmosphere models above this altitude are not considered.

6.3.2. Gravitational Model - J_2 effect

To define Earth's gravitational field, it was decided to use a point mass, central gravity approximation with the added influence of the zonal harmonics J_2 coefficient. The gravitational acceleration for a point mass approximation was already provided in Equation 4.3, which was dependent only on the radial vector between the center of Earth and the vehicle. With the addition of the J_2 effect, the new gravitational acceleration is presented in the following equations. Equation 6.8 provides the gravitational acceleration in the radial direction (pointing away from Earth's center), and Equation 6.9 provides the gravitational acceleration in the latitudinal direction (North to South). Here, and in the remainder of the work, the denormalized J_2 coefficient is used with a value of J_2 = -0.00108263.

$$g_r = \frac{\mu_E}{r^2}\left(1 + \frac{3}{2}\,J_2\,\frac{R_e^2}{r^2}\left(3\sin^2\lambda\, - 1\right)\right) \tag{6.8}$$

$$g_\lambda = -3\frac{\mu_E}{r^2}\,J_2\,\frac{R_e^2}{r^2}\sin\lambda\cos\lambda \tag{6.9}$$

How these new gravitational accelerations are implemented into the model, is explained further in Section 6.4.1 regarding the equations of motion.

6.3.3. Rotational Model - Rotating Earth

Due to its large influence on the predicted impact point, the rotating Earth model was selected to be implemented. As previously mentioned, a rotating Earth model considers both the motion of the surface itself as well as the co-rotation of the atmosphere. As shown in Equation 6.10, this is represented by the Coriolis force and relative forces respectively (Mooij, 2017). This also shows that these additional forces represent the difference between an ECI frame (index I) and an ECEF frame (index R).

$$\mathbf{F_R} = \mathbf{F_I} + \mathbf{F_{cor}} + \mathbf{F_{rel}} = m\frac{d^2\mathbf{r_{cm}}}{dt^2} + 2m\omega_\mathbf{R} \times \frac{d\mathbf{r_{cm}}}{dt} + m\omega_\mathbf{R} \times (\omega_\mathbf{R} \times \mathbf{r}_{\mathrm{cm}}) \tag{6.10}$$

How the effect of a rotating Earth is implemented into the model, is explained further in Section 6.4.1 regarding the equations of motion.

6.3.4. Shape Model - Ellipsoidal Earth

For a shape model, the selection was made to implement an ellipsoidal Earth instead of a spherical Earth. This is consistent with the selection of the J_2 effect for the gravitational model, as this model represents the gravitational effects of an oblate Earth. Three variables are required to represent an ellipsoidal Earth. Based on the IERS89 ellipsoidal model, the values used are the equatorial radius of $R_{e,eq}$ = 6378.136 km, the polar radius of $R_{e,pl}$ = 6356.751 km and the flattening factor, or ellipticity, of $f = 1 - R_{e,pl}/R_{e,eq} \approx$ 1/298.257.

This new definition of the Earth's shape also means that new altitude and latitude definitions have to be applied. Using an ellipsoidal model, the downward direction no longer points to the center of Earth, but rather it is perpendicular to the ellipsoidal surface and toward the equatorial plane. Therefore, three different angles can be defined: declination, geocentric latitude and geodetic latitude, as seen in Figure 6.7. These distinctions do not apply to the spherical model, as here all three latitude definitions are equal, as well as the accompanying altitude definitions. The longitude is independent of the latitude and shape model definitions.

The *declination* is the angle between the equatorial plane, and the radial vector directly connecting the center of the Earth with the vehicle. In this case, the altitude is defined as the distance between the vehicle, and the point where this radial vector intersects the surface. On the contrary, the *geodetic latitude* is the angle between the equatorial plane and the extension of the vector between the vehicle and the sub-latitude point, where the altitude vector intersects the Earth's surface perpendicularly. Subsequently, the altitude is defined as the distance between the vehicle and the sub-latitude point. Lastly, the *geocentric latitude of the sub-latitude point* is defined as the angle between the equatorial plane and the vector from the center of Earth to the sub-latitude point. Again, the altitude is defined as the distance between the vehicle and the sub-latitude point.

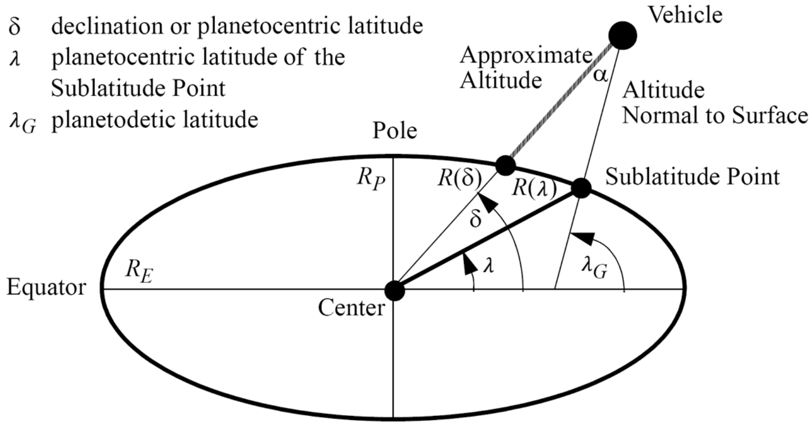

Figure 6.7: Visualization of an ellipsoidal Earth model and the different latitude definitions.
[Source: Figure 2.2 from Astos Solutions GmbH, 2020a]

For the ellipsoidal model, the local Earth radius varies between the polar and equatorial radii. For a given latitude λ, the local radius and subsequent geometric altitude h are given in Equations 6.11 and 6.12 (Mooij, 2017).

$$R_{e,s} = R_{e,eq}(1 - f \sin^2 \lambda) \tag{6.11}$$

$$h = r - R_{e,s}(\lambda) \tag{6.12}$$

Lastly, to convert from declination δ to geodetic latitude λ_G, an iterative process is started using the equations below, until the error $|\lambda_G - \lambda_i|$ is smaller than the desired threshold. The value of λ_G at that point is taken to be the geodetic latitude (Astos Solutions GmbH, 2020a).

$$\begin{aligned} \lambda_i &= \delta \\ N &= \frac{R_{e,eq}}{\sqrt{1-e^2 \sin^2 \lambda_i}} \\ \lambda_G &= \tan^{-1}\left[\tan\delta + \frac{Ne^2 \sin\lambda_i}{r\cos\delta}\right] \end{aligned} \tag{6.13}$$

where the eccentricity e is given by

$$e^2 = 2f - f^2 \tag{6.14}$$

6.3.5. Wind Model - Instantaneous Local Winds

The in-flight model implements the same input wind profile as previously presented in Section 4.2.5, based on the ERA5 database. This profile consists of Eastward and Northward wind magnitudes at altitudes up to approximately 40 km, which needs to be manually implemented into the in-flight model.

The wind velocity causes the vehicle to obtain an angle of attack, which can influence a vehicle's motion in two ways according to Wittenberg et al. (2016). For the DART XL, an unguided and statically stable vehicle, the second definition applies. This states that *"The rocket has the tendency to reduce the angle of attack, as a result of the static stability, and rotates with the nose into the wind."* (Section 2.5.3 from Wittenberg et al., 2016). In order to comply with the model assumption of a continuously zero angle of attack, the rocket is considered to have infinite static stability. This means that the vehicle's response to the wind velocity by rotating into the wind will happen instantaneously and its rotational inertia is neglected. In reality, the rotational inertia causes the weather cocking effect to be delayed, not instantaneous.

The magnitude and direction of the wind are dependent on the altitude. Their effects on the impact point can therefore not be calculated as a single displacement distance. Instead, the wind velocity is incorporated into the equations of motion in the change of vehicle velocity. This way, its effect is propagated at every time step of the integration, using the wind velocity at the accompanying altitude. Since the in-flight model is a 3-DoF model, this velocity cannot be included in for example normal force or lift coefficients without adding vehicle attitude degrees of freedom. The wind profile consists of geopotential altitude versus wind velocity, so this is converted to geometric altitude using Equation 6.2. The implementation into the equations of motion is described further in the following section.

The above-mentioned instantaneous influence and application of the wind velocity is expected to introduce a deviation from reality and from the presented nominal trajectory results in ASTOS. To compensate for this, a correction factor is introduced by which the Eastward and Northward wind velocities are multiplied at each time step of the integration. As an initial guess, it was decided to define the correction factor δ_w as the relative atmospheric density, with respect to sea level density ρ_0.

$$\delta_w = \frac{\rho}{\rho_0} \tag{6.15}$$

This correction factor accounts for the decreasing influence of wind velocities at higher altitudes, where the atmospheric density and thus the drag are lower. After evaluating the results of implementing this corrected wind model, the usability of the correction factor is determined. If necessary, it will be multiplied with an additional constant factor to more accurately replicate the effect of the wind as calculated in the pre-flight nominal trajectory model.

6.4. Flight Dynamics

The behaviour of the DART XL during a launch can be defined by the term 'flight dynamics'. Using flight dynamics, it is possible to not only describe but predict this behaviour, which is the main goal of the in-flight IIP prediction model. In this section, the set of equations of motion used to propagate the vehicle's trajectory is provided. Additionally, it describes the substitute input vehicle state vector that is used during the model development phase, as no actual TRU positioning data is available.

6.4.1. Equations of Motion

After describing the environment in which the vehicle is located, the relevant reference frames and desired number of degrees of freedom, next the motion of the vehicle within this framework can be described using equations of motion (EoM). Given that flight termination will only occur during the non-propelled flight phase, the EoM will only describe the Dart's ballistic trajectory over the Earth. A trajectory similar to that of the DART XL is visualized in Figure 6.8[5]. The selection of a 3-DoF model means that the aerodynamic angles of angle of attack, bank angle and sideslip angle are all assumed to be constant at a value of zero during this ballistic phase. As the result of a zero angle of attack, the lift force is also zero and the trajectory therefore describes a gravity turn (Wittenberg et al., 2016). This is all in line with the assumptions made for the baseline pre-flight nominal trajectory model, used for verification of the environment model implementation.

Next, the non-linear numerical equations of motion for ballistic flight are presented that are used to describe the trajectory of the DART XL Dart payload stage from burnout to impact. These equations of motion are obtained by following the method and assumptions for ballistic re-entry, as described in Section 12-2-2 of Mulder et al. (2013). The EoM presented in this source represent a model of many

---

[5] Note that burnout point 'B' in this figure does not best represent a DART XL flight. Burnout of the DART XL occurs within the atmosphere, so below the depicted Kármán line at 100 km altitude.

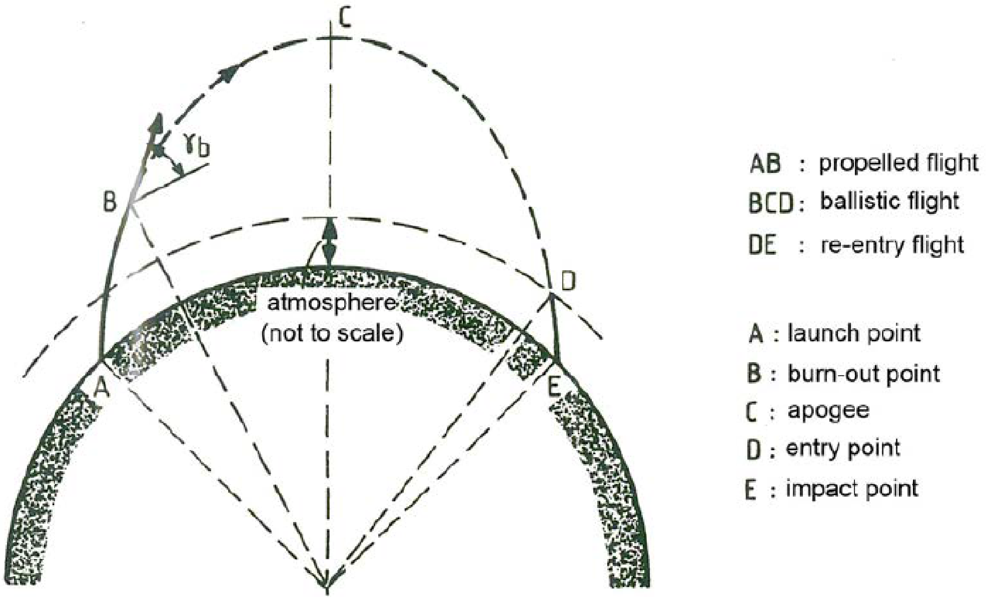

Figure 6.8: Regimes of a planar ballistic launch trajectory, assuming a spherical Earth.
[Source: Figure 4.1 from Wittenberg et al., 2016]

degrees of freedom. Here, a narrowed down version is presented to represent the desired 3-DoF model and the assumptions made. The external forces acting on the vehicle of weight and drag are treated as point forces for simplicity, evaluated in a body-centric frame with the origin at the vehicle's center of gravity. All angles are groundspeed-based.

Equations 6.16 to 6.18 show the dynamic 3-DoF translational motion, representing the change in velocity V, the change in flight path angle γ and the change in heading angle χ. In these equations, as presented by Mulder et al., 2013, terms representing the Earth's rotation were already included, but terms representing the J_2 effect are added (Mooij, priv. comm.). The $\boxed{\text{dashed}}$ boxes represent the J_2 terms in the equations and the $\boxed{\text{dotted}}$ boxes provide the terms representing Earth's rotation. Lastly, Equations 6.19 to 6.21 show the resulting kinematic position in terms of the change in distance r and the change in latitude and longitude λ and Λ.

$$\dot{V} = -\frac{D}{m_d} - g_r \sin\gamma \boxed{-g_\lambda \cos\gamma \cos\chi} \boxed{+\omega^2 r \cos\lambda \left(\sin\gamma \cos\lambda - \cos\gamma \sin\lambda \cos\chi\right)} \tag{6.16}$$

$$\dot{\gamma} = \left(\frac{V}{r} - \frac{g_r}{V}\right)\cos\gamma \boxed{+\frac{g_\lambda}{V}\sin\gamma\cos\chi} \boxed{+2\omega\cos\lambda\sin\chi + \frac{\omega^2 r}{V}\cos\lambda\left(\cos\gamma\cos\lambda + \sin\gamma\sin\lambda\cos\chi\right)} \tag{6.17}$$

$$\dot{\chi} = \frac{V}{r}\cos\gamma\tan\lambda\sin\chi \boxed{+\frac{g_\lambda}{V}\frac{\sin\chi}{\cos\gamma}} \boxed{+2\omega\frac{\cos\gamma\sin\lambda - \sin\gamma\cos\lambda\cos\chi}{\cos\gamma} + \frac{\omega^2 r}{V}\frac{\cos\lambda\sin\lambda\sin\chi}{\cos\gamma}} \tag{6.18}$$

$$\dot{r} = \dot{h} = V\sin\gamma \tag{6.19}$$

$$\dot{\Lambda} = \frac{V}{r}\frac{\sin\chi\cos\gamma}{\cos\lambda} \tag{6.20}$$

$$\dot{\lambda} = \frac{V}{r}\cos\gamma\cos\chi \tag{6.21}$$

The wind velocity is included by decomposing the change in velocity $\dot{V}$ for a given time step into components in the ENU frame. The wind velocity at the vehicle's current altitude, V_w, is then multiplied by the correction factor δ_w and the time step-size dt. It is then added to the vehicle's East and North velocity components, V_1. It is added, not subtracted, because $Groundspeed = Airspeed + Wind\ Speed$. The resulting updated velocity components V_2 are given in Equation 6.22 below. In this equation, the subscripts E, N, U represent the directions in the ENU frame, subscript w represents the wind velocity and subscripts 1 and 2 represent the vehicle velocity vectors before and after adding the wind velocity.

$$\begin{bmatrix} V_{E,2} \\ V_{N,2} \\ V_{U,2} \end{bmatrix} = \begin{bmatrix} \cos\gamma * \sin\chi \\ \cos\gamma * \cos\chi \\ \sin\gamma \end{bmatrix} \begin{bmatrix} V_{E,1} \\ V_{N,1} \\ V_{U,1} \end{bmatrix} + \begin{bmatrix} V_{E,w} \\ V_{N,w} \\ V_{U,w} \end{bmatrix} * \delta_w \; dt \tag{6.22}$$

With this new velocity vector, the new changes in velocity, flight path angle and heading angle are calculated using Equation 6.23. This way, both the downrange and cross-range components are included without adding additional degrees of freedom or aerodynamic angles.

$$\begin{aligned} \dot{V} &= \sqrt{V_{E,2}^2 + V_{N,2}^2 + V_{U,2}^2} \\ \dot{\gamma} &= atan2\left(V_{U,2},\ \sqrt{V_{E,2}^2 + V_{N,2}^2}\right) \\ \dot{\chi} &= atan2\left(V_{E,2},\ V_{N,2}\right) \end{aligned} \tag{6.23}$$

For each time step, this process is used to determine the change in vehicle state. As defined in Section 3.5, the state is then propagated to the next time step using Euler integration. This is repeated continuously, while the vehicle's altitude is larger than zero. To match the pre-flight nominal trajectory model definitions, the final vehicle state at which the altitude is larger than or equal to zero is taken as the final IIP prediction.

6.4.2. Input State Vector

During a launch, the input state vector for each time step comes from the latest TRU state vector calculations. The IIP prediction model is set up so that the TRU inputs, consisting of position and velocity components in the TRU frame, can directly be implemented in real-time as new data is received. This data is then converted from the TRU frame to the ENU frame, in order to determine the initial state vector for the parameters used in the equations of motion to propagate the trajectory.

However, when setting up the model, an issue arises in the fact that neither the DART XL nor the TRU have been flown before. It is therefore not possible for the IIP prediction model to use input state vectors based on actual flight data. For this reason, a temporary substitute input state vector is created during the model development and testing phase, based on data taken from the pre-flight nominal trajectory model in ASTOS. From the pre-flight model, the position and velocity parameters at the time of motor burnout are exported to create the initial state vector for the IIP prediction model.

The exported parameters from ASTOS are not defined in the TRU frame, so creating the final substitute input state vector requires some additional frame transformations and unit conversions. The exported vehicle velocity components are defined in the ENU frame, in km/s. These are converted to the TRU frame using the corresponding transformation matrix, as provided in Appendix D, which is defined by a rotation about the z-axis with the launch azimuth angle. This is visualised in Figure 6.9. The unit of the resulting velocity components is m/s.

Downrange and crossrange distances are not provided by the ASTOS software, only a total ground distance from the launch site. Therefore, the downrange and crossrange distances are determined from the projected latitude and longitude of the burnout point. The distances can then be determined by decomposing the vector to this projected point along the TRU frame axes and determining the individual lengths in m. As shown in Figure 6.9, the downrange distance is defined in the direction of launch. It is therefore highly unlikely for the downrange distance to ever have a negative value. The positive crossrange distance is defined in the direction of the TRU frame y-axis, which completes its right-handed system. Lastly, the geometric altitude as exported by ASTOS is converted from km to m, completing the position state vector components.

This results in the final substitute input state vector, consisting of position in m and velocity in m/s in the TRU reference frame. From this state vector, the IIP prediction model can then extrapolate the trajectory to the surface, as it would during a launch. This process can be repeated for subsequent time steps in the pre-flight model after motor burnout, to simulate receiving updated TRU state vectors throughout the ballistic flight phase.

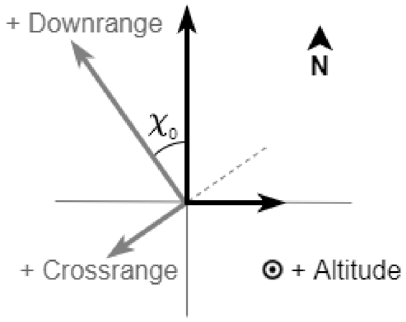

Figure 6.9: Representation of the positive directions of downrange distance, crossrange distance and altitude for the TRU frame (grey) and the ENU frame (black). Both frames are right-handed.

6.5. Output Compilation

As the final step after an impact point has been predicted, this IIP prediction needs to be communicated to the responsible RSO to advise their flight termination decisions. Making a flight termination decision is a very time-critical process. It is therefore crucial to present the IIP prediction in a way that can be unambiguously and quickly interpreted. In cooperation with T-Minus, three aspects were determined that should at minimum be displayed to the RSO (requirement FTS-TR-07). All three aspects are discussed here. Finally, the course of action for an end of signal from the TRU is considered.

6.5.1. Map Representation

The first aspect required to be presented to an RSO is '*a map representation of current and past impact point predictions, relative to the allowable impact area boundaries*'. In this case, the geobasemap function in MATLAB was used to produce a map plot[6]. This automatically includes a geographic background, distance scalebar and a latitude and longitude grid. If desired, additional factors such as the ground track of the most recent prediction can be visualised as well. Upon this map plot with reference elements, the launch location and the launch range allowable impact area boundaries are plotted as reference elements, along with the Monte Carlo 3-σ impact probability area boundaries. After each impact point prediction, the latest IIP prediction will be added to this figure. IIP predictions of previous time steps will remain visible, albeit in a different colour and opacity than the most recent prediction, so that trends can be observed.

A potential downside of this method is that producing geographic plots can increase the overall computation time. If this proves to be a problem, there is the option to remove the geographic background to speed up this visualisation. In this case, the distance scalebar, latitude and longitude grid and the reference elements would need to remain visible for interpretation purposes.

6.5.2. Numerical Value Output and Visual Indicator

The second required aspect is '*a numerical value output, representing the shortest ground distance between the location of a predicted impact point and the allowable impact area boundaries*'. As an accompaniment, the third aspect requires the presence of '*a visual indicator for the numerical value output, to differentiate between impact points inside and outside of the allowable impact area boundaries*'. Both of these will be printed in the MATLAB command window for each prediction.

The numerical value is determined by calculating the shortest ground distance between the impact point coordinates and the coordinates of the closest point on the allowable impact area boundaries. This is then printed in the command window in km with three decimals, effectively presenting the distance with an accuracy of m. If the IIP prediction lies inside the boundaries, the distance is presented as a positive value. If the IIP prediction lies outside of the boundaries, the distance is presented as a negative value. Furthermore, the word 'Inside' or '**OUTSIDE**' is printed alongside the distance for additional clarity.

---

[6] MathWorks (2018). *geobasemap - Documentation*. URL: https://nl.mathworks.com/help/matlab/ref/geobasemap.html (visited on 06/06/2022).

6.5.3. Loss of Signal Considerations

As a final consideration, it is discussed how to indicate an loss of signal from the TRU. This can have two general causes: a (potentially temporary) loss of telemetry with the TRU or a vehicle position beyond the line of sight. In either case, no new vehicle state vectors can be received at the ground station. During a launch, the IIP prediction model continuously polls the file containing the TRU state vector calculations for the latest state vector. Upon a loss of signal, this latest value does not change until the signal is restored. Therefore, the IIP model is set to detect when two consecutive state vector polls return the same vector. Upon detection of two equal state vectors, the IIP prediction process is paused for 1 second. This is indicated to the RSO by printing the following sentence: 'Waiting for new input data entries. IIP prediction is paused.'. After this second, the model will again poll to detect if a new input state vector is available. If not, the model will continue the loop of pausing and polling repeatedly. During this process, the preceding predictions will remain visible to the RSO. If a new state vector is indeed available, the model will resume its prediction process with this new input. Since the current version of the IIP prediction model does not take predictions from previous time-steps into account, waiting for any duration of time has no influence on the predictions after this pause. As a final consideration, this loss of signal check also becomes active in the unlikely case that the computation of the IIP prediction is faster than the update rate of the TRU.

7

Results of the In-flight Instantaneous Impact Point Prediction Model

In this chapter, the results of the in-flight IIP prediction model are presented. These results are divided into four parts. First, the results of the environment model implementation are presented, along with a comparison to the results of the pre-flight nominal trajectory model. Next, an evaluation is made of the model accuracy and the model computation time based on the nominal IIP prediction. Next, the execution of the output presentation is provided, in terms of both the visual and numerical outputs. Finally, this chapter provides a quick overview of the results when testing the IIP prediction model for a different launch site, for verification and validation purposes. Additional verification and validation steps are discussed throughout the results, with a reference table to each aspect provided in Appendix C.

7.1. Environment Model Implementation and Comparison

During the development of the IIP prediction model, the previously selected environment model aspects are implemented. This section presents the results of this implementation, relative to the corresponding results for the pre-flight nominal trajectory model. The selected environment model aspects were implemented according to the equations in Section 6.3. In this comparison, the nominal trajectory model results are used as validated control points because they were determined using an established trajectory simulation software. In this section, the wind model is discussed separately from the other environment model aspects because its implementation is less straightforward. Finally, this section presents the combined effects of implementing all selected environment model aspects and how this compares to the results of the nominal trajectory model.

7.1.1. General Environment Model Implementation and Comparison

For each aspect, the impact point comparison is shown on a map plot. A 1 km accuracy radius is depicted as a white circle around the control point of the selected aspect. Furthermore, the figures also show the impact points using the baseline environment model as described in Table 4.1. These are used to compare the difference in impact point before and after implementing an environment model aspect. Since this baseline point is the same impact point in all figures, it is indicated with '(B)' for reference. Figure 7.1 shows the results for each of the environment model aspects, except for wind. The results of the pre-flight nominal trajectory model are shown as yellow circles and the results of the in-flight IIP prediction model are shown as pink squares.

In Figure 7.1a, a slight deviation of 150 m is observed between the implementation results of the US76 atmosphere model. Upon analysis, the cause for this deviation has not been found. It is expected to be caused by inherent differences in the model design between ASTOS and MATLAB, rather than an inaccurate implementation of the atmosphere model. The trajectory models could not be tested without implementation of the atmosphere model, so this hypothesis could not be tested further. Therefore, the decision was made that this result is considered to verify the implementation of the atmospheric model in the IIP prediction model. The observed deviation is expected to remain present in the other aspect comparisons, since they all use the settings for this IIP prediction as a baseline.

In Figure 7.1b, it can be observed that the implementation of an ellipsoidal Earth model in the IIP prediction model yields very similar results to the nominal trajectory model. It does show that the observed deviation between the two models seems to decrease when implementing the ellipsoidal shape model. Again, it is unclear what causes this change as it is unclear what caused the deviation in the first place. For this reason, it was decided that this result is considered to verify the implementation of the shape model in the IIP prediction model.

In Figure 7.1c, it can be observed that the addition of the J_2 effect to the central gravity model in the IIP prediction model yields seemingly identical results to the nominal trajectory model. Therefore, this result is considered to verify the implementation of the gravitational model in the IIP prediction model.

In Figure 7.1d, it can be observed that the implementation of a constant Earth rotation rate in the IIP prediction model yields seemingly identical results to the nominal trajectory model. Therefore, this result is considered to verify the implementation of the rotational model in the IIP prediction model.

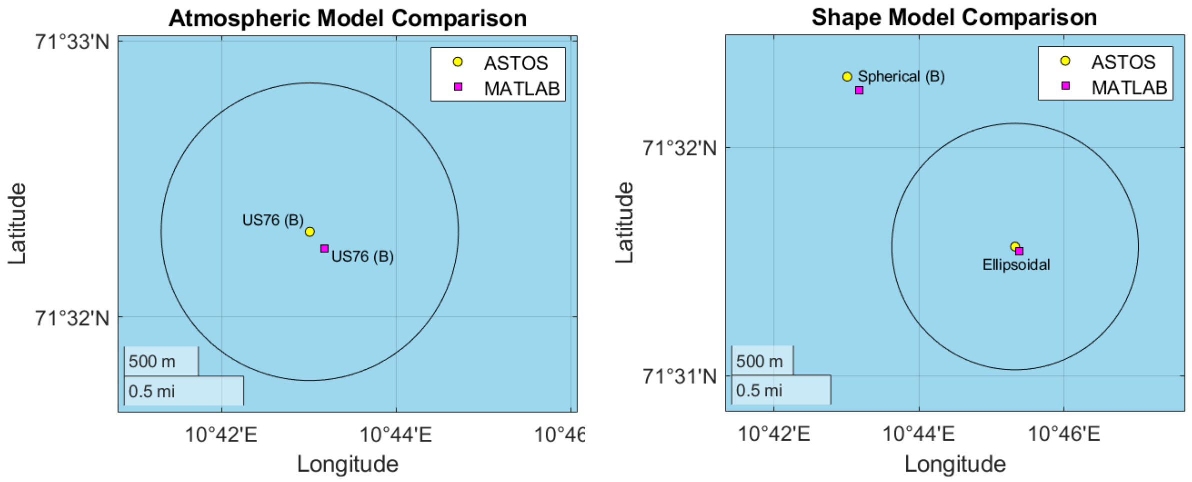

(a) Implementation of the US76 atmospheric model.

(b) Implementation of the ellipsoidal shape model.

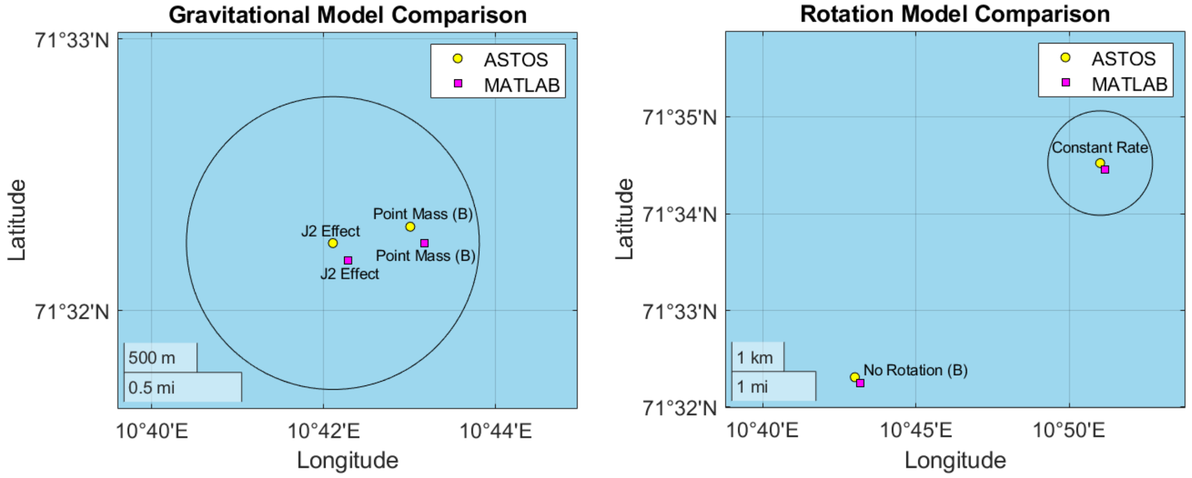

(c) Implementation of the gravitational model including the J_2 effect.

(d) Implementation of the constant rate rotational model.

Figure 7.1: Implementation of environment model aspects in the IIP prediction model, compared to its baseline IIP and the nominal trajectory model results. Results with respect to the required 1 km accuracy radius.

7.1.2. Local Wind Model Implementation and Scaling Factor

The implementation of the wind model is less straightforward than that of the other environment model aspects because it requires the addition of a correction factor to represent the fact that the vehicle's rotational inertia is neglected in the 3-DoF IIP prediction model. This correction factor is initially set to represent the relative atmospheric density with respect to sea level conditions. In this section, it is evaluated whether this correction factor allows the IIP prediction model to sufficiently replicate the effect of implementing the local wind profile from the ERA5 dataset. The effect of this local wind model was previously presented in Figure 5.1e, where the same local wind profile was implemented into the nominal trajectory model with its results considered verified.

The results for this initial correction factor are visualised in Figure 7.2a by the pink datapoint 'With Wind'. This clearly shows that the initial correction factor is insufficient to produce a wind model that approaches the nominal trajectory model results, represented by the yellow datapoints. It is not a surprise that there is a discrepancy between the effect of wind in the pre-flight and in-flight model, as the in-flight model considers the wind to have an instantaneous effect instead of accounting for the delayed effect caused by the vehicle's rotational inertia.

Updating the Wind Correction Factor

To better approach the verified and more realistic nominal trajectory model results, it was decided to multiply the wind correction factor δ_w by an additional scaling factor. This updated correction factor was determined iteratively by manually trying different scaling factors between 0 and 1, with intermediate steps of 0.1. This is visualised in Figure 7.2b by the hollow black datapoints. From the IIP predictions corresponding to these scaling factors, it was determined that the desired scaling factor should lie between 0 and 0.1. In a second iterative process, it was determined that the desired additional wind scaling factor is 0.06, leading to the updated correction factor presented in Equation 7.1. Implementing this updated wind correction factor produces the pink datapoint labelled by 'Corrected Wind' in Figures 7.2a and 7.2b.

$$\delta_w = 0.06 \, \frac{\rho}{\rho_0} \tag{7.1}$$

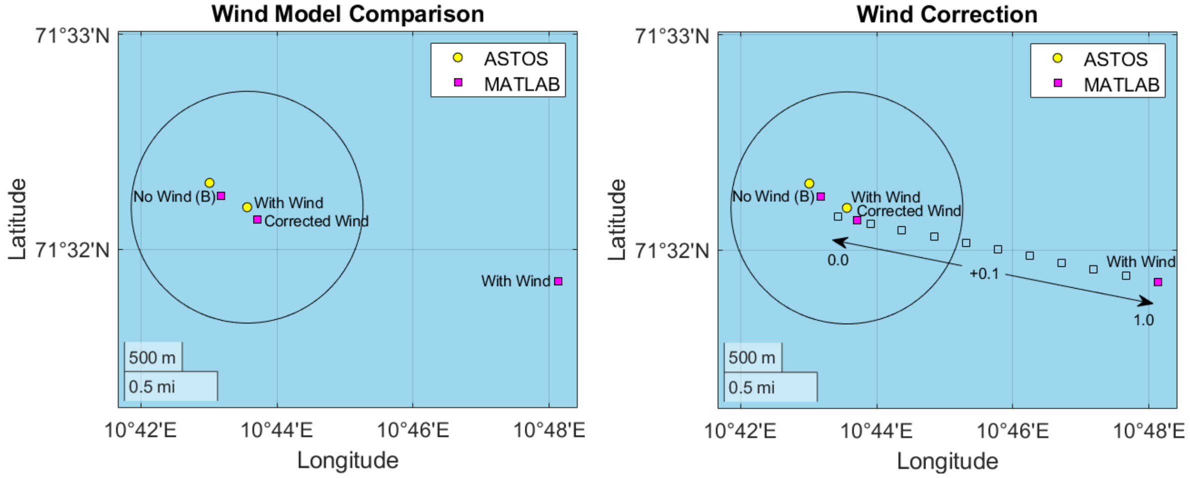

(a) Implementation of the updated correction factor in 'Corrected Wind', compared to the original correction factor in 'With Wind'.

(b) Determining the desired correction factor to match the results from the pre-flight nominal trajectory model.

Figure 7.2: Implementation of the updated wind scaling factor of 0.06 times the relative atmospheric density.

Verifying the Updated Wind Correction Factor

To ensure that this correction factor is not just valid for this specific wind profile, this updated correction factor was tested for a different wind profile as additional verification. For this purpose, a fictitious wind profile of constant magnitude was fabricated. This fabricated wind profile consists of winds at altitudes between 0 and 45 km, where the Easterly and Northerly wind components were set a constant arbitrary magnitude of +2 m/s.

The results for this fabricated wind profile are shown in Figure 7.3. It was tested in both the nominal trajectory model represented by the yellow datapoints as well as the IIP prediction model represented by the pink datapoints. The pink datapoints labelled 'Constant Wind' and 'Corrected Constant Wind' respectively represent the IIPs before and after updating the scaling factor δ_w. For this validation case, the selected scaling factor of 0.06 again appears to produce an IIP closest to the expected value from the nominal trajectory model IIP in yellow. Therefore, the updated wind correction factor presented in Equation 7.1 is verified to sufficiently replicate the effects of wind on an IIP prediction. It is thus implemented in all IIP predictions going forward.

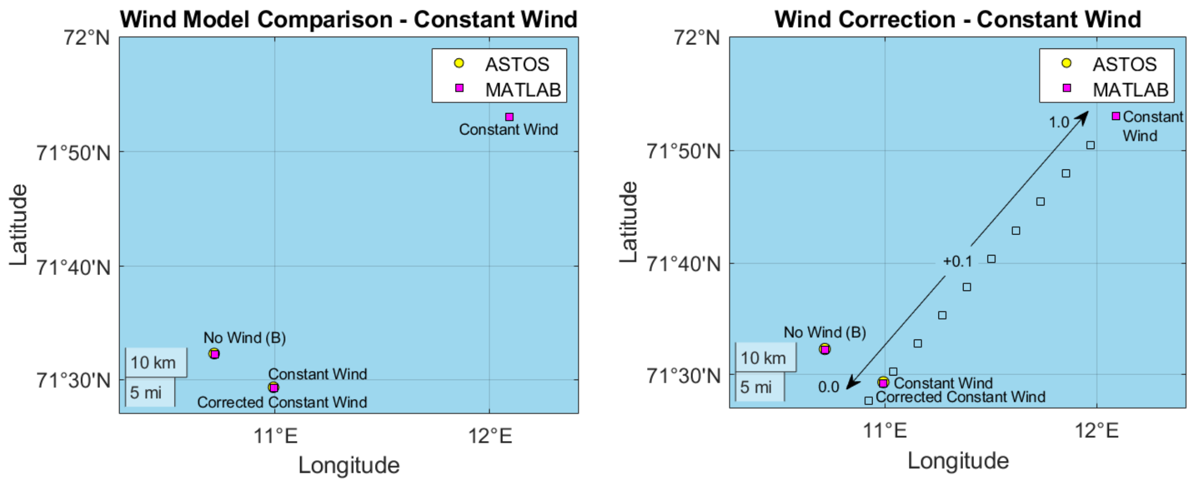

(a) Verification of the updated correction factor in 'Corrected Constant Wind', compared to the original correction factor in 'Constant Wind'.

(b) Determining the desired correction factor to match the results from the pre-flight nominal trajectory model.

Figure 7.3: Implementation of the updated wind scaling factor for a fictitious constant wind magnitude of 2 m/s up to 45 km.

7.1.3. Combined Effects of the Environment Model Aspects

After determining that all individual environment model aspects have been implemented correctly, the combined effects are evaluated. Again, the resulting IIP prediction for full environment model implementation is compared to the results of the nominal trajectory model.

Figure 7.4 shows the IIPs for full environment model implementation, as well as those for the baseline environment model as a comparison. Again, the results are provided for both the initial and updated wind correction factors. This figure shows that, after implementing the updated corrected wind model, the predicted IIP for the full environment implementation lies very close to that of the nominal trajectory model at a distance of approximately 40 m. This confirms that the updated wind scaling factor is still valid when observing the combined effects of the full environment model. The observed deviation is similar to that of the baseline model comparison, which was discussed earlier. The full implementation of the environment model is therefore considered to be verified, meeting the accuracy requirements, and will be used in all IIP predictions in the remainder of this report.

7.2. Accuracy of the IIP Prediction for a Nominal Input State Vector

The previous section showed that the nominal IIPs of the IIP prediction model and the 'baseline + environment' nominal trajectory model version met the accuracy requirements. However, this is not the only factor that determines the accuracy of the IIP prediction model. In this section, the full trajectory is observed to determine similarities and differences between the pre-flight nominal trajectory model versions and the IIP prediction model. The pre-flight nominal trajectory model results are used to estimate the accuracy of the IIP prediction model, since no actual DART XL flight data is available. It therefore serves as a comparison to the models created in an established software, as well as with more degrees of freedom.

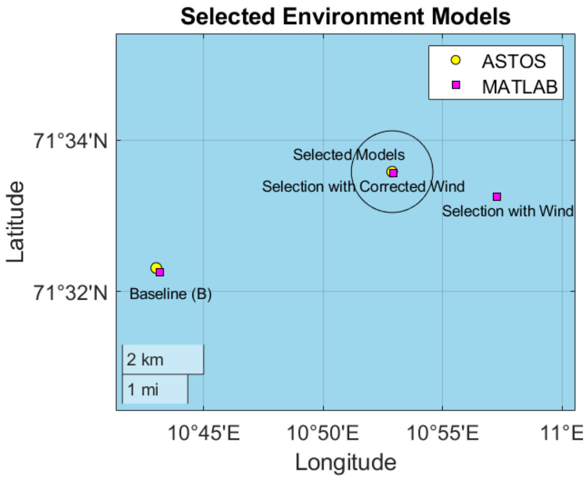

Figure 7.4: Combined implementation of all selected environment model aspects, compared to the nominal trajectory model results with respect to the required 1 km accuracy radius.

For all trajectory model versions, Figure 7.5 shows the ground track of each. This comparison was already done for the three nominal trajectory model versions in Section 5.2. From the figure shown here, in which the trajectory of the IIP prediction model was added, the ground tracks seem to closely overlap each other. This shows confidence in the fact that the differences between the models is small. Furthermore, this appears to verify that the IIP prediction model accurately replicates the results of the nominal trajectory model versions. Figure 7.6 shows the horizontal distance versus altitude for all trajectory model versions. Here, it can again be observed that the trajectory of the IIP prediction model is very similar to those of the pre-flight nominal trajectory model versions.

In the highlighted boxes in both figures, a slight difference in the trajectories becomes apparent. The trajectory of the IIP prediction model does seem to align the closest to the 'baseline + environment' nominal trajectory model. This was to be expected, since this baseline model was used to verify the implementation of the IIP prediction model.

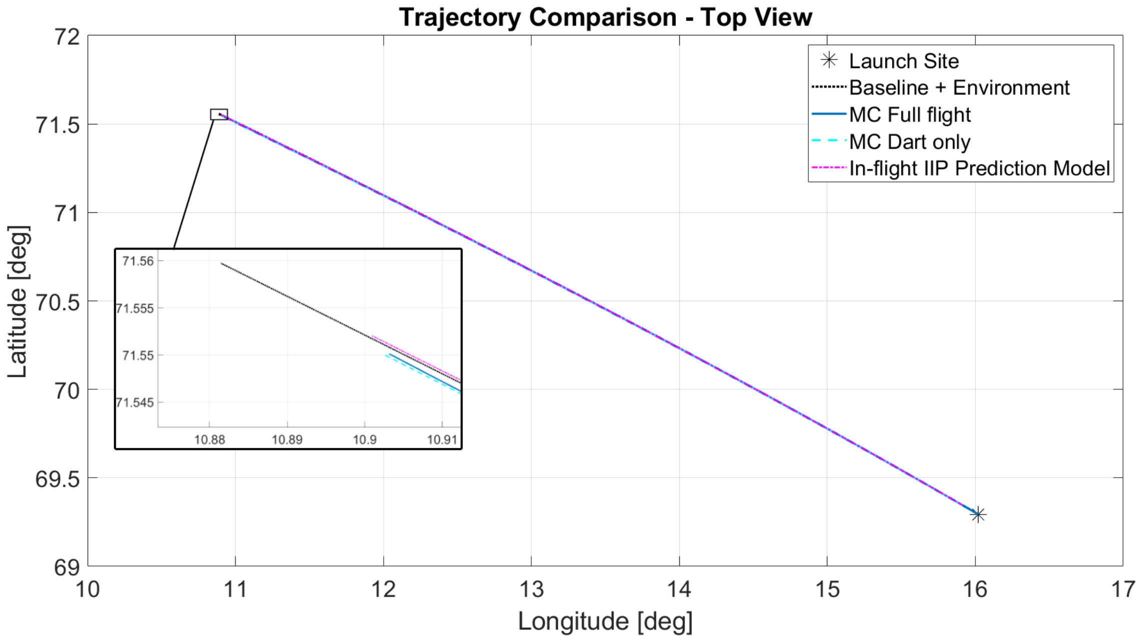

Figure 7.5: Latitude and longitude coordinate comparison for the pre-flight nominal trajectory model versions and the IIP prediction model. The window shows a zoomed in view of the impact points of each model.

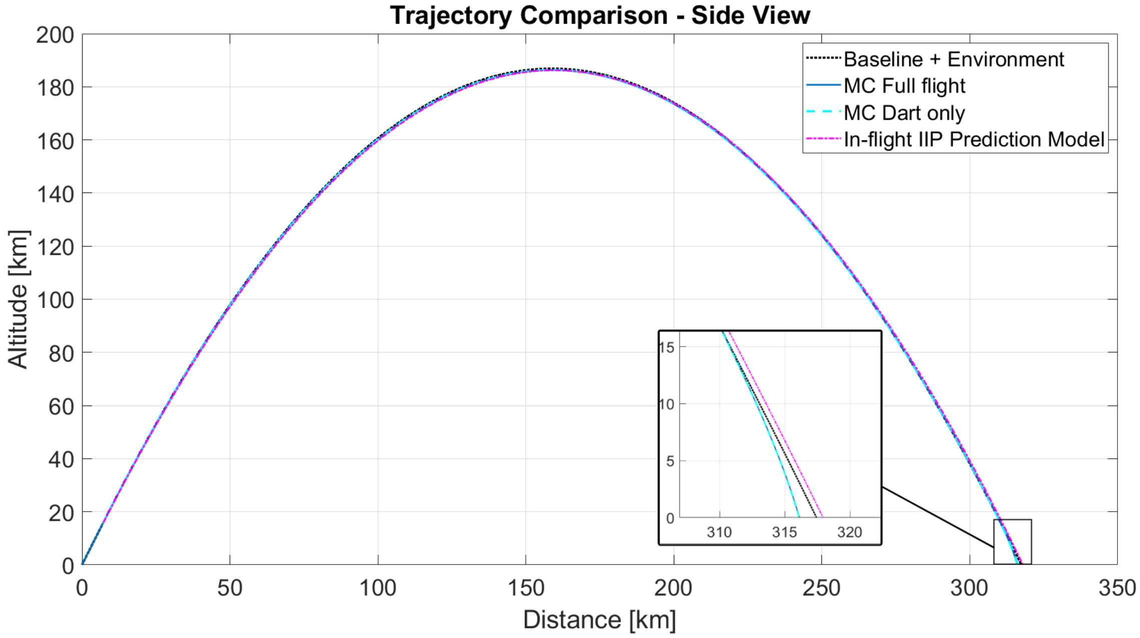

Figure 7.6: Horizontal distance and altitude comparison for the pre-flight nominal trajectory model versions and the IIP prediction model. The window shows a zoomed in view of the impact points of each model.

Figure 7.7 provides an overview of the IIPs with respect to each other. The 'baseline + environment' datapoints were already confirmed to be very close at a distance of 40 m in Section 7.1.3. When providing the IIP prediction model with the initial state vector of the expanded nominal trajectory model, the resulting IIP prediction lies further away from the expected coordinates. This difference between the IIPs labelled by 'Expanded Model' was calculated to be approximately 687 m. This shows that the IIP prediction model is less accurate with respect to an expanded model of more degrees of freedom with non-zero aerodynamic angles. However, it also shows that, despite this difference, the IIP accuracy still falls within the required 1 km radius.

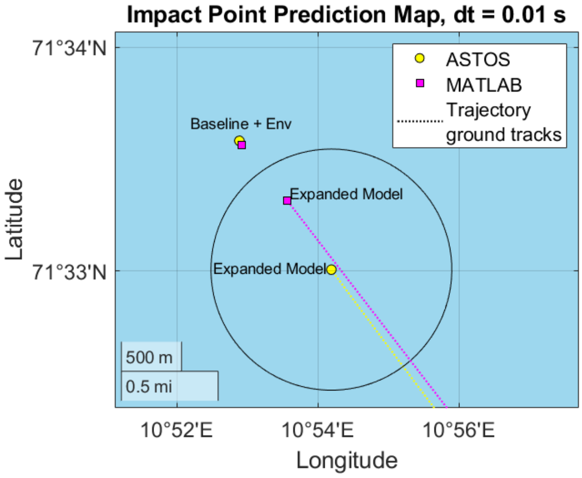

Figure 7.7: IIP prediction model results for an initial state vector of the baseline + environment and the expanded pre-flight nominal trajectory models, for a step-size of $dt = 0.01$ s.

Overall, the figures presented in this section show that the results of the IIP prediction model are very similar to those of the pre-flight nominal trajectory model results, and that its nominal IIP prediction meets the accuracy requirements.

7.3. Computation Time of the IIP Prediction for a Nominal Input State Vector

After implementing and verifying the implementation of the environment model and equations of motion for the nominal trajectory IIP prediction, the computation time of this model can be evaluated. All results presented in this section are based on simulations performed on the same device[1].

Figure 7.8 shows the computation time per run for a prediction from an initial state vector of the pre-flight nominal trajectory mode. Here, each run represents an initial state vector starting from the initial state vector at burnout, looping through each state vector until the final initial state vector immediately preceding impact.

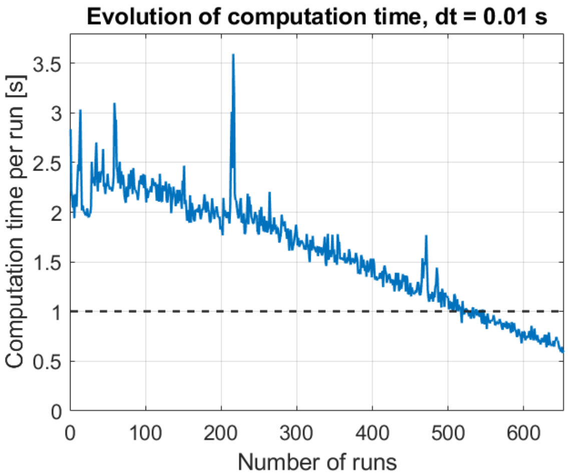

Figure 7.8: Computation time per run for each initial state vector between burnout and impact, for a step-size of dt = 0.01 s.

In this figure, it can be observed that the computation time for an integration step-size of 0.01 s does not meet the requirement of an update rate of 1 s or less. Adjustments to the model were made to optimise for speed, for example trying a simplified version of the output map visualisation and storing less variables in the memory. However, these adjustments did not manage to sufficiently decrease the computation time per IIP prediction to consistently fall below 1 s. As shown, this only happens toward the end of the simulation. Here, the initial state vector gets closer to impact and thus the remaining trajectory to propagate this state vector over becomes smaller. As a result, it was decided to try changing the integration step-size from 0.01 to 0.1 s.

Figure 7.9 shows the resulting computation time per run, evaluated for ten separate simulations. Two are highlighted for visualisation purposes. In this figure, it can be observed that the new integration step-size of 0.1 s does lead to a computation time that meets the requirement. In a few simulations, a spike in computation time was observed that caused the computation time to temporarily rise above the required 1 s. These spikes did not occur after a set number of initial state vectors, so it is not clear what caused them. A potential cause is computer background processes causing a temporary delay in the calculations.

These results lead to the conclusion that a change in integration step-size is required in order to meet the computation time requirement. However, it should be taken into account that this change also affects the model accuracy. Previously it was already determined that the development of the model implemented the environment models and equations of motion correctly, so these factors are not re-evaluated. To re-evaluate the model accuracy, the nominal IIPs for the baseline + environment and the expanded model version initial state vector are predicted once more. For the new integration step-size of 0.1 s, Figure 7.10 shows the resulting IIP predictions.

---

[1] HP Pavilion - 15-cs3721nd, with an Intel Core i7-1065G7 CPU @ 1.30GHz, with 16 GB of RAM and an NVIDIA GeForce MX250 graphics card

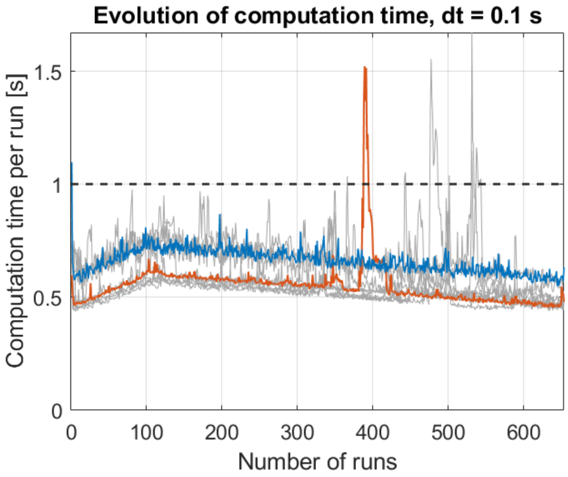

Figure 7.9: Computation time per run for each initial state vector between burnout and impact, for a step-size of dt = 0.1 s. Compilation of ten prediction simulations, with highlighted simulations for visualisation purposes only.

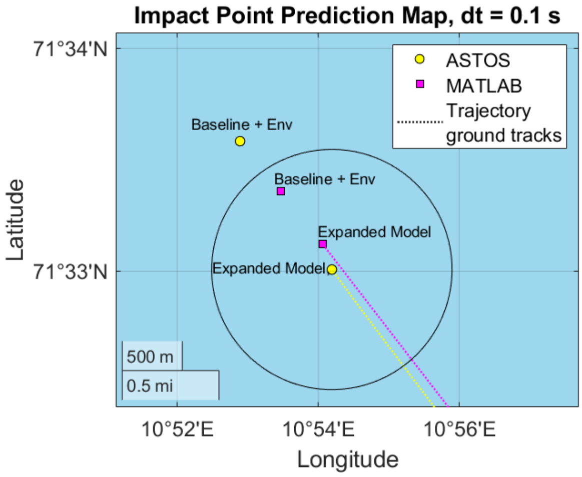

Figure 7.10: IIP prediction model results for an initial state vector of the baseline + environment and the expanded pre-flight nominal trajectory models, for a larger step-size of dt = 0.1 s.

Figure 7.10 shows a clear change in the location of the IIP predictions for both the baseline and expanded version of the initial state vector, compared to the results for a step-size of 0.01 s in Figure 7.7. However, the corresponding IIP predictions do continue to meet the accuracy requirement, as the IIP predictions fall within their respective 1 km accuracy radius. The difference between the baseline + environment model version IIPs was calculated to be approximately 541 m, whereas the difference between the expanded model version IIPs was calculated to be approximately 230 m. Therefore, the updated integration step-size of 0.1 s is accepted and implemented in the final IIP prediction model version, because its predictions meet the computation time as well as the accuracy requirements.

7.4. Output Presentation

This section presents the IIP prediction model outputs, as they would be shown to an RSO. The outputs were kept as minimal but complete as possible, to portray all necessary information in the most concise way. The visual part of the outputs is presented first and the numerical aspects are presented thereafter.

7.4.1. Visual Output - Map Projection

To best show the location of the impact point prediction, a map plot is displayed. As a reference, this map plot shows the allowable impact area boundaries and the location of the launch site. The IIP predictions are then added to this plot after each individual prediction.

Figure 7.11 shows the map plot that the RSO would monitor during a launch, at the actual figure size. After the first IIP prediction, based on the state vector immediately following motor burnout, the ballistic impact probability area is depicted with this first IIP prediction at its center. This aims to show a measure of uncertainty for the trajectory that the vehicle is on at the start of the ballistic phase. Furthermore, the most recent IIP prediction is displayed in blue, whereas previous predictions are visible in white to allow the observation of possible trends. Due to computation time and memory constraints, only the 100 predictions immediately preceding the most recent prediction remain visible.

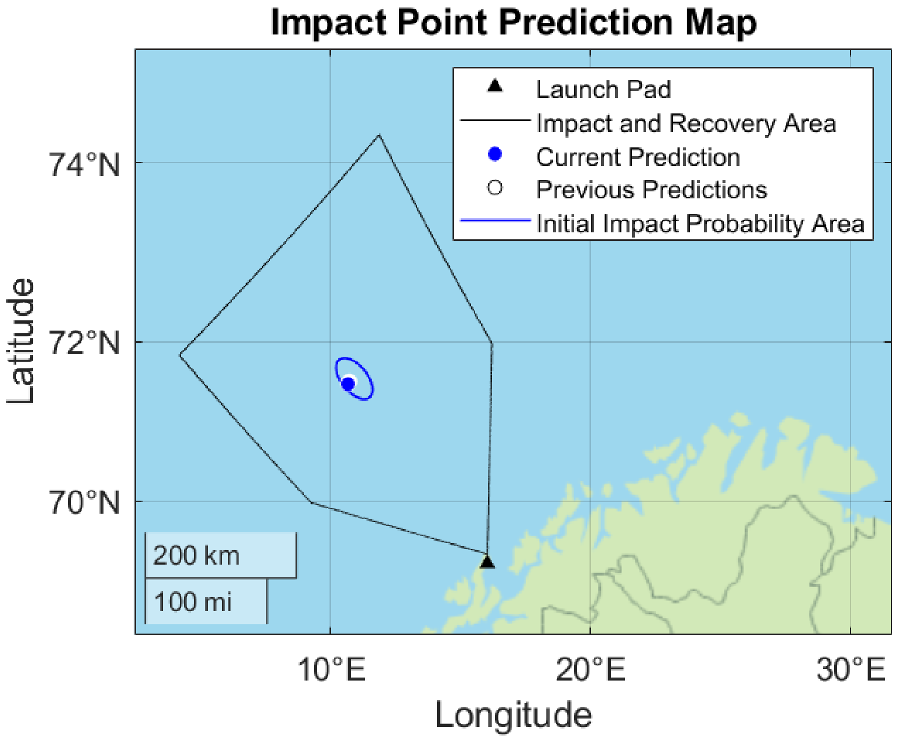

Figure 7.11: Visual output representation, as displayed to an RSO. To be updated with the most recent IIP prediction in real-time, with the previous 100 predictions visible for reference.

It was purposefully decided to have the map scaled to display the full allowable impact area, so the full situation can be observed at once. This figure is especially helpful to determine potential trends, and to easily observe the IIP prediction's location relative to the boundaries.

7.4.2. Numerical Output - Distance to Allowable Impact Area Boundaries

For an IIP prediction that is close to the boundaries, the presented map plot does not provide a clear unambiguous answer. In such a case, the provision of additional numerical information is essential.

The numerical outputs are presented in three parts, all of which are printed in the MATLAB command window for the current iteration of the IIP prediction model. Figure 7.12 shows the numerical outputs corresponding to the final three IIP predictions of Figure 7.11. The first line of the numerical output for each time step provides the time since launch of the initial state vector used for that prediction. This ensures that there is always a value that updates between predictions to show that the model is still running, even if the distance to the allowable impact area boundary remains constant. The second line of the numerical output for each time step provides the calculated shortest ground distance between the current IIP prediction and the closest point on the allowable impact area boundaries. A positive or negative sign is added as a visual indicator. Here, an IIP prediction inside the boundaries has a positive sign and a prediction outside the boundaries has a negative sign. The third line of the numerical output provides the word 'Inside' or '**OUTSIDE**' for additional clarity on the IIP's position with respect to the allowable impact area boundaries.

Lastly, when the IIP model detects two consecutive state vector polls returning the same vector, the IIP prediction process is paused in 1 s intervals before polling again after each interval. This is indicated in the command window by printing 'Waiting for new input data entries. IIP prediction is paused'. If a new input state vector is detected after pausing and waiting, the IIP prediction is resumed and printed in the command window as before. During this process, the previous predictions remain visible for the RSO to evaluate in the meantime.

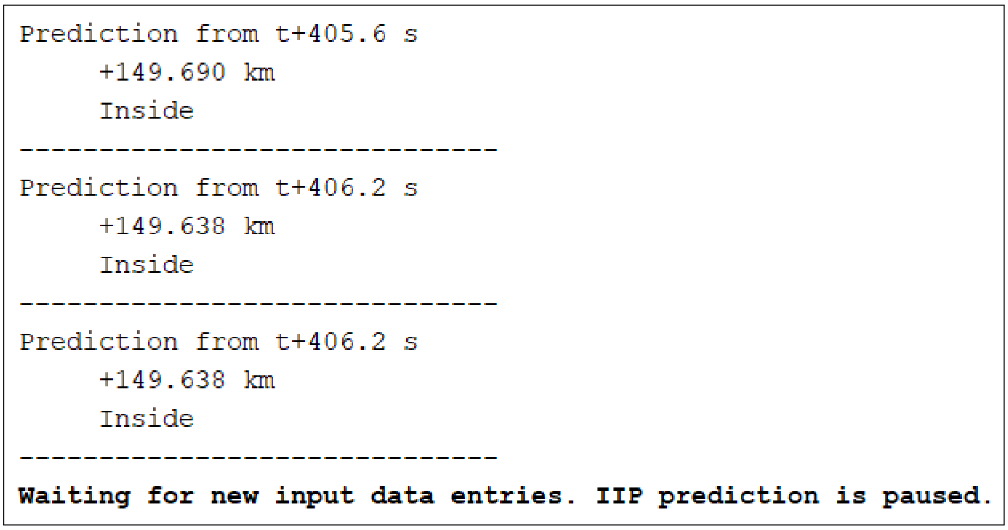

```
Prediction from t+405.6 s
     +149.690 km
     Inside
------------------------------
Prediction from t+406.2 s
     +149.638 km
     Inside
------------------------------
Prediction from t+406.2 s
     +149.638 km
     Inside
------------------------------
Waiting for new input data entries. IIP prediction is paused.
```

Figure 7.12: Numerical output presentation, as displayed to an RSO. Corresponding to the final three impact predictions of a simulation, with a message stating that IIP prediction has been (temporarily) paused due to a lack of new input data entries.

7.5. Model Testing for a Different Launch Location

This section evaluates the IIP prediction model for an alternative launch site, to evaluate the applicability of the model. The selected alternative launch site is Whalers Way, South Australia, because this was determined to provide the most contrast to the Andøya launch site in terms of coordinates and launch angles.

The launch coordinates are set at $(lat, lon) = (\lambda_0, \Lambda_0) = (-34.937611, 135.630045)$ deg for this launch from the Southern hemisphere. The exact coordinates of the Whalers Way launch facilities are not known, but this best estimate is considered sufficient for the current purpose. The launch angles are arbitrarily set at $(azimuth, elevation) = (\chi_0, \gamma_0) = (180, 60)$ deg, to again provide a meaningful contrast to the launch angles at Andøya by launching directly South. To provide an initial state vector, the Whalers Way launch was first simulated using the pre-launch nominal trajectory model. This was done for both the 'baseline + environment' model version as well as the expanded full flight model version.

Apart from the initial state vector and launch conditions, the remainder of the IIP prediction model is kept identical. This means that it also implements the same local wind profile that was determined for the Andøya vicinity. The wind model implementation was already verified for a different input profile in Figure 7.3, so it was not deemed necessary to perform an entirely new wind analysis for the Whalers Way site. Furthermore, the updated integration step-size of 0.1 s was implemented to further verify that this step-size yields results that meet the accuracy requirement.

Using the pre-flight nominal trajectory model initial state vectors, the accompanying nominal impact points and IIP predictions are presented in Figure 7.13. This figure shows that, for both the baseline and expanded model versions, the corresponding IIP predictions lie within the 1 km accuracy radius. Therefore, the IIP prediction model is considered to be verified for operation at more than one specific launch site.

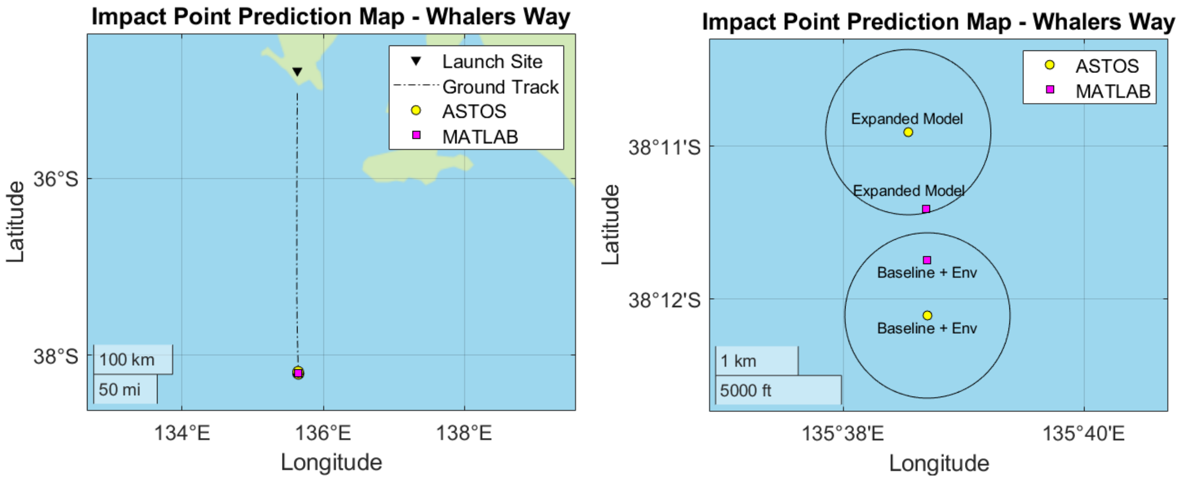

Figure 7.13: Impact point comparison for a launch from Whalers Way, South Australia, at an azimuth of 180 deg and an elevation of 60 deg. Zoomed in view on the right, with respect to the required 1 km accuracy radius.

8

Sensitivity Analysis

After developing, validating and verifying the model, the final step is determining the robustness of the model by performing a sensitivity analysis. This evaluates whether the results hold up when taking into account parameter uncertainties and whether the same conclusions can be made. The sensitivity analysis will focus on the in-flight IIP prediction model as the robustness of this model is most important in informing a flight termination decision. The pre-flight nominal trajectory model is not considered because this serves a more supportive role for the development of the in-flight IIP prediction model.

To perform the sensitivity analysis, the commonly used one-at-a-time (OAT) method is selected. This chapter first describes this OAT approach, followed by the analysed parameters. Finally, it presents the results of the sensitivity analysis as well as an evaluation of the robustness of the IIP prediction model.

8.1. One-at-a-Time Approach

As the name implies, the one-at-a-time method varies one parameter at a time at different values, while keeping all other parameters fixed. Whereas the Monte Carlo analysis focussed more on the effects of different trajectories on the impact point, the sensitivity analysis aims to take a step back and observe the effect of parameter uncertainties on these trajectories. The selected OAT method therefore evaluates the individual effect of varying a single parameter instead of parameter interactions. Using this method, each parameter of interest is varied over an interval of different values. This interval, as provided in Equation 8.1, is based on the mean and standard deviation of each parameter (Johnson, 2017). This process is then repeated for each parameter of interest.

$$[\mu - 3\sigma,\ \mu - 2\sigma,\ \mu - 1\sigma,\ \mu,\ \mu + 1\sigma,\ \mu + 2\sigma,\ \mu + 3\sigma] \tag{8.1}$$

Because this method only evaluates deviations in single parameters over an interval of few points, the results are aimed at providing a general understanding of the influence of deviations in these parameters and the model robustness.

8.2. Parameters of Interest and their Standard Deviations

The parameters of interest to vary in the OAT analysis are divided into two categories. First, the TRU input state vector is evaluated because it is the starting point of the trajectory prediction. Therefore, its uncertainty is expected to be of great influence on the resulting impact point due to error propagation. Furthermore, the Monte Carlo dispersion parameters of the ballistic model are evaluated to determine which of these are implemented in the IIP prediction model, and which of the implemented parameters are of interest for the sensitivity analysis. For each of the parameters presented in this section, only the 1-σ standard deviations is provided. The assumption is that it scales linearly, meaning that 2-σ and 3-σ are the double and triple of 1-σ respectively.

8.2.1. Initial State Vector

The TRU input state vector consists of six parameters, consisting of the position and velocity vectors in the three directions of the TRU frame. These are determined from accelerometer and gyroscope measurements taken by the TRU during a launch. Here, high-range accelerometers are used during the propelled flight phase, whereas high-accuracy accelerometers are used during the ballistic flight phase (Olthof, 2020).

These sensors come with their own characteristics and sensitivities, as detailed by their respective datasheets of which the relevant tables are provided in Appendix E. Some of the sensitivities stated in these tables, such as temperature sensitivities and gyroscope offsets, are accounted for during the pre-launch sensor calibrations and are therefore not relevant for this sensitivity analysis. Additionally, the TRU implements a moving average filter to compensate for noise. Only the factors that are accounted for in the sensitivity analysis, as determined in consultation with T-Minus, are discussed below.

Table 3 of STMicroelectronics (2013), provided in Figure E.1, presents the sensitivities of the high-range accelerometers used during the propelled flight phase. For the in-flight IIP prediction model, these sensitivities are used to determine the uncertainty of the initial state vector as propagated throughout the burn. The only sensitivity to account for during this propelled flight phase is the 'TyOff: Typical zero-g level offset accuracy'. The provided sensitivity of $\pm 1\ g$ is greatly reduced by the calibration steps, with an approximate factor of 100, but it does not become negligible. The expected remaining sensitivity is an offset of $\pm 10\ \mathrm{m}g$, where g is the sea level gravitational acceleration. Given that it is an acceleration offset factor, it propagates according to Equations 8.2 and 8.3.

$$\Delta V_{TRU,i} = g_{offset}\ \Delta t \tag{8.2}$$

$$\begin{aligned} \Delta S_{TRU,i} &= 1/2\ g_{offset}\ \Delta t^2 + \Delta V_{TRU,i}\ \Delta t \\ &= 3/2\ g_{offset}\ \Delta t^2 \end{aligned} \tag{8.3}$$

Here, the subscript i represents the three directions of the TRU frame. For a propelled phase of 15 s, this results in the expected 3-σ uncertainties in the velocity and position of the initial state vector being $\Delta V_{TRU,i} = 0.01 \cdot 9.80665 \cdot 15 \approx 1.4710$ m/s and $\Delta S_{TRU,i} = 3/2 \cdot 0.01 \cdot 9.80665 \cdot 15^2 \approx 33.0974$ m. The 1-σ uncertainties are therefore 0.4903 m/s and 11.0325 m.

Table 3 of STMicroelectronics (2017), provided in Figure E.2, presents the sensitivities of the high-accuracy accelerometers used during the ballistic flight phase. For the in-flight IIP prediction model, these sensitivities represent the uncertainty of the initial state vector measurement at the start of the ballistic phase. The only sensitivity to account for during the propelled flight phase is the 'LA_TyOff: Linear acceleration typical zero-g level offset accuracy'. The provided sensitivity of $\pm 40\ \mathrm{m}g$ is expected to be reduced by an approximate factor of 10 during calibration, so the expected remaining sensitivity is an offset of $\pm 4\ \mathrm{m}g$, where g is the sea level gravitational acceleration. Again, this acceleration offset factor propagates according to Equations 8.2 and 8.3. Because the sensitivity analysis evaluates the first state vector of the ballistic phase, the LA_TyOff is only propagated and evaluated for the first time step. The update rate of the TRU is 10 Hz, or 0.1 s. Therefore, the expected 3-σ uncertainties in the velocity and position of the initial ballistic state vector are $\Delta V_{TRU,i} = 0.004 \cdot 9.80665 \cdot 0.1 \approx 0.0039$ m/s and $\Delta S_{TRU,i} = 3/2 \cdot 0.004 \cdot 9.80665 \cdot 0.1^2 \approx 0.0006$ m. The 1-σ uncertainties are therefore 0.0013 m/s and 0.0002 m.

The sensitivity analysis will investigate how these errors in the state vector at the start of the ballistic phase propagate along the trajectory to an error in the final IIP prediction. The total 1-σ uncertainties of the initial ballistic state vector are presented in Table 8.1. By adding the values of the propelled flight phase to the initial error of the ballistic state vector, the totals were calculated to be 0.4916 m/s for the velocity components and 11.0327 m for the position components. The corresponding mean velocity and position values for each direction in the TRU frame are taken from the pre-flight nominal trajectory full flight version. These are presented in Table 8.2 at the end of this section.

Table 8.1: Individual components and total 1-σ uncertainties of the initial ballistic state vector of the DART XL Dart payload stage in the TRU frame.

	Propelled Flight Cumulative Error	Ballistic Flight Initial State Vector Error	Combined Error of the Initial State Vector
1-σ Velocity Error [m/s]	0.4903	0.0013	0.4916
1-σ Position Error [m]	11.0325	0.0002	11.0327

8.2.2. Selection from the Monte Carlo Dispersion Parameters

Alongside the TRU initial state vector, additional model parameters are selected from the Monte Carlo dispersion parameters of the ballistic flight model version, which were previously presented in Table 4.3. However, the in-flight IIP prediction model is based on a simplified baseline nominal trajectory model, in which not all Monte Carlo parameters are implemented. Only those parameters that are implemented in the IIP prediction model are considered for the sensitivity analysis. These are the atmospheric density scaling, Northern and Eastern wind scaling, structural mass and ballistic drag coefficient scaling of the Dart payload stage, as well as the launch azimuth. This section discussed each considered parameter and evaluates whether to include them into the sensitivity analysis. The launch elevation is not considered in this section because the IIP prediction model only takes into account the vehicle orientation at burnout. The vehicle elevation and azimuth at the point of motor burnout are however also not explicitly included, as these are calculated from the TRU input state vector. The mean and standard deviations for all considered parameters are presented here in Table 8.2. These are based on the values provided previously in Table 4.3.

Atmospheric Density Scaling

The atmospheric density used during the model development phase is based on the global US76 atmosphere model, meaning that it does not account for local and seasonal variations. Leading up to a launch campaign, however, it is extremely common to perform atmospheric measurements using a weather balloon. This would remove most of the uncertainties that remain between any location and the global model. It is therefore decided not to include the atmospheric density scaling in the sensitivity analysis, because most of the uncertainties can be taken into account by the aforementioned on-site weather balloon measurements.

Wind Scaling

The wind vectors used during the model development phase are based on a local monthly average, which does not account for daily variations or gusts. Similar to the atmospheric density, local winds are commonly measured by weather balloon leading up to a launch campaign. However, this would only remove some of the uncertainties. Due to the high variability in wind and its potentially large influence on the vehicle, the Northern and Eastern wind scaling factors are included in the sensitivity analysis. The profile that is varied is the same as was used throughout this report, based on the ERA5 database. For both the Northern and Eastern wind scaling factor, the mean and standard deviation are 1 ± 0.167. Within the IIP prediction model, the deviation of the wind scaling factor is implemented simultaneously to the wind scaling factor itself. The scaling factor is implemented at each time step during the equations of motion, where the estimated wind velocity components at the current altitude are added to the vehicle velocity components.

Dart Structural Mass

The structural mass of the Dart payload stage used during the model development phase is based on the average expected value of 14.0 kg. Therefore, this does not account for manufacturing and payload variations, which can introduce uncertainties. During a launch campaign, however, the individual Dart configuration that is used can be measured to determine its mass prior to launch. The value uncertainty would therefore only be dependent on the uncertainty of the measuring equipment used. It is therefore decided not to include the Dart structural mass in the sensitivity analysis, because most of the uncertainties can be taken into account for an individual Dart prior to launch.

Ballistic Dart Drag Coefficient Scaling

The drag coefficient of the Dart payload stage used during the model development phase is based on data provided by T-Minus. This does not account for manufacturing and assembly variations, which can introduce uncertainties. However, determining the precise drag coefficient of each individual Dart is unrealistic. Due to its potentially large influence on the vehicle it is therefore decided to include the ballistic Dart drag coefficient scaling in the sensitivity analysis. The scaling factor's mean and standard deviation are 1 ± 0.1. Within the IIP prediction model, the deviation of this scaling factor is implemented simultaneously to the ballistic Dart drag coefficient scaling factor itself. The scaling factor is implemented at each time step just before propagating the equations of motion, where the drag coefficient is determined from a lookup table containing the drag coefficient versus Mach number.

Launch Azimuth

The launch azimuth determines the orientation of the TRU reference frame. Even though it is not technically part of the ballistic phase, it can therefore still have a potentially large influence on the predicted impact point calculation. It is therefore decided to include it in the sensitivity analysis. From Table 4.2, its mean and standard deviation are 324.1 ± 1.0 deg. It is important to note here that this only considers the orientation of the TRU frame itself, since the actual azimuth of the vehicle orientation is determined from the TRU measurements. Within the IIP prediction model, the deviation of the launch azimuth is implemented only during the initialisation of the IIP prediction model. This is where the orientation of the TRU frame is determined, which is then referenced throughout all IIP predictions.

8.2.3. Sensitivity Analysis Parameter Overview

For convenience, the table below provides an overview of all the parameters selected for the OAT sensitivity analysis. For each parameter, the mean and 1-σ standard deviation values are provided. Furthermore, each parameter is assigned a parameter index, which is referenced in the figures presented in the results section.

Table 8.2: Selected parameters for the one-at-a-time sensitivity analysis of the in-flight IIP prediction model.

Parameter	Index	Symbol	Unit	Mean μ	Std σ
TRU Input State Vector					
Velocity (Downrange)	1	$V_{TRU,x}$	m/s	846.7019	0.4916
Velocity (Crossrange)	2	$V_{TRU,y}$	m/s	-1.2338	0.4916
Velocity (Vertical)	3	$V_{TRU,z}$	m/s	1852.3144	0.4916
Position (Downrange)	4	$S_{TRU,x}$	m	7022.5079	11.0327
Position (Crossrange)	5	$S_{TRU,y}$	m	19.4980	11.0327
Position (Vertical)	6	$S_{TRU,z}$	m	15648.4378	11.0327
Environment					
Wind Scaling (Easterly)	7	$V_{w,E}$	-	1.0	0.167
Wind Scaling (Northerly)	8	$V_{w,N}$	-	1.0	0.167
Aerodynamics					
Ballistic Dart Drag Coefficient Scaling	9	$\Delta C_{D,d}$	-	1.0	0.1
Launch					
Launch Azimuth	10	χ_0	deg	324.1	1.0

8.3. Results

In this section, the results of the sensitivity analysis are provided. The results are presented to show the relative difference in downrange and crossrange distance with respect to the nominal IIP, when implementing a $\pm 1\sigma, \pm 2\sigma$ or $\pm 3\sigma$ uncertainty for each individual parameter.

In Figures 8.1 and 8.2, a blue indicator represents the difference cause by implementing a positive uncertainty ($+1\sigma, +2\sigma$ or $+3\sigma$). A red indicator represents the difference cause by implementing a negative uncertainty ($-1\sigma, -2\sigma$ or -3σ). Figure 8.1 represents the difference in downrange distance, whereas Figure 8.2 represents the difference in crossrange distance. The 1 km accuracy radius is indicated by the dashed horizontal lines.

For the sensitivity of the downrange distance, it can be observed that only the Dart drag coefficient, exceeds the accuracy limits. For the other parameters, the downrange velocity has the largest influence, followed by the vertical velocity and the vertical position respectively. All other parameters cause a non-observable downrange difference of less than 50 m for the $\pm 3\sigma$ values.

For the sensitivity of the crossrange distance, it can be observed that none of the parameters exceed the accuracy limits. However, it can be observed that the launch azimuth has the largest influence on the crossrange difference, followed by the crossrange velocity, the Dart drag coefficient and the Easterly wind scaling factor. All other parameters cause a non-observable crossrange difference of less than 30 m for the $\pm 3\sigma$ values.

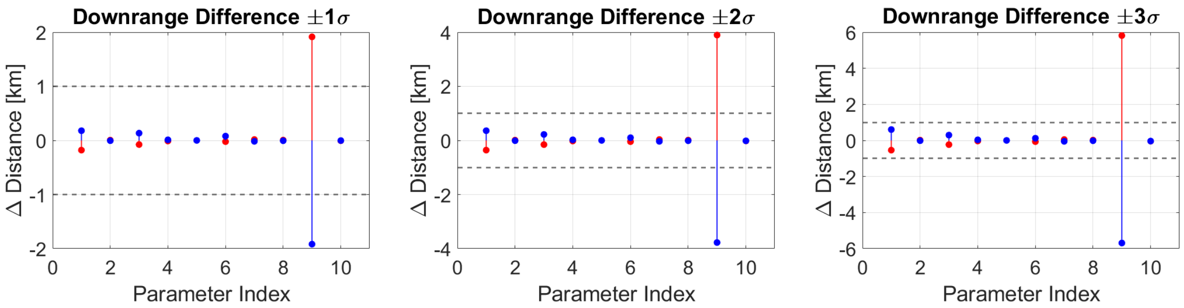
Downrange Difference $\pm 1\sigma$

Downrange Difference $\pm 2\sigma$

Downrange Difference $\pm 3\sigma$

(a) Difference in downrange distance for a 1-σ deviation.

(b) Difference in downrange distance for a 2-σ deviation.

(c) Difference in downrange distance for a 3-σ deviation.

Figure 8.1: The effect of parameter uncertainties on the downrange distance, with respect to the nominal IIP.

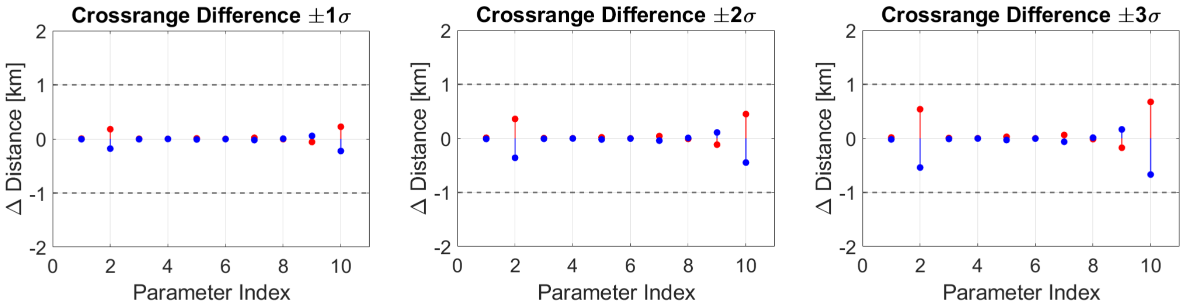
Crossrange Difference $\pm 1\sigma$

Crossrange Difference $\pm 2\sigma$

Crossrange Difference $\pm 3\sigma$

(a) Difference in crossrange distance for a 1-σ deviation.

(b) Difference in crossrange distance for a 2-σ deviation.

(c) Difference in crossrange distance for a 3-σ deviation.

Figure 8.2: The effect of parameter uncertainties on the crossrange distance, with respect to the nominal IIP.

Overall, the linear scaling of the standard deviations can be observed to produce a linear scaling of the difference in IIP position. For example, the downrange difference caused by the Dart drag coefficient (index 9) can be seen to double and triple between the $\pm 1\sigma$ results and the $\pm 2\sigma$ and $\pm 3\sigma$ results respectively. Furthermore, the presented results show that the Dart drag coefficient is the only parameter expected to have an uncertainty large enough to exceed the accuracy requirements. The model can therefore be considered to be relatively robust with respect to parameter uncertainties. This comes with the added sidenote that the Dart drag coefficient is a very important parameter for T-Minus to investigate further, to potentially decrease its expected uncertainty.

9

Conclusions & Recommendations

The objective of this thesis was ”*to predict the instantaneous impact point of a sounding rocket’s ballistic payload stage in (near) real-time, by creating a flight termination algorithm that predicts this impact point considering impact probability area boundaries and accuracy requirements, in order to increase launch safety.*” The evaluated sounding rocket is the DART XL by T-Minus Engineering B.V., consisting of a propelled booster stage containing a solid rocket motor and a Dart payload stage. In order to meet this objective, two separate models were created. The first was a pre-flight nominal trajectory model aimed at evaluating the nominal trajectory and thereby producing inputs and verification tools for the second model. The second model, the in-flight instantaneous impact point (IIP) prediction model was the main focus of the thesis work. This model is intended to run during a DART XL launch to predict the ballistic trajectory and IIP of the Dart stage in the post-separation phase. As part of the custom flight termination system T-Minus is developing, this algorithm will continuously update and display its IIP predictions to a range safety officer (RSO) as a flight termination advice. This chapter will present the conclusions gained from developing and evaluating these models, in general and with respect to the research questions. Furthermore, recommendations for future work are provided to aid in the expansion and improvement of the current iteration of the developed models.

9.1. Conclusions and Evaluation of the Research Questions

This section evaluates the conclusions of the thesis work in a general context and with respect to the research questions. As an additional stakeholder, the requirements set by T-Minus are also considered. Most requirements aimed to provide a framework within which to develop the pre-flight and in-flight models. All such requirements were met, because they were integral in defining the boundaries within which the models were developed in the first place. The remaining requirements to consider in the model development pertained to the accuracy and computation time of the IIP prediction model.

An important element of developing both models was selecting the environment model aspects, with respect to the required 1 km accuracy radius. The final environment model selection consists of a US76 atmospheric model, a central gravity model with the addition of the J_2 effect, the inclusion of a local wind model and a rotating, ellipsoidal Earth model. This environment model definition was used for both the pre-flight and the in-flight models. Compared to the environment model aspects, the model’s number of degrees of freedom was determined to have a less notable influence on the trajectory and IIP prediction. Here, a 3-degrees of freedom (3-DoF) model was found to predict impact points close to those predicted using a model of more degrees of freedom. The only complication posed by developing the IIP prediction model as a 3-DoF model, was that the local wind model required a correction factor because this excluded the influence of the vehicle’s rotational inertia causing a delay in the effects of wind. In general, it can therefore be concluded that the same overall model definitions can be used for both the pre-flight and the in-flight models, with the slight exception of the local wind correction factor. Additionally, it was concluded that the number of degrees of freedom does not have to be equal.

The IIP prediction model was thus developed as a 3-DoF model, implementing the selected environment model aspects. To determine whether the resulting model meets the 1 s computation time requirement, initially the IIP prediction model was evaluated using a step-size of 0.01 s. However, this did not meet the computation time requirement, and modifications to the model such as simplifying the map output did not have a large enough effect on the overall computation time using this step-size. Therefore, it was decided to change the integration step-size to 0.1 s and re-evaluate the accuracy and computation time of the resulting model. With the updated step-size of 0.1 s, the model computation time was consistently smaller than 1 s with the exception of a few unidentified spikes.

To determine whether this IIP prediciton model also meets the 1 km accuracy requirement, the nominal IIP results of the pre-flight nominal trajectory model were used as a means of verification for the results of the IIP prediction model. By comparison, it was concluded that the accuracy requirement was met for both the initial integration step-size of 0.01 s and the updated step-size of 0.1 s. For a step-size of 0.01 s the distance to the verification IIP was less than 700 m and for a step-size of 0.1 the distance to the verification IIP was less than 600 m. The updated step-size of 0.1 s was therefore used in the final IIP prediction model.

Additionally, the expected nominal impact point distribution was determined by performing Monte Carlo simulations using the pre-flight nominal trajectory model. The input parameters to vary were determined for two trajectories: the full flight from launch to impact and only the ballistic flight from burnout to impact. All parameters to include or exclude were carefully considered and discussed in consultation with T-Minus, with a focus on non-design parameters. From the resulting IIP distribution and 3-σ impact probability area, it was concluded that the expected uncertainty of an IIP propagated from the beginning of the ballistic phase was much smaller than that of an IIP propagated from lift-off. This result is in line with expectations, since the ballistic trajectory simulations exclude errors occurring during the propelled flight and the remaining errors have less time to propagate before impact. Furthermore, the uncertainty in the downrange direction was found to be larger than the uncertainty in the crossrange direction, which was to be expected due to the larger influence of errors in the direction of flight.

The influence of individual parameters or combinations of several parameters within the Monte Carlo IIP dispersion was not evaluated. The effect of varying individual parameters using a One-at-a-Time approach was investigated in a sensitivity analysis. Out of the ten investigated parameters, only the drag coefficient of the ballistic Dart payload stage was found to have an influence that exceeds the 1 km accuracy radius.

Finally, the IIP prediction is continuously updated and displayed to an RSO during a launch, to allow them to monitor the vehicle's expected IIP in near real-time. This is achieved by the development of a map plot to visually show the location of the IIP prediction relative to the launch site's allowable impact area boundaries, a numerical value output representing the shortest ground distance between the prediction and these boundaries, as well as a visual indicator accompanying the numerical value output to quickly identify whether the prediction lies inside or outside of these boundaries.

In conclusion, the development of the pre-flight nominal trajectory model and the in-flight IIP prediction model has successfully produced results that answer all research questions and meet all research objectives. Furthermore, all requirements set by T-Minus are met when considering a nominal IIP prediction. It should be noted that uncertainties remain in this nominal prediction larger than the desired 1 km accuracy radius, represented by for example the ballistic impact probability area and Dart drag coefficient. However, it is unlikely that the uncertainty of the nominal IIP prediction can be decreased below a radius of 1 km due to the inherent unpredictability of launch conditions. Overall, it is therefore concluded that the thesis work is considered to have successfully developed a model for the near real-time instantaneous impact point prediction of the DART XL sounding rocket's Dart payload stage.

9.2. Recommendations for Future Work

The current research and the resulting model development was aimed at providing a first iteration of an instantaneous impact point prediction model, custom-built for the flight termination system of the DART XL. The focus was mostly on selecting model definitions that would allow this first iteration to answer the research questions and meet the requirements, to provide an RSO with the minimal required data to serve as a flight termination advice. Therefore, many model aspects and additions remain unexplored that could guide future potential research areas. These aspects are discussed in this section.

Investigate individual parameters influences on the IIP dispersion
To gain insight into parameter influences on the vehicle's expected impact point, it is recommended to investigate which parameters or combinations of several parameters have the largest influence on the IIP dispersions resulting from the Monte Carlo simulations. This knowledge will aid T-Minus in evaluating which parameters to focus on during the vehicle development stage, to further decrease the expected uncertainty of the nominal IIP and the subsequent impact probability area.

Reduce uncertainty of the Dart drag coefficient
As determined in the sensitivity analysis, uncertainties of the drag coefficient of the ballistic Dart payload stage have a large influence on the predicted IIP location, much larger than any other investigated parameter. Gaining more detailed knowledge of this coefficient is therefore key to decrease its expected uncertainty and thereby increase the accuracy of IIP predictions during a launch.

Investigate implementing a variable step-size integrator
The current iteration of the in-flight IIP prediction model uses an Euler integrator with a fixed step-size of 0.1 s. Smaller step-sizes did not meet the computation time requirements. As an alternative, it is recommended to investigate the effects of implementing a variable step-size integrator such as the Runge-Kutta4(5) or the Dormand-Prince 4/5 used in the pre-flight model. This allows for a potential decrease in the computation time, while simultaneously being able to implement a smaller minimal step size and continuing to meet the accuracy requirements.

Adapt model to integrate with TRU input data
Currently, the IIP prediction model uses a substitute input initial state vector taken from the nominal trajectory model, because no actual TRU flight data is currently available. Once TRU flight data does exist, it is therefore recommended to adapt the model to implement this data and remove any subsequent conversions that were required to implement the substitute input vector. Only after this integration with the TRU can the IIP prediction model be implemented during a launch.

Implement additional aerodynamic data into the pre-flight nominal trajectory model
To increase the accuracy of the pre-flight nominal trajectory model, it is recommended to implement additional aerodynamic data such as the lift coefficient and aerodynamic moments into this model. For this first iteration, this data was not available. However, including this data into the pre-flight model can potentially influence the validity of the in-flight IIP prediction model definitions, because this uses the pre-flight model results as a verification tool.

Investigate how to display previous IIP predictions on the map plot
Currently, the map plot displayed to the RSO shows not only the most recent IIP prediction, but also the preceding 100 predictions. These provide the RSO with a reference point and a means to observe potential trends. However, this means that any predictions further back in time than the preceding 100 are no longer displayed. It is therefore recommended to investigate other ways of displaying preceding IIP predictions. A suggestion is to display past IIP prediction at 5 second intervals following lift-off to provide a more general overview.

Test the in-flight IIP prediction model on different devices
The IIP prediction model was developed and tested on a single device. Any computation time considerations are therefore also based on the performance of this device. It is therefore recommended to perform additional model and computation time evaluations on different devices, preferably including the device that will act as a ground station for the RSO during launch.

A

Additional Model Inputs

This appendix presents additional model inputs for the DART XL trajectory model. It is therefore supplementary to Chapter 3. The inputs presented are mostly in figure form, providing a variable profile for a parameter. Furthermore, this appendix also details how the sea level thrust measurements were converted to vacuum thrust data.

A.1. Sea Level Thrust Measurements

The sea level thrust is based on static test data for the DART XL SRM. In particular, the data used was of the static test performed on November 30th 2020 at ASK 't Harde. The thrust that was measured during this test, for an initial propellant mass of 99.82 kg, is provided in Figure A.1. Shown in this figure is the calibrated and post-processed thrust data. From this, the specific impulse was calculated to be Isp_{sea} = 241.61 s, using Equation A.1 from Sutton and Biblarz (2010).

$$Isp = \frac{\int_0^t F dt}{g_0 \int \dot{m}_p dt} \tag{A.1}$$

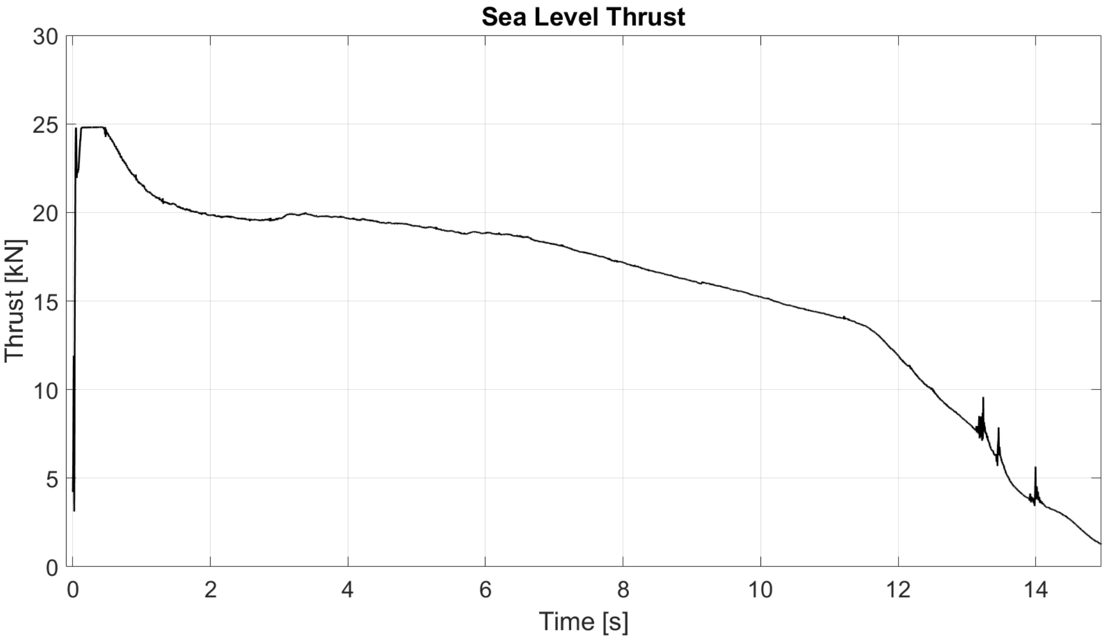

Figure A.1: Sea level thrust, measured from a DART XL SRM static test.

A.2. Vacuum Thrust Conversion

As stated in Section 3.3.2, in order to create a trajectory model in ASTOS, the vacuum thrust and vacuum Isp_{vac} need to be used as an input. The only available data for the thrust profile of the DART XL SRM stems from sea level static tests. Therefore, this section details how the sea level thrust curve and Isp_{sea}, as presented in the previous section, were converted to vacuum data. All equations used in this section are taken from Chapter 2 and 3 of Sutton and Biblarz (2010). It is important to note here that these equations assume an ideal gas, and therefore provide only a best estimate of the vacuum conditions.

Before going into the equations that were used for the thrust conversion, a few additional parameters and indices are defined that are used throughout this appendix. The indices used represent different parts of the nozzle, as shown in Figure A.2 for a nozzle of arbitrary dimensions. The additional parameters and their values are listed in Table A.1, with parameters that are yet to be calculated listed as 'TBD'.

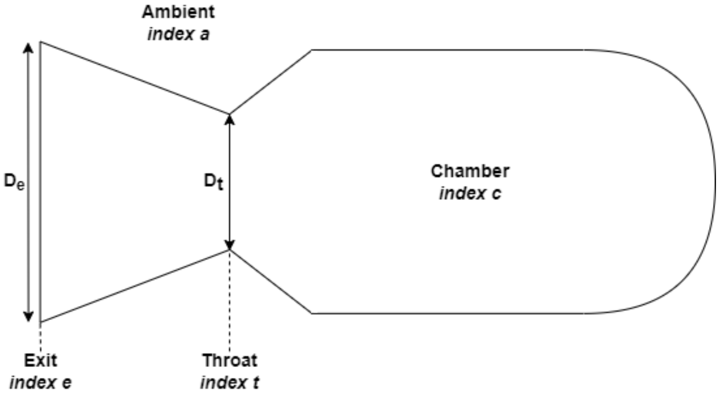

Figure A.2: Nozzle geometry for a nozzle of arbitrary dimensions.

Table A.1: Descriptions and values of variables used for the thrust conversion.

Symbol	Description	Unit	Value
$C_{F,sea}$	Thrust coefficient at sea level	-	TBD
$C_{F,vac}$	Thrust coefficient in vacuum	-	TBD
D_e	Nozzle exit diameter	mm	140
D_t	Nozzle throat diameter	mm	55
ϵ	Nozzle area ratio	-	6.48
F_{sea}	Sea level thrust	N	Measured
F_{vac}	Vacuum thrust	N	TBD
k	Specific heat ratio	-	1.2
$P_{a,sea}$	Ambient pressure at sea level	Pa	101325
$P_{a,vac}$	Ambient pressure in vacuum	Pa	0
P_c	Chamber pressure	Pa	Measured
P_e	Exit pressure	Pa	TBD

All sea level parameters are based on the static test data. Furthermore, k = 1.2 is an estimate of a constant specific heat ratio that is based on the theoretical specific heat ratios at various locations in the nozzle, as provided by T-Minus.

The first step of the thrust conversion is to calculate the exit pressure P_e. It can be determined using Equation A.2, where the exit pressure is the only unknown given the chamber pressure that was measured during the static test. Considering the fact that the chamber pressure is measured as a function of time, the accompanying exit pressure is calculated for every time step to determine the exit pressure as a function of time.

$$\frac{A_t}{A_e} = \left(\frac{k+1}{2}\right)^{1/(k-1)} \left(\frac{P_e}{P_c}\right)^{1/k} \sqrt{\frac{k+1}{k-1}\left(1-\left(\frac{P_e}{P_c}\right)^{(k-1)/k}\right)} \tag{A.2}$$

where the ratio between the nozzle exit area and throat area is defined as

$$\frac{A_e}{A_t} = \epsilon = \frac{\pi\ (D_e/2)^2}{\pi\ (D_t/2)^2} = \left(\frac{D_e}{D_t}\right)^2 \tag{A.3}$$

The resulting pressure ratio is a constant factor of $P_c/P_e \approx 44.64$ with an area ratio of $\epsilon \approx 6.48$. For verification, it is determined that this value matches the the expected value from literature using Figure A.3.

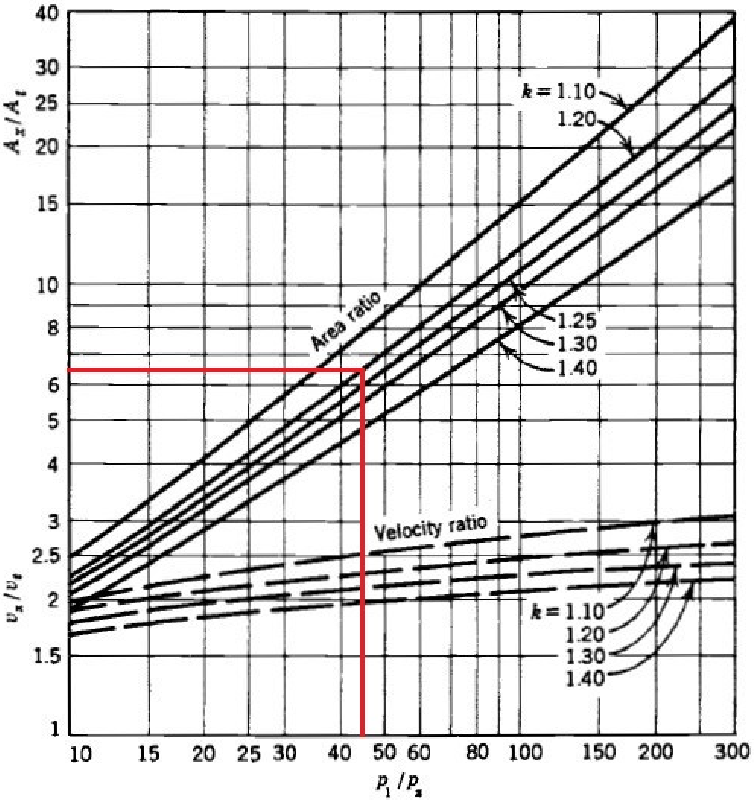

Figure A.3: Area and velocity ratios as a function of pressure ratio for the diverging section of a supersonic nozzle, with added indicators for the DART XL nozzle in red.
[Source: Figure 3-4 from Sutton and Biblarz, 2010]

After calculating and verifying the exit pressure, the sea level and vacuum thrust coefficients can be calculated using Equation A.4. Here, the only factor that differentiates $C_{F,sea}$ from $C_{F,vac}$ is the ambient pressure P_a. The thrust coefficients calculated with this equation are provided in Figure A.4.

$$C_F = \sqrt{\frac{2k^2}{k-1}\left(\frac{2}{k+1}\right)^{(k+1)/(k-1)}\left(1-\left(\frac{P_e}{P_c}\right)^{(k-1)/k}\right)} + \frac{P_e - P_a}{P_c}\frac{A_e}{A_t} \tag{A.4}$$

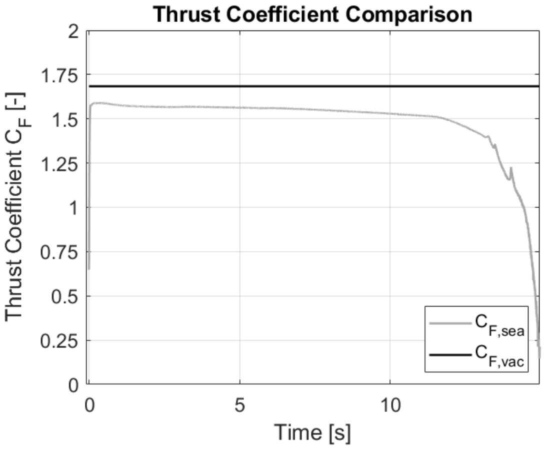

Figure A.4: Calculated thrust coefficients at sea level and in vacuum as a function of burn time.

Again these parameters were verified using literature data from Sutton and Biblarz (2010). The vacuum coefficient $C_{F,vac}$ is calculated to be constant at 1.68. This is verified when looking at Figure A.5, given that the pressure ratio P_c/P_a goes to infinity in vacuum and ϵ = 6.48. The sea level coefficient $C_{F,sea}$ lies between 1.5-1.6 for the majority of the burn. This is verified when looking at Figure A.6, given that the pressure ratio is P_c/P_e = 44.64, k = 1.2 and ϵ = 6.48. It is noted that this figure represents optimum expansion conditions, which are not reached during the burn. Rather, the motor is slightly under-expanded at sea level. The purpose of this verification is thus to determine the general credibility of the estimate. Near the end of the burn a sudden drop in $C_{F,sea}$ is observed. This regime clearly shows the limitations of describing a motor test at sea level using equations considering an ideal gas.

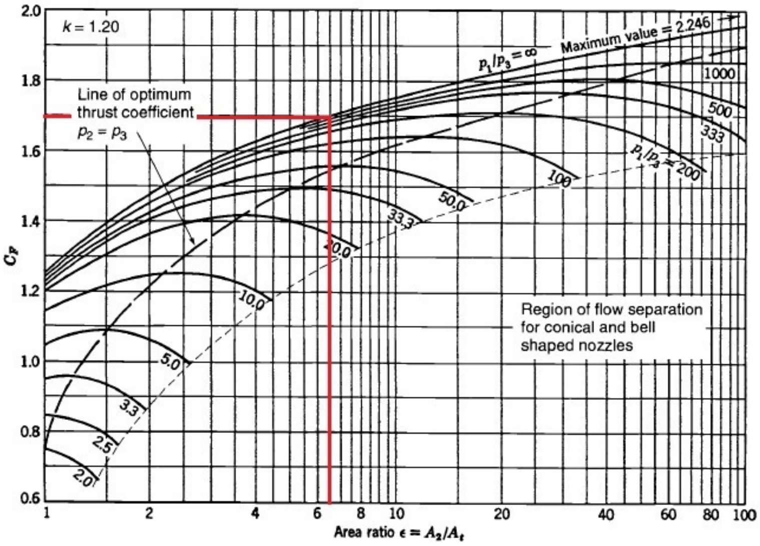

Figure A.5: Thrust coefficient C_F versus nozzle area ratio for k = 1.20, with added indicators for the DART XL nozzle in red. [Source: Figure 3-7 from Sutton and Biblarz, 2010]

Finally, after determining the thrust coefficients, the vacuum thrust can be calculated using Equation A.6 as derived from Equation A.5. The vacuum specific impulse is then calculated with Equation A.1.

$$F = C_F A_t P_c \tag{A.5}$$

$$F_{vac} = F_{sea} \frac{C_{F,vac}}{C_{F,sea}} \tag{A.6}$$

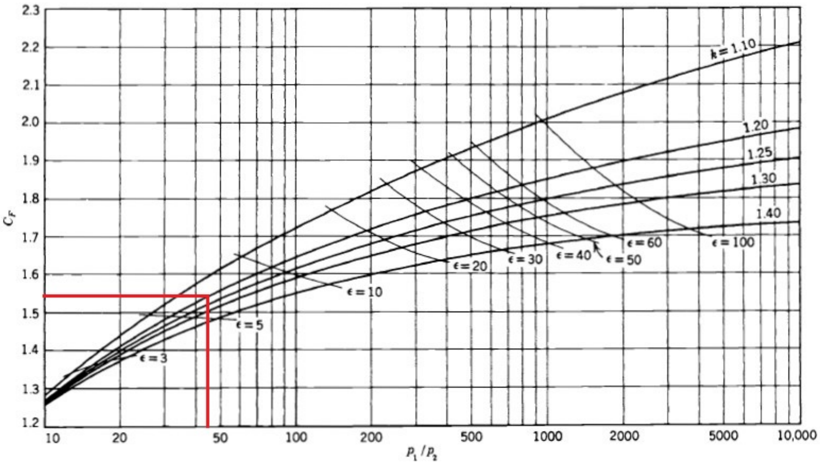

Figure A.6: Thrust coefficient C_F as a function of pressure ratio, nozzle area ratio, and specific heat ratio for optimum expansion conditions ($P_e = P_a$), with added indicators for the DART XL nozzle in red.
[Source: Figure 3-6 from Sutton and Biblarz, 2010]

The resulting vacuum thrust profile is shown in Figure A.7. This shows that during the final second of the burn, the calculated vacuum thrust experiences a sudden increase. This is not considered to be realistic behaviour, but rather an effect of the equations not being valid in this final regime of the burn, as previously mentioned. Therefore, a correction is applied to this final section of the burn. This correction factor was determined by looking at the difference between the vacuum and sea level thrust, as shown in Figure A.8. Here, the burn until t=1 s is not included to exclude ignition fluctuations. Additionally, the burn after 13 s is not considered as this is the regime that needs correcting. By applying a linear fit through the difference, the conversion factor for the final seconds of the burn becomes $F_{vac} = F_{sea} + fit$. This results in the dashed line shown in Figure A.7, representing the vacuum thrust that is used to perform the trajectory simulations. After implementing this correction, the corresponding vacuum specific impulse is calculated to be Isp_{vac} = 264.82 s.

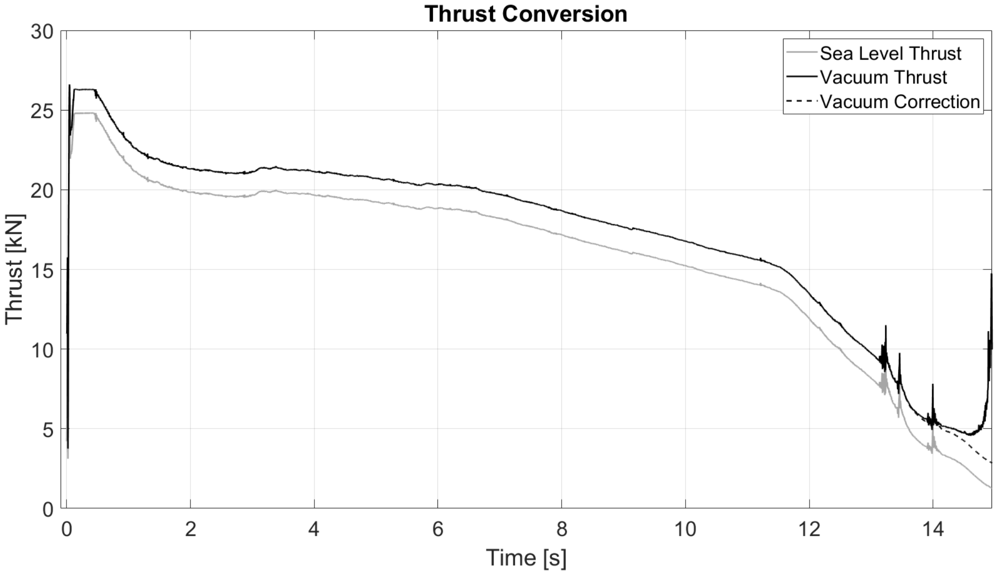

Figure A.7: Thrust conversion from sea level to vacuum as a function of burn time, where the dashed line represents the corrected vacuum thrust used in the trajectory simulations.

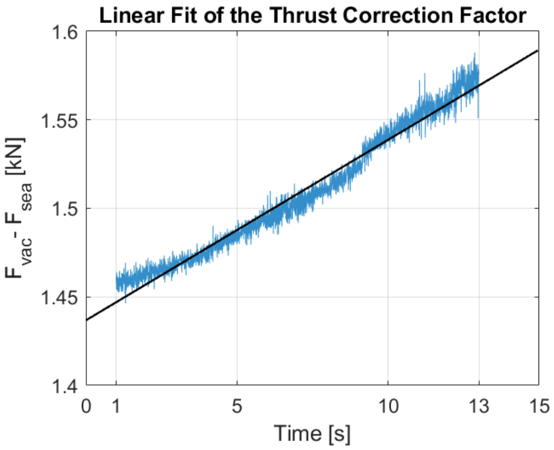

Figure A.8: Linear fit of the difference between the vacuum and sea level thrust as a function of burn time, to determine the correction factor.

A.3. Center of Pressure

This section presents the curve for the center of pressure with respect to Mach number for the DART XL, as determined by T-Minus Engineering. It is important to note here that this curve represents the center of pressure X_{CP} with respect to the nozzle end of the vehicle's booster.

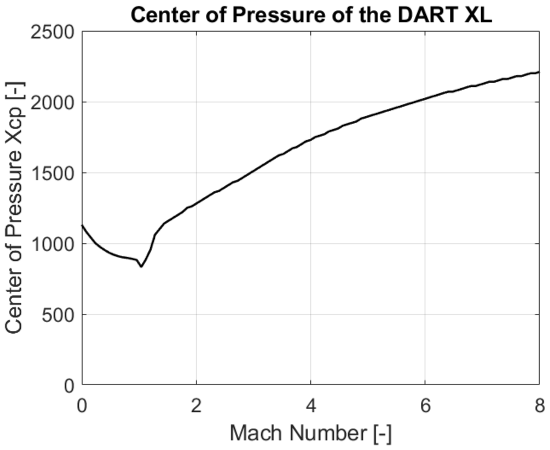

Figure A.9: Center of pressure versus Mach number of the DART XL.

A.4. Drag Coefficient

In this section, the drag coefficient data for the DART XL is presented, as determined by T-Minus Engineering. The drag coefficient C_D is presented in three different curves, with respect to Mach number. For the full configuration of the DART XL, meaning booster and Dart, the drag coefficient curve is given for the propelled version of this configuration as well as the unpropelled version. Lastly, the drag coefficient curve for the Dart stage by itself is provided.

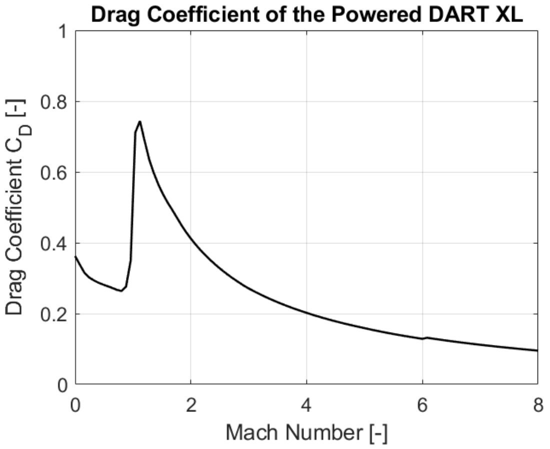

Figure A.10: Drag coefficient versus Mach number of the powered DART XL.

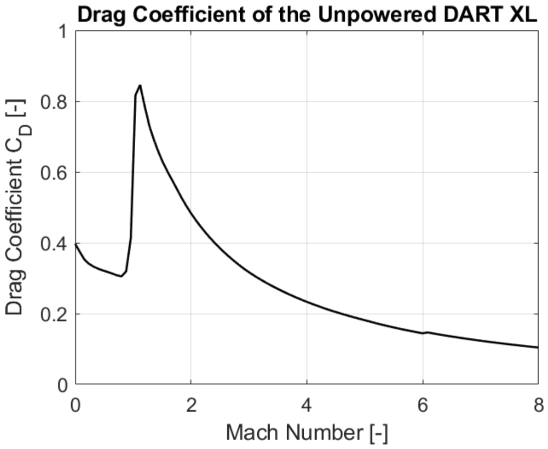

Figure A.11: Drag coefficient versus Mach number of the unpowered DART XL.

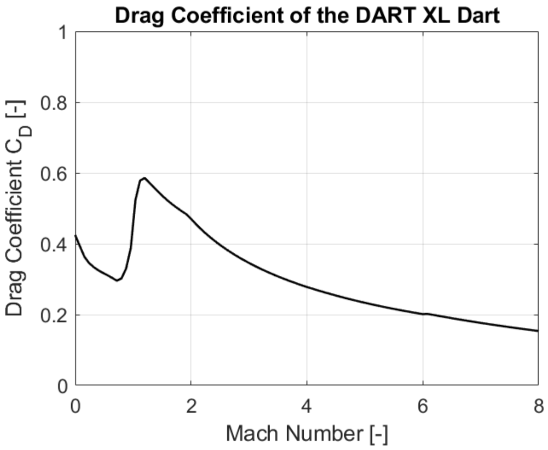

Figure A.12: Drag coefficient versus Mach number of the DART XL Dart payload stage.

B

Analysis of the Full Flight Model

The results presented in Sections 5.3 and 5.4 mainly discussed the results for the ballistic flight model version. Therefore, this appendix presents the results of the Monte Carlo analysis results for the expanded full flight model version, of which the 3-σ impact probability area was briefly discussed in Section 5.4. Furthermore, it presents evidence supporting the validity of the assumption of a zero roll rate during the ballistic flight phase, using the results of the full flight model version.

B.1. Monte Carlo Impact Point Distribution for the Full Flight

The analysis of the full flight Monte Carlo results was performed similar to the method presented for the Monte Carlo results of the ballistic model version. This section first presents the spread of the IIP dispersion relative to the nominal impact point, which resulted from the Monte Carlo simulations. Furthermore, a convergence analysis is done along with an evaluation of the impact point distribution.

Figure B.1 shows the results of the Monte Carlo impact point dispersion, for 25000 individual runs representing uncertainties during the entirety of the flight. Here, a large spread of the impact points can be observed. This indicates that the effect of varying the dispersion parameters is high. Compared to the spread for the ballistic phase, this spread is expectedly much larger as more parameters are varied and each parameter can propagate over a longer time. Additionally, it can be seen that the spread is higher in the downrange direction than in the crossrange direction, but that the elliptical shape is much less eccentric than that of the ballistic phase. It does, however, show the expected elongation in the downrange direction caused by the fact that uncertainties are generally larger in the downrange direction than the crossrange direction. Again, it was not investigated which parameters caused the largest spread, as acquiring data for individual parameters would require a lot of additional work that is not directly relevant to the model moving forward and is therefore out of the scope of this project.

The impact point data forms a bivariate normal distribution with latitude and longitude as the variables, which is visualised in Figure B.2 along with a normal distribution fit of each. This figure shows that both the latitude and the longitude are indeed normally distributed, which is to be expected given that almost all the input dispersion parameters are normally distributed. These distributions do skew towards lower latitudes and higher longitudes, which would indicate that there are more potential scenarios that negatively impact the trajectory by resulting in a below average impact distance.

The final step in presenting the Monte Carlo impact point distribution is evaluating the convergence and confidence interval of the data. Figure B.3 shows the convergence and 3-σ confidence interval for the latitude and longitude individually. The impact points presented above are indicated in this figure as '1st Batch', of which the moving average is visualised by the thick, solid black line. The red lines represent the confidence interval boundaries, calculated from this first batch. As observed, after about 1000 runs this moving average appears to converge. However, the confidence interval is still narrowing at this point. When taking into account all 25000 samples, the size of the confidence interval indicates certain convergence. It is important to note that there is a slight offset between the values the model converges to and the nominal latitude and longitude values, indicated by the dashed black lines. This difference shows that the mean IIP of the Monte Carlo simulation has a lower latitude and a higher

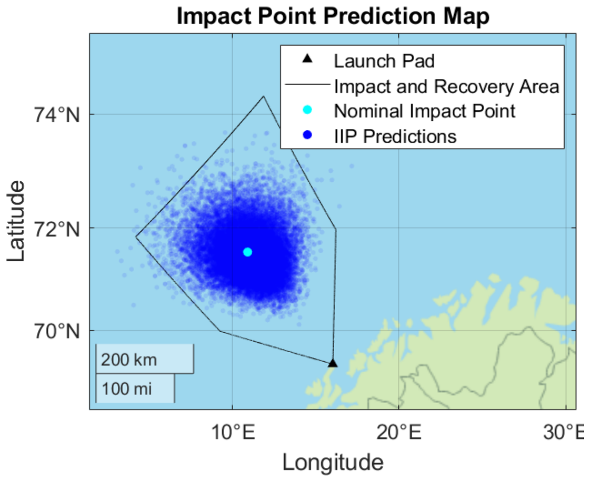

Figure B.1: Impact point distribution relative to the Andøya allowable impact area, for a Monte Carlo simulation of 25000 runs during the ballistic flight phase.

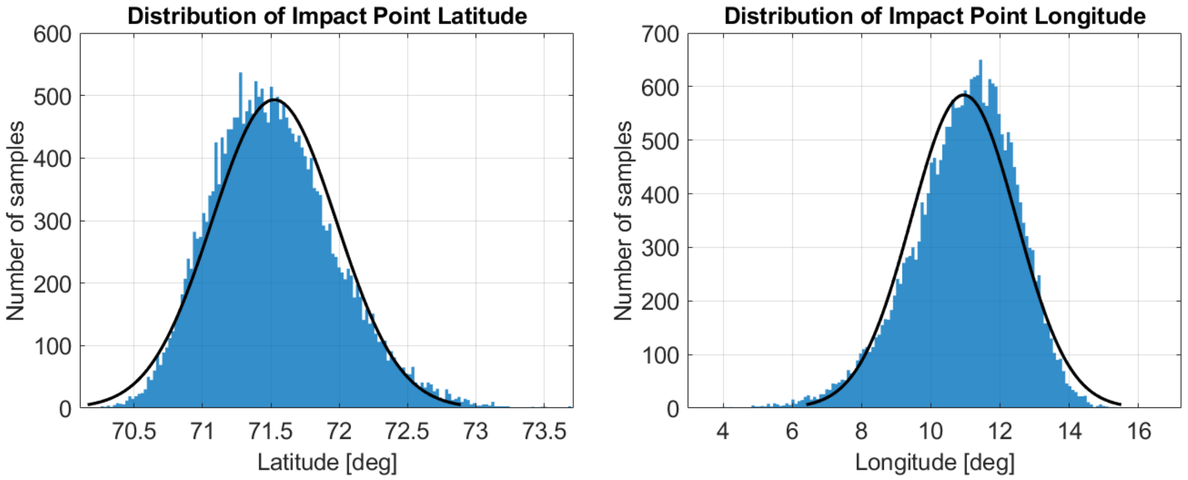

Figure B.2: Histogram and normal distribution fit of the impact point latitudes and longitudes for a Monte Carlo of the full flight.

longitude than the nominal IIP. This can again be attributed to the fact that the nominal case was based on inputs for an expected minimal energy trajectory. Therefore, it is more likely for any deviation from this nominal case to produce a less optimal trajectory that lands closer to the launch site.

Taking these results into account, the second batch was limited to 10000 runs as this was considered sufficient for convergence. The moving averages of this second batch are depicted by the thin, solid black lines in Figure B.3 indicated as ’2nd Batch’. These are not taken into account for the confidence interval. It can be observed that this second batch converges to the same values as the first run, therefore also converging to coordinates slightly below the nominal values. This also means that the second batch has a sufficient number of runs to fall within the established confidence interval. The results of the Monte Carlo simulations are therefore considered to be verified. The 3-σ impact probability area subsequently calculated for this IIP distribution was previously presented in Section 5.4.

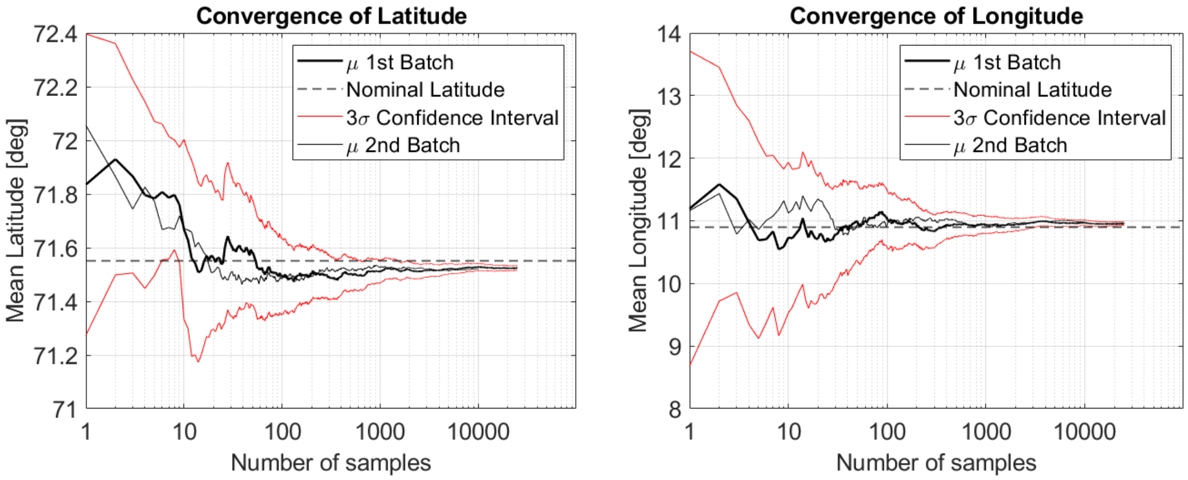

Figure B.3: Convergence and confidence analysis of the impact point latitudes and longitudes.

B.2. Evaluation of the Zero Roll Rate Assumption

Throughout this report, the assumption is made to model the trajectory of the Dart at a roll rate of zero. This section evaluates the validity of this assumption.

The assumption is tested by observing the impact point distribution of the full flight Monte Carlo simulations using ASTOS, both with and without a roll rate for the Dart payload stage. All other model parameters are unchanged. As previously established, the purpose of the spin motors is to induce a roll rate of the full vehicle during the propelled phase to provide the necessary stability during early launch phases. This roll rate can then either be sustained throughout the ballistic phase, or stabilized at the start of this ballistic phase. In reality, the vehicle's behaviour is expected to fall in the middle, stabilizing somewhere during the ballistic phase. This situation is not tested, as it is considered sufficient to only test the two extreme cases of a fully sustained roll rate or immediate stabilization. Neither case considers the added influence of the Magnus effect, which causes a slight deviation of the trajectory due to unequal pressures on opposite sides of a rotating body (Hooke, 2015).

Figure B.4 shows the Monte Carlo impact point distribution for the two presented cases. The impact point distribution for a Dart with zero roll rate is depicted in blue, which are the same 25000 points presented in the analysis and Figure B.1 above. The red distribution represents the impact points for a sustained roll rate throughout the ballistic phase, with its accompanying 3-σ impact probability area as the red ellipse. The computation time of this simulation was much higher, so only 1000 runs were performed before ASTOS ran out of the available internal memory for a single simulation. From this figure, it can be observed that both sets of impact points overlap, with a very similar impact probability area. However, since the Monte Carlo for a sustained roll rate only consists of 1000 runs, additional information is needed. Therefore, Figure B.5 provides a convergence and confidence analysis of these results. Here, it can be observed that at 1000 runs, full convergence has not yet been achieved. However, due to the aforementioned computation time and memory issues, it was very difficult to achieve a simulation of more runs. The confidence intervals for both the latitude and longitude do appear to be narrowing significantly, indicating the approach of convergence. At this rate, the expected converged values again seem to be a slightly lower than nominal latitude and a slightly higher than nominal longitude. This matches the results found for the zero roll rate Monte Carlo simulation.

Overall, due to the observed similarity in behaviour and the great decrease in model complexity and computation time, it is decided to accept the assumption of a zero roll rate of the Dart during the ballistic phase. This was to be expected, because the roll rate induced by the spin motors mainly acts as a countermeasure against destabilising factors such as fin, thrust and assembly misalignments. Such misalignment factors are not considered in the current iteration of the trajectory model, thus it is not required to include the roll rate in the model for compensation.

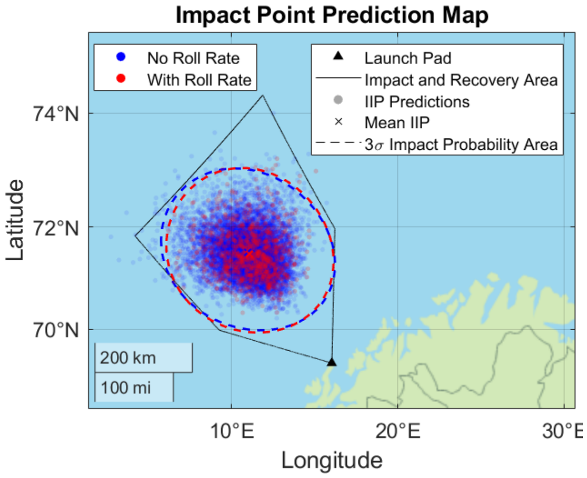

Figure B.4: Evaluating the validity of the assumption of a zero roll rate during the ballistic flight phase.

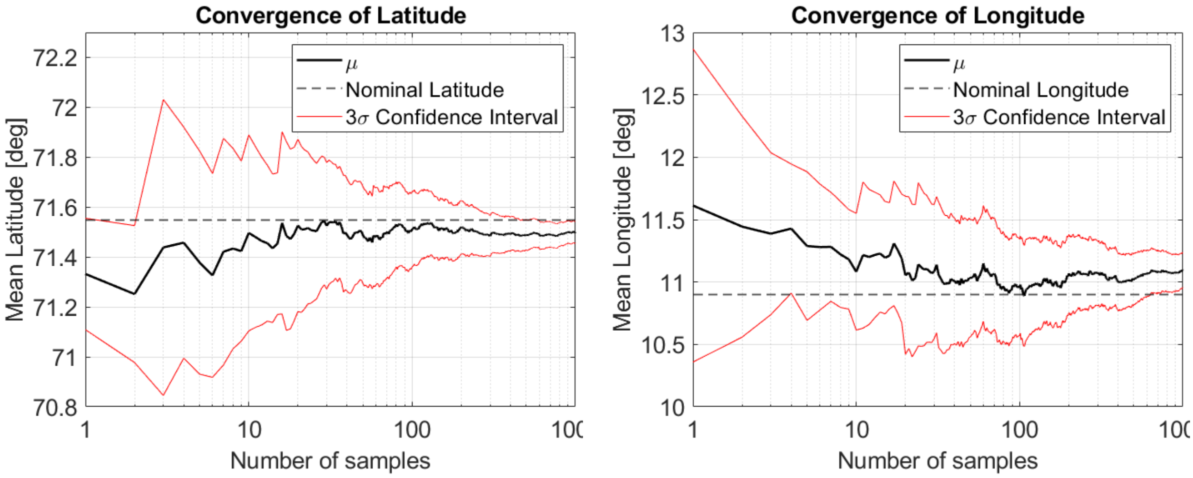

Figure B.5: Convergence and confidence analysis of the impact point latitudes and longitudes, for a simulation with a sustained roll rate throughout the ballistic phase.

C

Verification & Validation

A key factor in developing a model is to ensure verification and validation of the obtained results. Here, validation is aimed at determining whether the right thing was developed, whereas verification is aimed at determining whether it was developed right. Different aspects of both the pre-flight and in-flight models were discussed throughout this report. Therefore, the table below provides an overview of where to find these verification and validation results.

Table C.1: Verification and validation reference table.

Verification and Validation data	Location
Monte Carlo convergence	
Ballistic flight	Section 5.3
Full flight	Appendix B
In-flight model environment model aspects	
Atmospheric model	Section 7.1
Gravitational model	Section 7.1
Rotational model	Section 7.1
Shape model	Section 7.1
Wind model and correction factor	Section 7.1
Vacuum thrust conversion	
Pressure ratio	Appendix A
Thrust coefficient	Appendix A
Trajectory	
Pre-flight model versions	Section 5.2
In-flight IIP prediction	Section 7.2
Launch from a different location	Section 7.5
Ballistic phase with zero roll rate	Appendix B

D

Transformation Matrices between Reference Frames

This appendix provides several transformation matrices between the reference frames that were discussed in Section 6.1. Reversing the direction of any given transformation matrix, so to go from frame 'B' to 'A' instead of from 'A' to 'B', is possible by transposing the transformation matrix. The table below gives an overview of the different variables and superscripts that are used throughout this appendix.

Table D.1: Descriptions of variables and frame superscripts used in the frame transformations.

	Symbol	Description
Angles	Λ	Longitude
	λ	Latitude
	χ_0	Launch azimuth angle
	ω	Earth's rotational speed
	t_O	Stellar time of point O
Superscripts	C	ECEF reference frame
	I	ECI reference frame
	N	ENU reference frame
	T	TRU reference frame

Earth-Centered Inertial (ECI) to Earth-Centered Earth-Fixed (ECEF) frame:
The transformation from the ECI to the ECEF frame accounts for the rotation of the Earth around the z-axis.

$$\begin{bmatrix} X^C \\ Y^C \\ Z^C \end{bmatrix} = \begin{bmatrix} \cos\omega t_O & \sin\omega t_O & 0 \\ -\sin\omega t_O & \cos\omega t_O & 0 \\ 0 & 0 & 1 \end{bmatrix} \begin{bmatrix} X^I \\ Y^I \\ Z^I \end{bmatrix} \tag{D.1}$$

East-North-Up (ENU) to Earth-Centered Earth-Fixed (ECEF) frame:
The transformation from the ENU to the ECEF frame accounts for the change in frame origin from the launch location to the center of Earth, and the orientation change from local 'up' to North along the Earth's rotation axis.

$$\begin{bmatrix} X^C \\ Y^C \\ Z^C \end{bmatrix} = \begin{bmatrix} -\sin\Lambda & -\cos\Lambda\ \sin\lambda & \cos\Lambda\ \cos\lambda \\ \cos\Lambda & -\sin\Lambda\ \sin\lambda & \sin\Lambda\ \cos\lambda \\ 0 & 0\cos\lambda & \sin\lambda \end{bmatrix} \begin{bmatrix} X^N \\ Y^N \\ Z^N \end{bmatrix} \tag{D.2}$$

Trajectory Reconstruction Unit (TRU) to East-North-Up (ENU) frame:
The transformation from the TRU to the ENU frame accounts for the orientation change between two local frames with their origin at the launch location. It does so by rotating around the local z-axis with the magnitude of the azimuth angle. The x-axis changes from pointing along the downrange direction to pointing toward local North. The y-axis changes from the cross-range direction to local East.

$$\begin{bmatrix} X^N \\ Y^N \\ Z^N \end{bmatrix} = \begin{bmatrix} \sin\chi_0 & \cos\chi_0 & 0 \\ \cos\chi_0 & -\sin\chi_0 & 0 \\ 0 & 0 & 1 \end{bmatrix} \begin{bmatrix} X^T \\ Y^T \\ Z^T \end{bmatrix} \tag{D.3}$$

E

Accelerometer Mechanical Characteristics

This appendix provides the tables of mechanical characteristics from the datasheets for the high-range accelerometers used during the propelled flight phase and the high-accuracy accelerometers used during the ballistic flight phase. Both types of accelerometers are used in the Trajectory Reconstruction Unit (TRU). These tables are referenced in Chapter 8 to determine the uncertainty of the TRU input initial state vector.

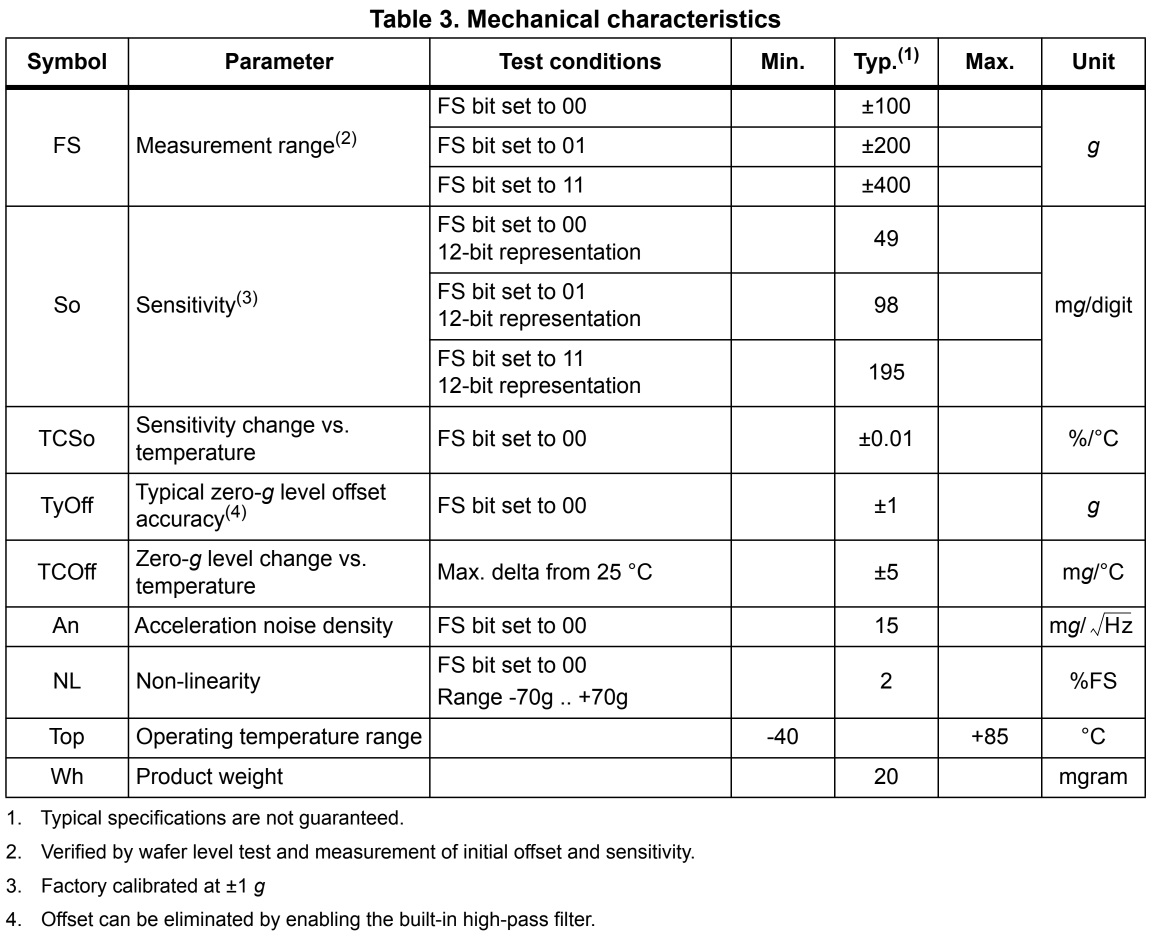

Table 3. Mechanical characteristics

Symbol	Parameter	Test conditions	Min.	Typ.(1)	Max.	Unit
FS	Measurement range(2)	FS bit set to 00		±100		*g*
		FS bit set to 01		±200		
		FS bit set to 11		±400		
So	Sensitivity(3)	FS bit set to 00 12-bit representation		49		m*g*/digit
		FS bit set to 01 12-bit representation		98		
		FS bit set to 11 12-bit representation		195		
TCSo	Sensitivity change vs. temperature	FS bit set to 00		±0.01		%/°C
TyOff	Typical zero-*g* level offset accuracy(4)	FS bit set to 00		±1		*g*
TCOff	Zero-*g* level change vs. temperature	Max. delta from 25 °C		±5		m*g*/°C
An	Acceleration noise density	FS bit set to 00		15		m*g*/$\sqrt{\text{Hz}}$
NL	Non-linearity	FS bit set to 00 Range -70g .. +70g		2		%FS
Top	Operating temperature range		-40		+85	°C
Wh	Product weight			20		mgram

1. Typical specifications are not guaranteed.
2. Verified by wafer level test and measurement of initial offset and sensitivity.
3. Factory calibrated at ±1 *g*
4. Offset can be eliminated by enabling the built-in high-pass filter.

Figure E.1: Table of mechanical characteristics of the high-range accelerometers used in the TRU.
[Source: Table 3 from STMicroelectronics, 2013]

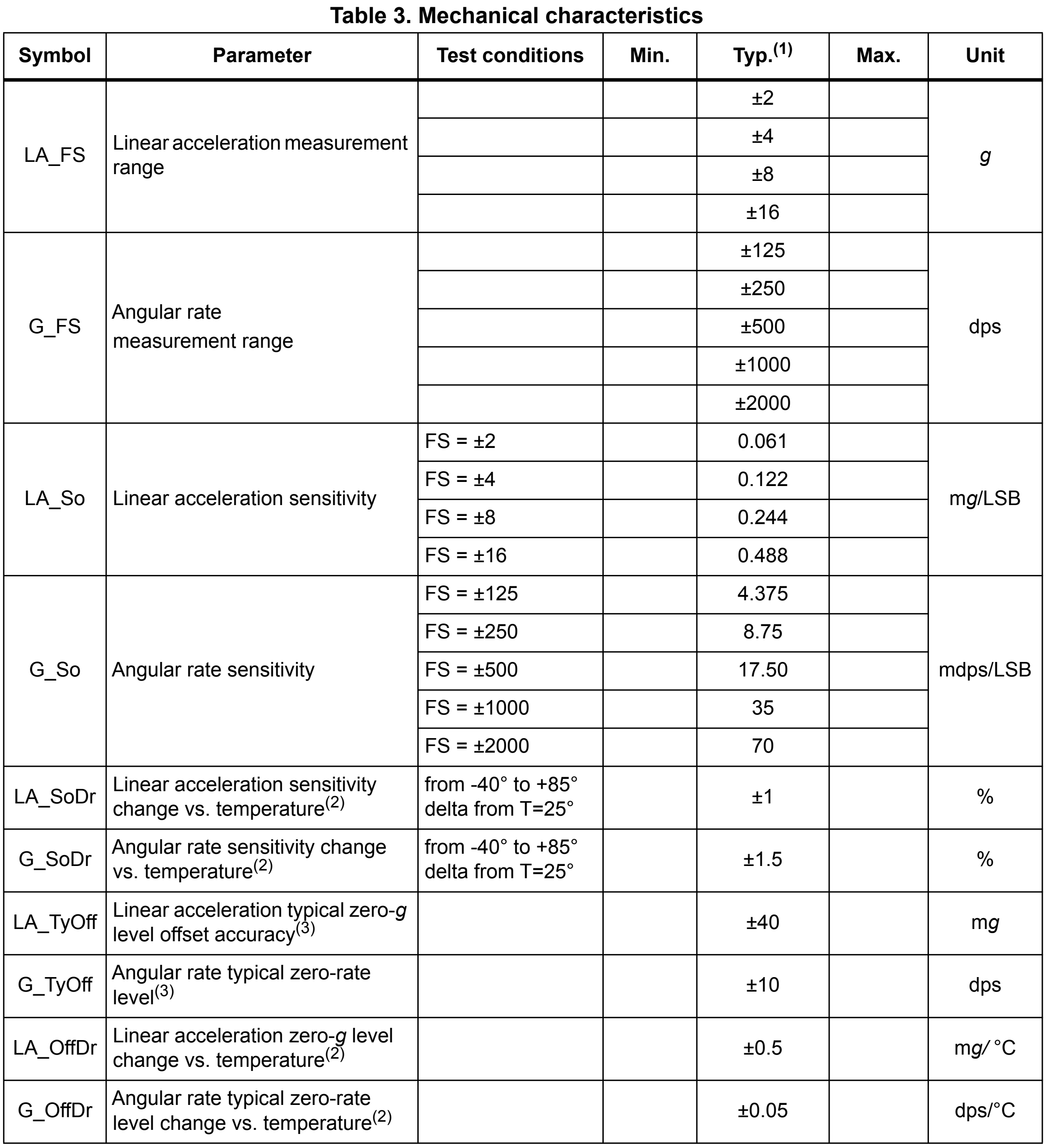

Table 3. Mechanical characteristics

Symbol	Parameter	Test conditions	Min.	Typ.(1)	Max.	Unit
LA_FS	Linear acceleration measurement range			±2		*g*
				±4		
				±8		
				±16		
G_FS	Angular rate measurement range			±125		dps
				±250		
				±500		
				±1000		
				±2000		
LA_So	Linear acceleration sensitivity	FS = ±2		0.061		m*g*/LSB
		FS = ±4		0.122		
		FS = ±8		0.244		
		FS = ±16		0.488		
G_So	Angular rate sensitivity	FS = ±125		4.375		mdps/LSB
		FS = ±250		8.75		
		FS = ±500		17.50		
		FS = ±1000		35		
		FS = ±2000		70		
LA_SoDr	Linear acceleration sensitivity change vs. temperature(2)	from -40° to +85° delta from T=25°		±1		%
G_SoDr	Angular rate sensitivity change vs. temperature(2)	from -40° to +85° delta from T=25°		±1.5		%
LA_TyOff	Linear acceleration typical zero-*g* level offset accuracy(3)			±40		m*g*
G_TyOff	Angular rate typical zero-rate level(3)			±10		dps
LA_OffDr	Linear acceleration zero-*g* level change vs. temperature(2)			±0.5		m*g*/ °C
G_OffDr	Angular rate typical zero-rate level change vs. temperature(2)			±0.05		dps/°C

(a) Part 1 of the table of mechanical characteristics.

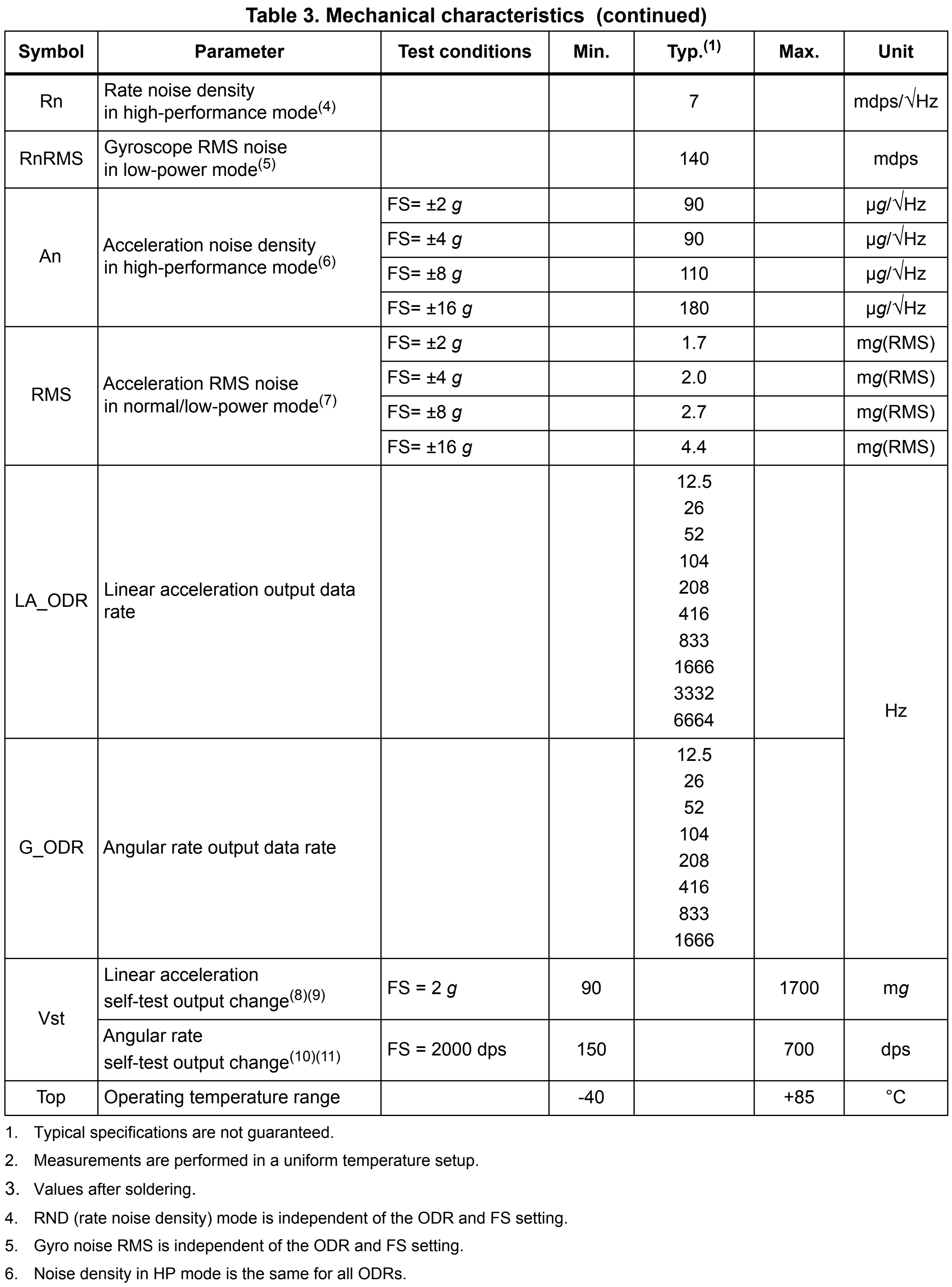

Table 3. Mechanical characteristics (continued)

Symbol	Parameter	Test conditions	Min.	Typ.(1)	Max.	Unit
Rn	Rate noise density in high-performance mode(4)			7		mdps/√Hz
RnRMS	Gyroscope RMS noise in low-power mode(5)			140		mdps
An	Acceleration noise density in high-performance mode(6)	FS= ±2 *g*		90		µ*g*/√Hz
		FS= ±4 *g*		90		µ*g*/√Hz
		FS= ±8 *g*		110		µ*g*/√Hz
		FS= ±16 *g*		180		µ*g*/√Hz
RMS	Acceleration RMS noise in normal/low-power mode(7)	FS= ±2 *g*		1.7		m*g*(RMS)
		FS= ±4 *g*		2.0		m*g*(RMS)
		FS= ±8 *g*		2.7		m*g*(RMS)
		FS= ±16 *g*		4.4		m*g*(RMS)
LA_ODR	Linear acceleration output data rate			12.5 26 52 104 208 416 833 1666 3332 6664		Hz
G_ODR	Angular rate output data rate			12.5 26 52 104 208 416 833 1666		
Vst	Linear acceleration self-test output change(8)(9)	FS = 2 *g*	90		1700	m*g*
	Angular rate self-test output change(10)(11)	FS = 2000 dps	150		700	dps
Top	Operating temperature range		-40		+85	°C

1. Typical specifications are not guaranteed.
2. Measurements are performed in a uniform temperature setup.
3. Values after soldering.
4. RND (rate noise density) mode is independent of the ODR and FS setting.
5. Gyro noise RMS is independent of the ODR and FS setting.
6. Noise density in HP mode is the same for all ODRs.

(b) Part 2 of the table of mechanical characteristics.

Figure E.2: Table of mechanical characteristics of the high-accuracy accelerometers used in the TRU.
[Source: Table 3 from STMicroelectronics, 2017]

References

AIAA (2010). *Guide to Reference and Standard*. G-003C. American Institute of Aeronautics and Astronautics. ISBN: 9781600867842.

Anderson, J. (2012). 'The Standard Atmosphere'. In: *Introduction to Flight*. 7th ed. McGraw-Hill. Chap. 3, pp. 110–133. ISBN: 9780071086059.

Arianespace (2014). 'Launch vehicle general data'. In: *Vega User's Manual*. Issue 4.0. Chap. 1.5.1, pp. 1.5–1.6. DOI: 10.1057/9781137002419_2.

Arianespace (2021). 'Launch Vehicle and range RF systems'. In: *Ariane 6 User's Manual*. 2.0. Ariane Group. Chap. 3.5.1, p. 3.18. URL: https://www.arianespace.com/wp-content/uploads/2021/03/Mua-6_Issue-2_Revision-0_March-2021.pdf.

Arianespace and ESA (2019). *Vega Flight VV15: Findings of the Independent Inquiry Commission's investigations - Press Release*. URL: https://www.arianespace.com/press-release/vega-flight-vv15-findings-of-the-independent-inquiry-commissions-investigations/ (visited on 10/09/2020).

Astos Solutions GmbH (2020a). *ASTOS 9 - Model Reference*. V 9.16.0. Stuttgart: Astos Solutions GmbH.

Astos Solutions GmbH (2020b). *ASTOS 9 - User Manual*. V 9.16.0. Stuttgart: Astos Solutions GmbH.

Basse, A. et al. (2021). 'Seasonal effects in the long-Term correction of short-Term wind measurements using reanalysis data'. In: *Wind Energy Science* 6.6, pp. 1473–1490. DOI: 10.5194/wes-6-1473-2021.

Bille, M. and E. Lishock (2004). 'Storming the Heavens: Satellites of 1958-59'. In: *The First Space Race: Launching the World's First Satellites*. 1st ed. Texas A&M University Press. Chap. 9, pp. 151–171. ISBN: 1585443743.

Blue Origin (2018). 'System Characteristics'. In: *New Glenn Payload User's Guide*. Revision C. Chap. 1.2, pp. 16–19.

Bull, J. and R. Lanzi (2007). 'An Autonomous Flight Safety System'. In: *AIAA Missile Sciences Conference 2008*.

Burghardt, T. (2020). *Virgin Orbit's First Orbital Launch Attempt Terminated Shortly After Release - NASASpaceFlight.com*. URL: https://www.nasaspaceflight.com/2020/05/virgin-orbit-first-orbital-launch-launcherone/ (visited on 02/09/2020).

Clark, S. (2017). *Auto-destruct system seen as a key to ramping up launch tempos – Spaceflight Now*. URL: https://spaceflightnow.com/2017/02/25/auto-destruct-safety-system-seen-as-key-to-ramping-up-launch-tempos/ (visited on 05/08/2020).

Clark, S. (2020a). *Ariane 5 to test modified fairing for JWST, hardware for new range safety system - Spaceflight Now*. URL: https://spaceflightnow.com/2020/07/31/ariane-5-launch-to-test-modified-payload-fairing-for-jwst/ (visited on 09/09/2020).

Clark, S. (2020b). *SpaceX poised for back-to-back launches Sunday at Cape Canaveral - Spaceflight Now*. URL: https://spaceflightnow.com/2020/08/29/spacex-poised-for-back-to-back-launches-sunday-at-cape-canaveral/ (visited on 09/09/2020).

Clark, S. (2022). *NASA not planning another Artemis 1 countdown dress rehearsal - Spaceflight Now*. URL: https://spaceflightnow.com/2022/06/22/nasa-not-planning-another-artemis-1-countdown-dress-rehearsal/ (visited on 29/06/2022).

Dirkx, D. and E. Mooij (2017). *Numerical Integration - Week 2*. Lecture Slides, AE4866 - Propagation and Optimization, Delft University of Technology.

ECMWF (2019). *ERA5 monthly averaged data on pressure levels from 1979 to present*. DOI: 10.24381/cds.6860a573. URL: https://cds.climate.copernicus.eu/cdsapp#!/dataset/reanalysis-era5-pressure-levels-monthly-means (visited on 07/07/2021).

Eggers, J. (2022). *NASA Releases Autonomous Flight Termination Unit Software to Industry*. URL: https://www.nasa.gov/feature/wallops/2021/nasa-releases-autonomous-flight-termination-unit-software-to-industry.

Engelen, F. (2012). *Quantitative risk analysis of unguided rocket trajectories -Master of Science Thesis*. Tech. rep. Delft: Delft University of Technology. URL: https://repository.tudelft.nl/islandora/object/uuid:2dfae5a6-809e-484d-8b3e-ebd146d891f3?collection=education.

European Commission (2022). 'Category 7 Navigation and Avionics - 7A105'. In: *Commission Delegated Regulation (EU) 2022/1 of 20 October 2021 amending Regulation (EU) 2021/821 of the European Parliament and of the Council as regards the list of dual-use items - Document 32022R0001*. Chap. Part IX, p. 216. URL: https://eur-lex.europa.eu/legal-content/EN/TXT/PDF/?uri=CELEX:32022R0001&from=EN.

Ferrell, B. et al. (2004). 'Autonomous Flight Safety System'. In: *41st Space Congress Conference Proceedings*.

Foust, J. (2020). *Astra launch terminated during first-stage burn - SpaceNews*. URL: https://spacenews.com/astra-launch-terminated-during-first-stage-burn/ (visited on 14/09/2020).

Foust, J. (2021). *Firefly Alpha failure blamed on premature engine shutdown - SpaceNews*. URL: https://spacenews.com/firefly-alpha-failure-blamed-on-premature-engine-shutdown/ (visited on 29/06/2022).

Foust, J. (2022). *Vulcan Centaur on schedule for first launch in 2022 as New Glenn slips*. URL: https://spacenews.com/vulcan-centaur-on-schedule-for-first-launch-in-2022-as-new-glenn-slips/ (visited on 29/06/2022).

Frick, W. (2002). 'Pegasus - Past, Present and Future'. In: *Smaller Satellites: Bigger Business? - Concepts, Applications and Markets for Micro/Nanosatellites in a New Information World*. Ed. by M. Rycroft and N. Crosby. Volume 6. Dordrecht: Springer Science+Business Media, pp. 229–237. ISBN: 9789401730082. DOI: 10.1007/978-94-017-3008-2.

Fudge, M., T. Stagliano and S. Tsiao (2003). *Non-Traditional Flight Safety Systems & Integrated Vehicle Health Management Systems - Descriptions of Proposed & Existing Systems and Enabling Technologies & Verification Methods Final Report*. URL: https://www.faa.gov/space/legislation_regulation_guidance/media/DO3_Report_final.pdf.

Groves, P. (2013). 'Inertial Navigation'. In: *Principles of GNSS, Inertial, and Multisensor Integrated Navigation Systems*. 2nd ed. Artech House. Chap. 5, pp. 163–216. ISBN: 9781608070060.

Gupta, S. C., B. N. Suresh and K. Sivan (2007). 'Evolution of Indian launch vehicle technologies'. In: *Current Science* 93.12, pp. 1697–1714. ISSN: 00113891.

Henry, C. (2017). *Avio expanding Vega launch abilities, mulls "light" mini-variant - SpaceNews*. URL: https://spacenews.com/avio-expanding-vega-launch-abilities-mulls-light-mini-variant/ (visited on 02/11/2020).

Higham, D. (2004). 'An Introduction to Financial Option Valuation - Mathematics, Stochastics and Computation'. In: *An Introduction to Financial Option Valuation - Mathematics, Stochastics and Computation*. 1st ed. Cambridge: Cambridge University Press. Chap. 15, pp. 141–150. ISBN: 9780511337048.

Hooke, R. (2015). *The mathematical modelling of projectile trajectories under the influence of environmental effects*. Tech. rep. School of Engineering and Information Technology, UNSW Canberra.

ISRO (2010). *GSLV-F06 Failure-Preliminary findings and Further steps*. URL: https://www.isro.gov.in/update/31-dec-2010/gslv-f06-failure-preliminary-findings-and-further-steps (visited on 29/06/2022).

JAXA (2003). *Launch Result of IGS #2/H-IIA F6*. URL: http://global.jaxa.jp/press/2003/11/20031129_h2af6_e.html (visited on 02/10/2020).

JAXA (2019). *Safety Regulation for Launch Site Operation*. URL: https://sma.jaxa.jp/en/TechDoc/Docs/E_JAXA-JERG-1-007E.pdf.

Jayaraman, T., K. Menon and A. Ganeshan (1982). 'Frames of Reference for Launch-Vehicle Trajectory Simulation'. In: *Simulation* V 39.1, pp. 3–17. DOI: 10.1177/003754978203900101.

Johnson, D. (2017). 'Sensitivity Analysis'. In: *Statistical Tools for the Comprehensive Practice of Industrial Hygiene and Environmental Health Sciences*. 1st. Hoboken: Wiley. Chap. 12.4, pp. 296–297. ISBN: 9781119351375.

Larson, W. and J. Wertz (2005). *Space mission analysis and design*. Microcosm Press & Kluwer Academic Publishers. ISBN: 1881883108.

Mancini, R., E. Scardecchia and S. Gallucci (2019). 'Vega C Light , a flexible and low cost solution for small satellites'. In: *8th European Conference For Aeronautics And Space Sciences (EUCASS)*. DOI: 10.13009/EUCASS2019-771. URL: https://www.eucass.eu/component/docindexer/?task=download&id=5603.

Mooij, E. (2017). *AE4870B - Re-entry Systems Lecture Notes (2017-2018)*. Delft: Delft University of Technology.

Mulder, J. et al. (2013). *AE3202 - Flight Dynamics Lecture Notes (March 2013)*. Delft University of Technology.

NASA (2015). 'Spaceflight Partners: Ensign-Bickford Aerospace & Defense Co.' In: *Space Launch System Highlights* July, p. 3. URL: https://www.nasa.gov/sites/default/files/atoms/files/sls_highlights_july_2015.pdf.

NASA Independent Review Team (2015). *NASA Independent Review Team Orb-3 Accident Investigation Report - Executive Summary*. Tech. rep. National Aeronautics and Space Administration.

Nassiri, N., J. Roushanian and S. Haghighat (2004). 'Stochastic flight simulation applied to a sounding rocket'. In: *International Astronautical Federation - 55th International Astronautical Congress 2004* 1, pp. 72–81. DOI: 10.2514/6.iac-04-a.1.07.

National Research Council (2000). *Streamlining Space Launch Range Safety*. Washington, DC: The National Academies Press. ISBN: 9780309069311. DOI: 10.17226/9790.

NOAA (1962). 'Basis of the Tables'. In: *U.S. Standard Atmosphere, 1962*. Washington, D.C. Chap. Part 1, pp. 3–16.

NOAA (1976). 'Defining Constants and Equations'. In: *U.S. Standard Atmosphere, 1976*. Washington, D.C. Chap. Part 1, pp. 1–20.

Northrop Grumman (2020). 'Avionics'. In: *Pegasus User's Guide*. 8.2. Chap. 2.1.3, pp. 16–17.

Olthof, H. (2020). *Trajectory Reconstruction Unit development*. V1.0. Internal Report T-Minus Engineering: Unpublished.

OxTS (2020). *What are the limitations of GNSS?* URL: https://www.oxts.com/gnss-limitations/ (visited on 04/02/2021).

Park, S. (2022). *Arianespace narrows Vega C and Ariane 6 maiden flight windows - SpaceNews*. URL: https://spacenews.com/arianespace-narrows-vega-c-and-ariane-6-maiden-flight-windows/ (visited on 29/06/2022).

Persson, O., A. Stamminger and H. Hellmann (2007). *Rexus Manual. 4.5*. Tech. rep. EuroLaunch.

Phipps, S. (2017). *30th safety personnel prove integral to automated system's integration - Vandenberg Air Force Base*. URL: https://www.vandenberg.spaceforce.mil/News/Article-Display/Article/1145696/30th-safety-personnel-prove-integral-to-automated-systems-integration/ (visited on 05/08/2020).

Range Safety Group (2019). *Flight Termination Systems Commonality Standard – RCC 319-19*. Tech. rep. New Mexico: Secretariat, Range Commanders Council, US Army White Sands Missile Range.

Rice, T. (2015). *When good rockets go bad - RocketSTEM*. URL: https://www.rocketstem.org/2015/07/05/when-good-rockets-go-bad/ (visited on 26/11/2020).

Rocket Lab USA (2019). *Rocket Lab Debuts Fully Autonomous Flight Termination System*. URL: https://www.rocketlabusa.com/about-us/updates/rocket-lab-debuts-fully-autonomous-flight-termination-system/ (visited on 07/09/2020).

Safonova, M. et al. (2016). ‘An Overview of High-Altitude Balloon Experiments at the Indian Institute of Astrophysics’. In: *Astronomical and Astrophysical Transactions* 29.3, pp. 397–426. arXiv: 1506.01538.

Seidelmann, P. K. et al. (2007). ‘Report of the IAU/IAG Working Group on cartographic coordinates and rotational elements: 2006’. In: *Celestial Mechanics and Dynamical Astronomy* 98.3, pp. 155–180. ISSN: 15729478. DOI: 10.1007/s10569-007-9072-y.

Sheetz, M. and L. Kolodny (2021). *After wobbly liftoff, Astra Space rocket fails to reach orbit once again - CNBC*. URL: https://www.cnbc.com/2021/08/28/watch-rocket-builder-astra-make-second-attempt-at-a-rocket-launch-from-alaska.html (visited on 29/06/2022).

SpaceX (2020). ‘Avionics, and Guidance, Navigation and Control’. In: *Falcon User’s Guide*. April 2020. Chap. 2.5, p. 8.

Spruyt, V. (2014). *How to draw a covariance error ellipse?* URL: https://www.visiondummy.com/2014/04/draw-error-ellipse-representing-covariance-matrix/.

STMicroelectronics (2013). *H3LIS331DL Datasheet - MEMS motion sensor*. Tech. rep.

STMicroelectronics (2017). *LSM6DS3 Datasheet - iNEMO inertial module*. Tech. rep.

Sutton, G. and O. Biblarz (2010). *Rocket Propulsion Elements*. 8th Ed. Wiley. ISBN: 9780470080245.

ULA (2010). ‘Spacecraft Destruct Option’. In: *Atlas V Launch Services User’s Guide*. Revision 1. March. Chap. 5.2.6, p. 5.35. URL: https://www.ulalaunch.com/docs/default-source/rockets/atlasvusersguide2010.pdf.

ULA (2013). ‘Mission Integration and Safety’. In: *Delta IV Launch Services User’s Guide*. June. Chap. 4, pp. 4.1–4.34. URL: https://www.ulalaunch.com/docs/default-source/rockets/delta-iv-user’s-guide.pdf.

ULA (2022). *United Launch Alliance Successfully Launches the Boeing CST-100 Starliner on Orbital Flight Test-2*. URL: https://www.ulalaunch.com/about/news/2022/05/19/united-launch-alliance-successfully-launches-the-boeing-cst-100-starliner-on-orbital-flight-test-2 (visited on 29/06/2022).

US Air Force (2019). *Environmental Assessment Draft Final Vulcan Centaur Program Operations and Launch on Cape Canaveral Air Force Station*. Tech. rep. May. ULA and 45th Space Wing Patrick Air Force Base.

Valencia, L. (2019). *Autonomous Flight Termination System (AFTS)*. URL: https://www.gps.gov/cgsic/meetings/2019/valencia.pdf.

Virgin Orbit (2020). *Mission Recap: Our First Launch Demo*. URL: https://virginorbit.com/mission-recap-our-first-launch-demo/ (visited on 07/09/2020).

Wertz, J. (2009). *Orbit & Constellation Design & Management*. 2nd ed. Microcosm Press & Springer. ISBN: 9780792371489.

Wittenberg, H. et al. (2016). *AE4870A - Rocket Motion Lecture Notes (2017-2018)*. September. Delft University of Technology.